Development, characterization, and application of compliant intracortical implants

Kagithiri Srikantharajah

JÜLICH
Forschungszentrum

Mitglied der Helmholtz-Gemeinschaft

Development, characterization, and application of compliant intracortical implants

Kagithiri Srikantharajah

Abstract

Over more than half a century, neural interfaces enabled various breakthroughs to treat patients suffering from neurodegenerative diseases. Up to now, only a few neural devices were able to demonstrate significant clinical impact, such as deep brain stimulation and cochlear implants. However, these probes are exclusively used for stimulating neural activity. As long-term monitoring of, or even bi-directional communication with, the brain still remains challenging, much effort has been devoted in the last years to optimize probe dimensions and to implement low Young's modulus polymers as substrate materials for the device fabrication.
With the goal to produce next-generation, compliant, intracortical probes suitable for chronic implantation, a Michigan-style array was designed by minimizing the probe dimensions and reducing the mismatch between the device and tissue. To this end, an array consisting of four shanks with cross-sections per electrode of $250\,\mu m^2$ were produced using ParyleneC, a biocompatible and soft polymer, as substrate material. Furthermore, to obtain high quality recordings, a low impedance coating was established utilizing spin-coated PEDOT:PSS. The recording sites with a geometric surface area of $113\,\mu m^2$ were covered with $610\,nm$ thick PEDOT:PSS, resulting in an impedance of $2.650\,M\Omega{\cdot}\mu m^2$. As compliant probes need to be mechanically reinforced during implantation, a tissue-friendly insertion system was developed to reduce the effective length of the intracortical probes by introducing a temporary polyethylene glycol coating. The soft and flexible shanks, with a length of $2\,mm$, were successfully implanted into the mouse barrel cortex without inserting the bulky coating, which minimized the acute trauma during insertion. The compliant implants were able to simultaneously detect local field potentials as well as single-unit and multi-unit activities with a maximum SNR of 7. Additionally, more quality units (SNR>4) were isolated from the recordings using compliant devices in contrast to commercially available traditional stiff probes. These promising outcomes lay the groundwork for future long-term stability validations of compliant intracortical implants and is one step closer towards designing chronically stable devices with seamless biointegration.

Zusammenfassung

Seit mehr als einem halben Jahrhundert ermöglichen Neuroprothesen außerordentlich Erfolge in der Behandlung von neurodegenerativen Erkrankungen, welche die zweithäufigste Todesursache weltweit darstellen. Vor allem mit Stimulationselektroden, wie zum Beispiel der Tiefen Gehirnstimulation, konnten bedeutende klinische Ergebnisse erzielt werden. Da das Messen der neuronalen Aktivität über einen längeren Zeitraum oder sogar eine bidirektionale Kommunikation immer noch eine Herausforderung darstellt, wurde in den letzten Jahren viel Aufwand betrieben, um einerseits die Dimensionen der Implantate zu optimieren und andererseits diese aus organischen Materialien herzustellen. Angelehnt an diese Ansätze war das Ziel der Arbeit, flexible intrakortikale Implantate zu entwickeln, die sich besonders für eine chronische Anwendung eignen. Zu diesem Zweck wurden Implantate mit vier Schafte und einer Querschnittsfläche pro Schaft von $250\,\mu m^2$ designt, die vom Aufbau her den Michigan Implantaten ähneln. Außerdem wurde das biokompatible und weiche Polymer, ParyleneC, für die Herstellung der Implantate verwendet, um die mechanischen Unterschiede zwischen Implantat und Gewebe zu verringern. Mit dem Ziel die Impedanz der Elektroden zu reduzieren und eine gute Qualität der Messungen zu gewährleisten, wurde eine Elektrodenbeschichtung bestehend aus dem leitfähigen Polymers PEDOT:PSS produziert. Die $113\ \mu m^2$ große Elektrode wurden mit $610\,nm$ dickem PEDOT:PSS beschichtet, was eine Impedanz von $2.650\,M\Omega{\cdot}\mu m^2$ ergab. Da die flexiblen Schafte während der Implantation mechanisch verstärkt werden müssen, wurde ein Shuttlesystem bestehend aus einer Polyethyleneglycol Beschichtung entwickelt. Dieses System ermöglicht es, die weichen und flexiblen Schafte ohne sperrige Beschichtung in das Gehirn einzuführen und verringert dadurch das akute Trauma. Die Implantate in Kombination mit dem Shuttlesystem konnte erfolgreich in das Barrel-Kortex von Mäusen eingesetzt werden, um neuronal Ableitungen durchzuführen. Mit Hilfe der Elektroden konnten gleichzeitig hoch- und niederfrequente Signale aufgenommen werden, außerdem war es möglich zwischen Signalen von einzelnen und mehreren Neuronen zu differenzieren. Darüber hinaus wiesen im Vergleich zu gängigen, harten Implantaten die Aufnahmen mit den flexiblen Implantaten einen höheren Anteil an qualitativ hochwertigen Signalen (SNR>4) auf. Diese vielversprechenden Ergebnisse bilden die Grundlage für die folgenden chronischen Implantationen, um ihre langfristige Stabilität zu überprüfen und bringen die Wissenschaft näher an das Ziel chronisch stabile Implantate herzustellen, die sich optimal in das Nervengewebe einfügen.

Eidesstattliche Erklärung

Ich, *Kagithiri Srikantharajah*,
erkläre hiermit, dass diese Dissertation und die darin dargelegten Inhalte die eigenen sind und selbstständig, als Ergebnis der eigenen originären Forschung, generiert wurden.
Hiermit erkläre ich an Eides statt

1. Diese Arbeit wurde vollständig oder größtenteils in der Phase als Doktorand dieser Fakultät und Universität angefertigt;

2. Sofern irgendein Bestandteil dieser Dissertation zuvor für einen akademischen Abschluss oder eine andere Qualifikation an dieser oder einer anderen Institution verwendet wurde, wurde dies klar angezeigt;

3. Wenn immer andere eigene- oder Veröffentlichungen Dritter herangezogen wurden, wurden diese klar benannt;

4. Wenn aus anderen eigenen- oder Veröffentlichungen Dritter zitiert wurde, wurde stets die Quelle hierfür angegeben. Diese Dissertation ist vollständig meine eigene Arbeit, mit der Ausnahme solcher Zitate;

5. Alle wesentlichen Quellen von Unterstützung wurden benannt;

6. Wenn immer ein Teil dieser Dissertation auf der Zusammenarbeit mit anderen basiert, wurde von mir klar gekennzeichnet, was von anderen und was von mir selbst erarbeitet wurde;

7. Ein Teil dieser Arbeit basiert auf der Publikation:
   K. Srikantharajah, R. Medinaceli Quintela, B. M. Kampa, S. Musall, M. Rothermel, and A. Offenhäusser, **Minimally-invasive insertion strategy and in vivo evaluation of multi-shank flexible intracortical probes**, *Scientific Reports*, vol. 11, 2021.

Contents

List of Abbreviations and Symbols

Abbreviations	
AC	Alternating current
ACSF	Artificial cerebrospinal fluid
ADC	Analog-digital converter
AAF	Accelerated ageing factor
AFM	Atomic force microscopy
AP	Action potential
BP	Biodegradable polymers
CE	Counter electrode
CI	Confidence interval
CIC	Charge injection capacity
CNS	Central nervous system
CNT	Carbon nanotubes
CP	Conductive polymer
CSC	Charge storage capacity
CTE	Coefficient of thermal expansion
CV	Cyclic voltammetry
CVD	Chemical vapour deposition
DBS	Deep brain stimulation
DBSA	Dodecylbenzenesulfonic acid
DRIE	Deep reactive ion etching
DI	Deionized
DIP	Dual in-line package
DMSO	Dimethyl sulfoxide
ECoG	Electrocorticography
EDOT	3,4-ethylenedioxythiophene
EEG	Electroencephalography
EIS	Electrochemical impedance spectroscopy
EG	Ethylene glycol
ECD	Electrochemical deposition
ESA	Electrochemical surface area
EIS	Electrochemical impedance spectroscopy
FBR	Foreign body reaction
FDA	Food and Drug Administration
FIB	Focused ion beam

Abbreviations	
GOPS	3-glycidoxypropyltrimethoxysilane
GSA	Geometric surface area
HNF	Helmholtz Nano Facility
ICP	Inductively coupled plasma
IHP	Inner Helmholtz plane
IrOx	Iridium oxide
ISI	Interspike interval
ISO	International Organization for Standardization
LFP	Local field potential
MEA	Microelectrode array
MEMS	Microelectromechanical systems
MUA	Multi-unit activity
MW	Moleculare weight
OHP	Outer Helmholtz plane
PaC	Parylene-C
PBS	Phosphate buffered saline
PCB	Printed circuit board
PDMS	Polydimethylsiloxane
PEDOT	Poly(3,4-ethylenedioxythiophene)
PEG	Polyethylene glycol
PLGA	Poly(lactic-co-glycolic)
PNS	Peripheral nervous system
PPy	Polypyrrole
PSS	Poly(styrene sulfonate)
PVA	Poly(vinyl alcohol)
PVD	Physical vapour deposition
RE	Reference electrode
RF	Radiofrequency
RIE	Reactive ion etching
RMS	Root-mean-square
RPV	Refractory period violation
RT	Room temperature
SCE	Saturated calomel electrode
SEM	Scanning electron microscopy
Si	Silicon
SL	Sacrificial layer
SNR	Signal-to-noise ratio
Std	Standard deviation
SUA	Single-unit activity
UV	Ultraviolett
WE	Working electrode

Variables/Constants	
A	Area
b	Width
C	Capacitance
C_m	Membrane capacitance
C_{dl}	Double layer capacitance
C_{shunt}	Parasitic capacitance
Δf	Noise bandwidth
E	Young's modulus
E_a	Anodic potential limit
E_c	Cathodic potential limit
E_i	Equilibrium potential
F	Faraday constant
g	Conductance
h	Height/Thickness
i	Current density
I	Current
I_c	Capacitive current
I_i	Ionic current
I_m	Membrane current
I_m	Moment of inertia
k	Boltzmann constant
K	Effective length constant
L	Length
λ	Slenderness ratio
P_i	Permeability
P_{cr}	Critical/Buckling force load
r	Distance
r_x	Radius of gyration
R	Gas constant
R	Resistance
R_{ct}	Charge transfer resistance
R_m	Resistance of the metal interconnections
R_{seal}	Sealing resistance
σ	Conductivity
t	Time
T	Absolute temperature
v	Thermal noise
V	Voltage
V_m	Intracellular voltage
V_{rec}	Recorded voltage

Abbrevations

Variables/Constants	
z	Valency of the ion
Z	Impedance
Z_{amp}	Impedance of the amplifier
Z_e	Electrode impedance
Z_{im}	Imaginary part of impedance
Z_j	Impedance of junctional cell membrane
Z_{nj}	Impedance of non-junctional cell membrane
Z_{re}	Real part of impedance

1. Introduction

The human brain, consisting of roughly 86 billion neurons [1], is by far the most complex organ. It controls a wide range of functions such as detection of sensory input, pain perception, as well as control of limb movements. Neurodegenerative diseases are disorders induced by progressive structural and functional degeneration of specific subsets of neurons within the central or peripheral nervous system. Such disorders including Parkinson's disease, Alzheimer's disease and epilepsy represent the second leading cause of deaths worldwide (2016), and substantially impair everyday life of patients [2]. Over more than half a century, a variety of neural devices has been introduced for the treatment of patients suffering from neurodegenerative diseases [3]. Advancements in neurophysiological techniques and microsystem technologies enabled the translation of neural interfaces from fundamental research using rodents and monkeys to clinical human applications. Up to now, only a few neural interfaces were able to demonstrate significant clinical impact, namely deep brain stimulation and the cochlear implant, which are exclusively used for stimulation purposes [3]. However, long-term monitoring of or even bi-directional communication with neurons still remains challenging. Examples of recording devices include the electrocardiogram and the electroencephalogram, which measure heart and brain activity, respectively. Especially, when looking at intracortical implants with superior spatio-temporal resolution compared to the above mentioned surface electrodes, Utah arrays are the only neural probes with medical approval [4, 5]. In contrast to Utah arrays, multi-site and multi-shank Michigan-style arrays allow simultaneous recording of several neurons with a lower probe cross-section. However, Michigan arrays fail during chronic implantation. Neural interfaces need to fulfil certain key features to perform consistently, especially when a chronic application is intended. With increased emphasis, research on ideal probe dimensions, organic materials and insertion methods has been advanced with the ultimate goal to enhance biointegration of neural devices by reducing the foreign body reaction. To this end, low Young's modulus polymers have been considered for the fabrication of implants to decrease the mechanical mismatch between the device and tissue [6, 7]. However, such devices are unable to penetrate the brain without buckling and consequently, need to be mechanically reinforced during implantation. Such insertion systems significantly increase the implantation footprint. To minimize the acute trauma, shuttle systems are needed to precisely position compliant devices without increasing the implantation footprint. Furthermore, to obtain high quality recordings, materials to lower electrode impedance have been

investigated such as coatings utilizing conductive polymers [8].

Driven by the limitation of traditional neural probes and inspired by the above-mentioned efforts, the goal of this work was to produce next-generation, compliant, intracortical implants suitable for chronic applications. In the following chapters, the outcomes and challenges of this attempt are given. Chapters 2 and 3 provide an overview of the fundamental background relevant for this work and of the general techniques employed within the study, respectively. The material choice, design concept and microfabrication of the Michigan-style arrays are introduced in Chapter 4. The low impedance electrode coating utilizing the conductive polymer poly(3,4-ethylenedioxythiophene) doped with poly(styrene sulfonate) (PEDOT:PSS) is described in Chapter 5. Furthermore, this chapter includes the electrochemical and abiotic stability characterization of PEDOT:PSS. As compliant probes are unable to penetrate the brain, a tissue-friendly shuttle system to successfully position compliant implants is reported in Chapter 6. At the end, in Chapter 7, the developed intracortical devices in combination with the low impedance coating and the shuttle system were validated within *ex vivo* and *in vivo* experiments. A summary and suggestions for future improvements towards a chronic *in vivo* implantation are provided in Chapter 8.

2. Fundamentals

2.1. Neural interfaces

Neural interfaces are electric devices that establish bi-directional communication between the nervous system and the outer world [3]. Originally developed for fundamental research, nowadays, these neuroprosthetics are used to treat neurodegenerative diseases such as deafness, blindness and motor disorders. One most prominent example is the cochlear implant that restores hearing by electrically stimulating the auditory nerve [9]. Retinal prosthesis with the potential to rehabilitate vision also received approval for commercial use [10,11]. Moreover, deep brain stimulation (DBS), utilizing intracortically implanted electrodes to stimulate focal brain circuits, is in clinical use for the treatment of movement disorders like tremor in Parkinson disease's patients, dystonia and epilepsy [12].

2.1.1. Essential features for implant development

Neural interfaces need to fulfil certain requirements when a chronic implantation is desired. Therefore, within this section such features like biocompatibility, long-term stability, foreign body reaction, and mechanical, as well as electrical properties are discussed with a particular focus on intracortical implants.
Considering the intended chronic application, materials employed for the implant fabrication such as substrate, insulation, conductor and electrode coating should be biocompatible [13]. Different material properties are involved in the interaction between implantable device and host like chemical composition, micro- and nanostructure, surface and mechanical characteristics. Since the device is in physical contact with the neural tissue, the materials should exhibit biological and chemical inertness, as well as mechanical and electrical robustness. Therefore, reactions such as cytotoxicity, corrosion, degradation, and release of chemical by-products have to be avoided [13]. In this respect, the long-term stability of the neuroprosthetic and more specific the material life time needs to be evaluated. Therefore, besides biotic mechanisms [14–16], the device should be characterized with regard to abiotic failure mechanisms such as polymer delamination due to water uptake, and degradation of electrodes or interconnections [16–18].
Although foreign body reaction (FBR) cannot be completely avoided, the immune

response induced by neural interfaces should be kept to a minimum. Stiff silicon based devices have been shown to lose recording quality over time due to enhanced immune reactions [19]. The brain undergoes constant pulsatile micromotions induced by respiration and cardiac pumping resulting in a constant stress at the device/tissue interface. Additionally, the mechanical properties of the brain can range from 0.03-1.2 MPa depending on animal model and target region [6] whereas static silicon (Si) based implants exhibits a Young's modulus several orders of magnitude higher [20]. The resulting mechanical mismatch triggers an encapsulation of the implant [15, 21]. Neural dieback and microglial proliferation increase the distance between the recording sites and the neurons, decreasing device performance. To overcome the limitations of stiff devices and with the advancement of polymer microelectromechanical systems (MEMS) techniques, compliant neural implants have been introduced as they significantly reduce the FBR (see Section 2.1.3).

However, besides the mechanical disparity, immune responses can be evoked by the implantation trauma or by tethering forces. Different factors contribute to the acute damage generated during device implantation. Compliant probes minimizing FBR are unable to penetrate the neural tissue and therefore, need insertion aids during implantation (see Chapter 6). However, such insertion systems increase the implantation footprint and consequently the acute trauma [22, 23]. Additionally, lesions induced during surgical procedures can result in higher immune reactions. The cranium and the underlying meninges including dura mater, arachnoid and pia mater physically protect the brain from injury [24] (see Figure 2.1). The dura mater exhibits a higher modulus than neural tissue, which impedes the insertion of brittle and flexible implants without performing a duratomy. Thus, dura removal can cause brain swelling, vascular damage, and infection risk. Similar to the implantation, the neural interface should be explanted without introducing additional damage. Due to the brain's micromotions, devices tethered to the skull have shown increased FBR [25, 26]. Therefore, free-floating configurations with monolithically integrated cables have been proposed [27, 28]. However, especially for chronic application, fully implantable devices are desirable to minimize infection risk [29] and interconnection failure, one of the most common failure modes of implantable devices [19]. Wireless communications are another alternative to avoid interconnects but demand a power supply with sufficient life time and low heat dissipation. Furthermore, they must have signal transmission compatible with the high amount of data [29, 30]. To circumvent the high-dimensional data acquisition, on-chip signal processing by integrating active electronic elements might be a promising approach [31, 32].

As recording sites should meet the intended application, they have been introduced in a variety of configurations and compositions. Depending on the intended application, monitoring or manipulating neural activity, the electrodes should exhibit specific electrical properties. Different electrode coatings have been explored to improve the electrochemical characteristics of recording and stimulation electrodes. These feature are discussed in detail in Section 2.2.4 and Chapter 5. Additionally, the size of electrodes needs to be customized based on the desired type of signals

(single cell and/or population activity) and the pursued resolution (single unit or multi-unit activity) [31]. Furthermore, densely packed electrodes have been developed to simultaneously access more cells and to increase spatial resolution [32].

2.1.2. Intracortical implants

Over more than half a century, a variety of neural devices have been proposed to record and manipulate neural activity within the brain [4,5]. Theses cortical implants provide a wide range of neural information through different degrees of invasiveness. Surface electrodes capture activity from population of neurons with low spatial resolution (see Figure 2.1). They are known as electroencephalography (EEG), which are placed on top of the skull or as electrocorticography (ECoG), which are in direct contact with the brain tissue. In contrast to such surface devices, penetrating implants, such as depth and intracortical probes, are able to

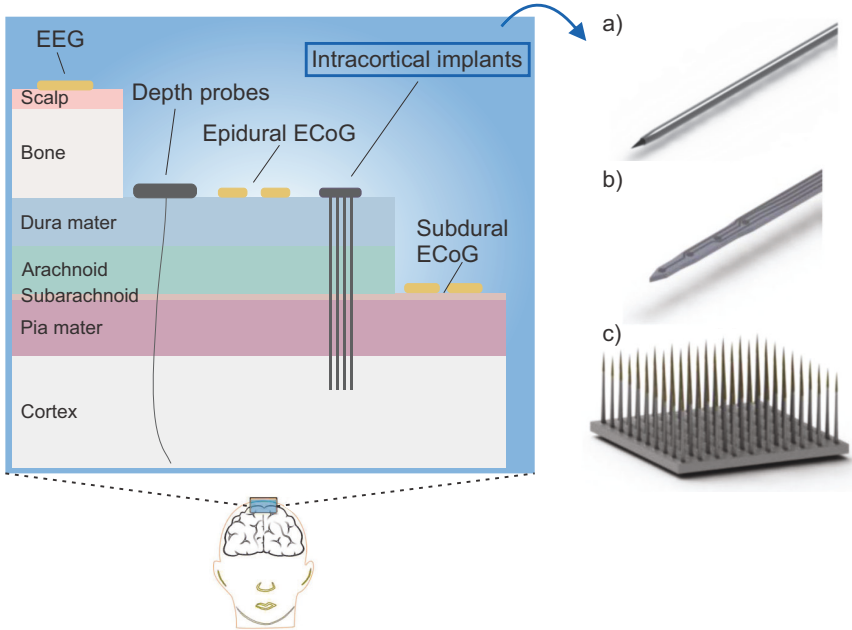**Figure 2.1.:** Overview of cortical implants. Cross-section of brain surface layers with placements of neural probe. Surface electrodes are electroencephalography (EEG) arrays, epdirual and subdural electrocorticography (ECoG) arrays. Penetrating devices are depth and intracortical probes subdivided into microwires (a), Michigan-style (b) and Utah-style (c) arrays. Figures adapted from [6,24].

detect from small networks or even single neurons with superior spatio-temporal resolution.

Intracortical implants are available in different configurations and can be subdivided into microwire and micromachined arrays. Microwires, the oldest neural probes, consist of a sharpened metal wire with a diameter of 10-200 µm (see Figure 2.1 a) [4,5]. The complete wire, typically made out of platinum, platinum-iridium, stainless steel, or tungsten, is isolated using quartz glass, polyimide, or parylene except the tip. This configuration enables the interaction with neurons however, restricts each wire to one single recording site. Thus, different assembling methods have been proposed to group multiple microwires together into arrays with the drawback of higher probe cross-section and significant tissue dimpling during insertion [4,5]. Nevertheless, microwire arrays enabled stable recordings over 1.5 years [33] and up to 7 years from monkeys [34].

With the progress in semiconducting materials and MEMS technology, silicon based probes were developed. These devices are distinguishable into two-dimensional Michigan- or three-dimensional Utah-style arrays (see Figure 2.1 b). Michigan arrays consist of one or several shanks with multiple recording sites aligned along each shank [4,5]. In contrast to microwires, one main advantage of micromachined implants is that they enable recording and stimulation with numerous electrodes per device. Furthermore, different approaches have been proposed to assemble several Michigan probes into 3D arrays [35,36]. Nowadays, commercially available Michigan arrays such as NeuroNexus devices are used as state-of-the-art devices for preclinical research [?]. Another commercially available neural probe and at the same time an example for cutting-edge technology is the high-density array Neuropixels with 960 recording sites distributed over one Si shank [32]. As long and thin Si shanks are prone to breakage, Michigan arrays have been used mainly for experiments with rodents, and showed a stable performance for up to 4-7 months [37,38].

The Utah array comprises several needles sawed into a Si substrate (see Figure 2.1 c). The needles are coated with biocompatible polymers like polyimide and parylene exposing the tip with conductive coatings like gold, platinum, and iridium [4,5]. As tissue dimpling is substantially increased due to the large probe cross-section, high speed insertions or pneumatic aids are utilized. Nevertheless, Utah arrays are the only intracortical device except depth probes with FDA and CE (Conformité Européenne) approval for human application and have been used for controlling cursors and prosthesis, lasting for 1.5 years in monkeys [39] and 2.5 years in humans [40].

2.1.3. Compliant interfaces

The mechanical mismatch between stiff intracortical implants and the soft neural tissue induces the encapsulation of the device, resulting in a degradation of recording
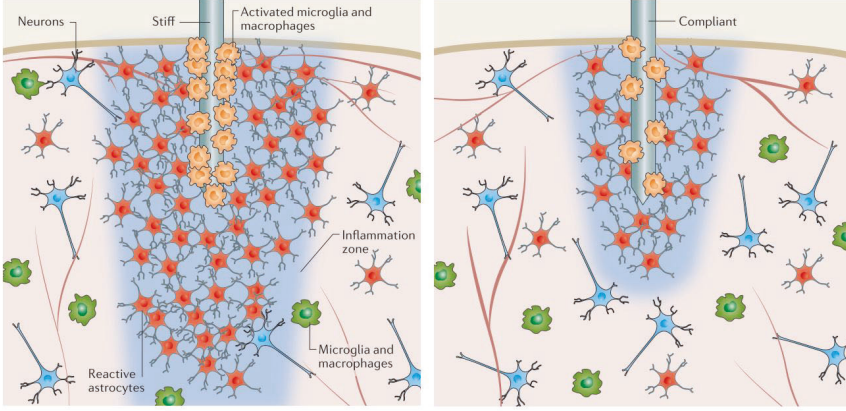
Figure 2.2.: Schematic illustration of the foreign body reaction induced by a stiff (left) and a compliant (right) penetrating shank. Figure from [41].

quality over time (see Figure 2.2). 3D finite-element modelling has demonstrated that decreasing the Young's modulus of implant material substantially reduces the stress at the device/tissue interface [42]. To improve biointegration for chronic application, compliant interfaces have been investigated with great effort. On the one hand low Young's modulus polymers were employed for the microfabrication and on the other hand probe dimensions were minimized (see Sections 4.1 and 4.2). As an example, ultra-small arrays have been produced based on silicon carbide and with a cross-section below $45\,\mu m^2$ [43]. Flexible Michigan-style intracortical implants were produced using parylene [44, 45] or polyimide [46, 47]. Furthermore, ultra-small arrays were proposed utilizing SU-8 with a cross-section below $10\,\mu m^2$ [48]. Validation in rodents and small animals up to 2 years showed an increased neuronal density and decreased microglial migration around compliant probes in contrast to stiff devices [15, 21] (see Figure 2.2). Additionally, stable single-cell recordings using polymer based arrays have been demonstrated for several months [44, 49, 50].

2.2. Neurophysiology

Neural interfaces are used to interface the nervous system by monitoring and manipulating electrophysiological activity of neurons. Therefore, in the following sections, the electrical properties of neurons and their membranes are described. Furthermore, the recording of electrogenic activity using passive transducers and the underlying signal transmission at the cell/electrode interface are explained.

2.2.1. Electrogenic cells

Information processing within cells is based on chemical agents [51], mechanical signals [52] and electrical activity [53]. Cells utilizing the latter are defined as electrogenic cells and include neurons and cardiomyocytes. Neurons are primarily responsible for the information processing within the central nervous system (CNS) and peripheral nervous system (PNS). Although they control several different functions such as detection of sensory input, pain perception and control of limb movements, each neuron follows a typical structure shown in Figure 2.3. They consist of a soma hosting the nucleus, which receives signals from neighbouring cells via multiple dendrites. These signals are transmitted to neighbouring cells via one long process called the axon. Therefore, a single neuron can be represented as a multi-input, 1-output information processing element [54].

Neurons are enclosed by a six to eight nanometer thick plasma membrane that consists of a phospholipid bilayer [55]. Maintaining the physical integrity and controlling the interaction with the environment by exchanging molecules and ions are the main functions of the membrane. The lipid bilayer structure gives rise to the semi-permeability of cell membranes where they act as a capacitor separating the internal and external ionic medium. Driven by the concentration gradient between the inside and outside of the cell, ion channels, specific transmembrane proteins, enable current flow over the membrane. This homeostasis generates a potential difference between the outer and inner cell defined as the resting potential. The equilibrium potential of a certain ion type is defined by the Nernst equation [55]:

$$E_i = \frac{RT}{zF} \, ln\frac{[i]^{exterior}}{[i]^{interior}} \tag{2.1}$$

where R is the gas constant, z is the valence of the ion, F is the Faraday constant and $[i]$ is the concentration of the ion. In neurons, the highest permeability is observed for potassium ions, resulting in a membrane potential similar to the equilibrium potential of K^+. Based on the intra- and extracellular concentrations of K^+ and by applying the Nernst equation, a single ion potential of -85 mV at 37 °C (310.15 K) is obtained[1]. However, the resting potential ranges between -40 mV and -140 mV as not only one specific ion type is involved in establishing the potential. The Goldman-Hodgkin-Katz equation (see Equation 2.2), an extended version of the Nernst equation, accounts for all ions that can pass the membrane, including for example chloride (Cl^-) [55]. Besides the different ion concentrations, the contribution of each ion species is weighted by the permeability P_i.

$$E_i = \frac{RT}{F} \, ln\frac{P_{K^+}[K^+]_e + P_{Na^+}[Na^+]_e + P_{Cl^-}[Cl^-]_i}{P_{K^+}[K^+]_i + P_{Na^+}[Na^+]_i + P_{Cl^-}[Cl^-]_e} \tag{2.2}$$

Hodgkin and Huxley proposed a equivalent circuit model that describes the electrical properties of passive membranes in excitable cells (see Figure 2.4) [56]. As the

---

[1] $E_K = \frac{8.314 \, Jmol^{-1}K^{-1} \cdot 310.13 \, K}{96485.33 \, Cmol^{-1}} \cdot ln\frac{4 \, mM}{96 \, mM}$ (values from [55])

membrane acts as an insulator that separates the conducting inner and outer cell parts, it behaves as a capacitor with a specific membrane capacitance (C_m [F/cm^2]) (see Equation 2.3). The specific membrane capacitance, defined as the charge that needs to be applied across $1\,\text{cm}^2$ of the membrane to change the potential by $1\,\text{V}$, is typically $1\,\mu\text{F/cm}^2$. Transmembrane ion channels perform as resistors. Therefore, the ion specific permeability is described by the conductance (g [S/cm^2]), which is the reciprocal of the resistance ($g=1/R$). Additionally, the ionic current is driven by the difference between the membrane potential (E_m) and the equilibrium potential (E_i [V]). Considering the contribution of different ion species, the ionic current is split into currents carried by sodium and potassium ions (I_{Na} [A], I_K) and leakage currents due to chloride and other ions (I_L). The total membrane current is given by the sum of capacitative (I_c) and ionic (I_i) currents [56]:

$$I_m = I_c + I_i = C_m \frac{dE_m}{dt} + I_{Na} + I_K + I_L$$

$$I_m = C_m \frac{dE_m}{dt} + g_{Na}(E_m - E_{Na}) + g_K(E_m - E_K) + g_L(E_m - E_L). \tag{2.3}$$

The above mentioned membrane potential is valid during the resting period (see Figure 2.3 A). Upon certain stimuli, ion channels are activated. Depending on the membrane permeability of the corresponding ions, the resting potential can increase or decrease. When the membrane depolarizes above a threshold potential, a cascade of ion channel activities is induced increasing the resting potential up to several tens of millivolts. This all-or-none event is defined as the action potential (AP) [55].

Two voltage-dependent conductances in the cell membrane are involved in firing an AP within a neuron. After reaching the threshold potential of around $-50\,mV$, voltage-gated sodium channels open and Na$^+$ ions enter the intracellular space until the positive Nernst potential of Na$^+$ is reached (see Figure 2.3 B). With a short delay, the Na$^+$ channels inactivate themselves while voltage-gated potassium channels open. The efflux of K$^+$ ions occurs inducing a repolarization of the membrane (see Figure 2.3 C). Due to the slow inactivation kinetics of K$^+$ channels compared to Na$^+$ channels, the membrane potential decreases below the resting potential, which is defined as hyperpolarization (see Figure 2.3 D). Finally, the resting potential is re-established (see Figure 2.3 A) by sodium-potassium pumps. The recovery of the inactivated ion channels takes a few milliseconds, defined as the refractory period. During this phase, no further AP can be propagated. As voltage-gated ion channels are transmembrane proteins responding to local potential changes, the depolarization at a certain membrane part results in the activation of the adjacent ion channels and so on. In this manner, the AP can propagate along the axon towards the terminals and the information is transmitted to the neighbouring neuron (see Figure 2.3). Between two neurons, information is transmitted through chemical and electrical synapses, although the latter is less common in the CNS. An incoming AP triggers the release of neurotransmitters,
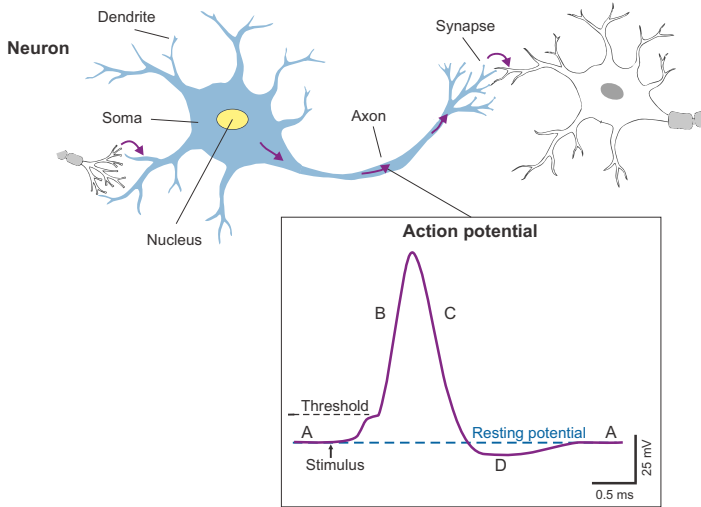
Figure 2.3.: Schematic structure of a neuron: Information is received from multiple dendrites, processed in the soma hosting the nucleus and transmitted by propagating along the axon. At the terminals, synapses convey the signal from one neuron to a neighbouring neuron. Action potential: In response to a stimulus, a depolarization of the membrane potential from its resting potential (A) is observed. If the threshold potential is reached, the influx of sodium causes a depolarization (B). After reaching a peak value and closing the sodium channels, voltage-gated potassium channels are activated. The efflux of potassium results in the repolarization of the membrane (C). Due to the slow inactivation kinetics of the potassium channels, a hyperpolarization (D) occurs before the resting potential is re-established (A). Figure adapted from [55].

which diffuse from the presynaptic end through the synaptic cleft to transmit the signal to the postsynaptic neuron [55].

2.2.2. Neural activity in the brain

The activities responsible for information processing in the brain can be grouped into two main types: APs (see 2.2.1) and field potentials [57, 58]. APs are either elicited by single neurons and defined as single-unit activities (SUAs) or originate from a local neural population and are called multi-unit activities (MUAs). Spiking activity from neurons in the motor cortex has been utilized, for example, to predict hand motions such as hand velocity, position, and forces [59]. In contrast to APs, the field potentials are more complex as they represent the flow of transmembrane currents summed across small populations of neurons where each population exhibits its own size, spatial distribution and frequency [57, 58]. Field potentials can be divided into rhythmic signals and event-related potentials. The latter are large potentials shifts

in neural populations induced by external or internal events. Rhythmic signals include slow, medium, and fast oscillations such as readiness potentials (Bereitschaft potentials), beta, and gamma rhythms, respectively. The oscillations are indicators for control signals and have gained more interested as information sources for neural interfaces. For example, humans were able to adjust the amplitudes of medium rhythms in the sensorimotor cortex by imagining different movements. Furthermore, beta oscillations occur in the primary motor cortex of humans with paralysis [60] whereas strong correlation between gamma oscillations and spiking activities was detected within the visual cortex [61]. Besides the mentioned transmembrane currents, additional events appear in the brain such as Ca^{2+} induced spikes, intrinsic membrane oscillations, and spike afterhyperpolarizations [58]. All these currents contribute to the extracellular field potential, which is used as signal source for neural interfaces. In contrast to APs, field potentials can be detected by EEG, ECoG and intracortical implants as they radiate remarkable distances. When detected by the intracortical probes, such signals have been referred to as local field potentials (LFPs) [57,58].

2.2.3. Recording electrogenic activity

The electrical nature of neural activity described in Section 2.2.1 enables the detection of these signals using electrodes with a wide range of spatial resolution. Whereas current of single cells and even single ion channels can be detected at a micro-scale using patch-clamp, surface electrodes such as EEG measure brain activity at a macro-scale [62]. Extracellular recording at the meso-scale is enabled by microelectrode arrays (MEAs). Already in the 1970s, Thomas, Gross, and Pine introduced such arrays for studying *in vitro* neural networks [63–65]. Nowadays, MEAs are utilized for recording neuronal signals as well as stimulation of electrogenic activity under *in vitro* and *in vivo* conditions. Additionally, these transducers are able to detect extracellular APs and LFPs.

The stereotypic structure of MEA devices is a thin conductive film sandwiched between a substrate and an insulation layer (see Figure 2.4). The electrode size is defined by patterning the insulation layer, and selectively exposing the conductive layer. Local ionic concentration changes outside the cell membrane associated with neural APs propagate through the electrolyte, and capacitively couple to the electrode. Based on the volume conduction, the distance between cell and electrode and the conductivity of the extracellular space mainly determines the potential seen at the electrode and can be described as following [66]:

$$V_e = \sum_{i=1}^{n} \frac{I_i}{4\pi\sigma r_i} \tag{2.4}$$

where V_e is the potential [V], I_i a single current source [A] from a series of n nearby neurons, σ the conductivity of the electrolyte [Ω·m], and r_i is the distance between
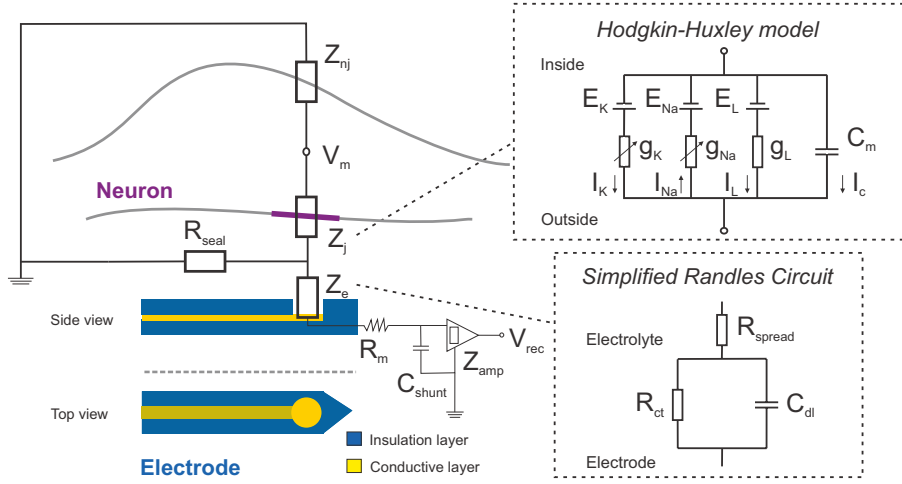
Figure 2.4.: Schematic representation of the point contact model describing the cell/electrode interface with the analogue passive electric circuit. The cell, for example a neuron (purple/grey), on top of a recording electrode consisting of a conductive layer (yellow) sandwiched between two insulation layers (blue). The cell membrane is represented by the Hodgkin-Huxley model with the specific membrane capacitance C_m, the capacitive current I_c, the non-linear conductances g_{Na} and g_K for the sodium (Na$^+$) and potassium (K$^+$) ions, the linear conductance of the leak g_L, the respective equilibrium potentials E_i and ion currents I_i. The membrane facing the electrode is defined as junctional (purple) and the remaining part as non-junctional (grey) membrane and both are depicted by the respective impedances (Z_j, Z_{nj}). The electrode/electrolyte interface is represented by the Simplified Randles circuit with the double layer capacitance C_{dl}, the charge transfer resistance R_{ct}, and the solution resistance R_{spread}. The sealing resistance R_{seal} describes the coupling between cell and electrode. Additionally, the model includes the resistance of the metal interconnections (R_m), the parasitic capacitance (C_{shunt}), the input impedance of the amplifier (Z_{amp}), the intracellular voltage (V_m) and the recorded voltage (V_{rec}). Figure adapted from [31, 56].

the current source and the electrode [m]. Thus, it can be deduced that the detected signal amplitude is inversely proportional to the distance between cell and electrode. Therefore, approaches that promote cellular adhesion are crucial to obtain high signal-to-noise ratio (SNR) recordings, for example by considering compliant neural interfaces (see Section 2.1.3).

2.2.4. Neuron/electrode interface

The key feature of neural interfaces is their recordings sites, as these sites are used to extracellularly detect electrophysiological activity of neurons. The physical
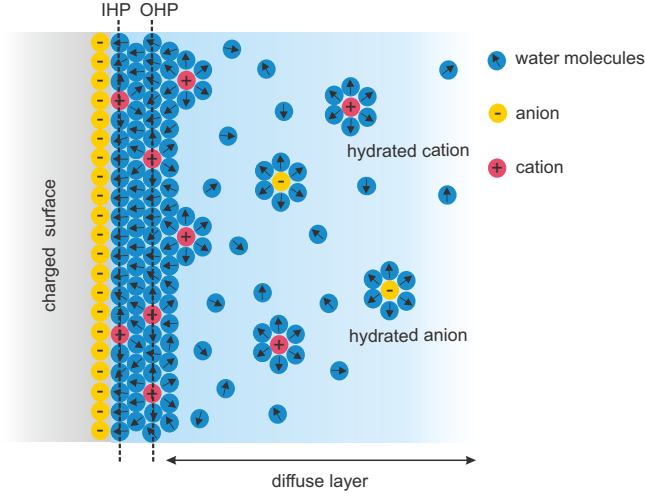
Figure 2.5.: Schematic illustration of the triple-layer model, also known as the extended Gouy-Chapman-Stern model, describing the electrochemical reactions and the ion distributions at the electrode/electrolyte interface and comprising the inner Helmholtz plane (IHP), the outer Helmholtz plane (OHP), and the diffuse layer. Figure adapted from [67].

processes occurring at the interface between cell and electrode mainly influence the quality of the detected signals. Thus, characterizing such interfaces by means of equivalent circuit models is needed to identify the different features comprising the electrochemical system. Based on these findings, one can specifically improve the quality of signals recorded.

As shown in Figure 2.4, the point contact model representing the cell/electrode interface can be subdivided into three main elements: an electrode, a neuron and the cleft between cell and electrode [31, 68, 69]. The electrode and especially the electrochemical reactions and ion distributions at the interface to the electrolyte are described by the extended Gouy-Chapman-Stern model. When immersed into electrolyte, electrodes form an interface zone defined as the electrochemical double layer [67, 69]. Driven by overall equilibrium, different charges accumulate at the interface: electrons within the electrode and ions within the electrolyte. The resulting double layer was first described by Helmholtz as a parallel plate capacitor. He assumed that the ions form a compact layer that is equally and oppositely charged compared to the electrode surface. However, the average distance between ions and electrode depends on the electrolyte concentration influenced by thermal motions and the applied potential. Therefore, Gouy and Chapman proposed a modification in the form of a diffusive layer to account for the decreasing ion concentration with increasing distance to the electrode surface. Stern later combined both the Helmholtz and the Gouy-Chapman model and introduced

the compact-diffuse layer acting as two capacitors in series [67,69]. To account for the adsorbed and hydrated ions, a triple-layer model consisting of the inner Helmholtz plane (IHP), the outer Helmholtz plane (OHP) and the diffuse layer was suggested by Grahame (see Figure 2.5). The IHP is the layer directly formed at the electrode comprising water dipoles and adsorbed ions whereas the OHP spans from the adsorbed-ion centres to the hydrated-ion centres. Such triple layers can be described by three capacitors in series, which can be summed up to the double layer capacitance (C_{dl}) [69].

The electrode/electrolyte interface and the resulting electrode impedance (Z_e) can be described by the Simplified Randles Circuit consisting of the above mentioned C_{dl} shunted by a charge transfer resistance (R_{ct}), in series with the solution resistance (R_{spread}) (see Figure 2.4) [31,70]. The current flow of ions crossing the electrochemical double layer is represented by R_{ct} and the spreading of current into the electrolyte between the working and a reference electrode by R_s. Low electrode/electrolyte impedance is crucial when designing neural interfaces to ensure high quality recordings, as thermal noise scales with electrode impedance:

$$v = \sqrt{4kTZ_{re}\Delta f} \tag{2.5}$$

where v is the thermal noise, k the Boltzmann constant, T the absolute temperature, Z_{re} the real part of the electrode impedance (see Section 3.2.1), and Δf the noise bandwidth. Aiming for high spatial resolution, dimensions of recording sizes are restricted to the size of single neurons. However, electrode impedance is dominated by capacitive reactions at the electrode-electrolyte interface and therefore, is inversely proportional to the surface area [31,71]. Different approaches have been introduced to decrease electrode impedance such as coatings using conductive polymers (see Chapter 5).

Within the model, the neuron surface is subdivided into a junctional membrane that faces the recording sites, and the non-junctional membrane that is in contact with insulation layer and the electrolyte (see Figure 2.4) [31,69]. The plasma membrane is represented by the Hodgkin-Huxley model (see Section 2.2.1). Furthermore, the coupling between neuron and electrode is influenced by the sealing resistance (R_{seal}), which is proportional to the recorded signal and the resulting SNR. Additionally, the recorded signal (V_{rec}) is affected by the resistance of the metal interconnections (R_m), the effective amplifier input impedance including the parasitic capacitance of the entire system (C_{shunt}) and the input impedance of the amplifier (Z_{amp}). C_{shunt} arises mainly from the capacitance between electrodes and electrolyte across the insulation layer as well as from the capacitances along connectors and wires between the electrode and amplifier. Overall, besides a proper data acquisition system with minimum parasitic capacitances, increasing R_{seal} by facilitating a good coupling between neuron and low impedance electrodes are the main factors to ensure high SNR recordings.

3. Methods

All chemicals are purchased from Sigma Aldrich, Germany, unless otherwise noted.

3.1. Optical characterization

The optical validation of the fabricated samples was carried out with the digital microscopes INM 300 (Leica, Germany) and VK-X150 (Keyence Deutschland GmbH, Germany). Furthermore, detailed images of etch profiles and surface morphology were obtained with a scanning electron microscope (SEM) (Magellan 400, FEI Deutschland GmbH, Germany) at $3\,kV$ acceleration voltage and a current of $50\,pA$ using inlens detection. To avoid charging effects, the samples were sputtered with Iridium at $15\,mA$ for $45\,s$ (Sputter coater K575x, Emitech GmbH, Germany). Focused ion beam (FIB) sectioning was performed employing a Helios NanoLab 600i microscope (FEI Deutschland GmbH, Germany) with a gallium ion source. To protect the structures prior to sectioning, a thin layer of platinum followed by a thick layer was deposited onto the region of interest via electron-beam-induced deposition (EBID) ($3\,kV$, $2.7\,nA$) and ion beam-induced deposition (IBID) ($30\,kV$, $2.5\,nA$), respectively. After bulk milling at $30\,kV$ acceleration voltage and a current of $9.3\,nA$, the section was polished at $30\,kV$ and with $230\,pA$. Finally, images were taken at $3\,kV$ and a current of $86\,pA$ using inlens detection. The SEM images and FIB sectioning were performed by the Helmholtz Nano Facility (HNF) staff of the Research Center Jülich.

3.2. Electrical characterization

The electrochemical measurements were performed with different potentiostats using the three electrode configuration featuring the electrodes of the flexible probes as working electrode (WE), a coiled Pt wire as counter electrode (CE) and a Ag/AgCl electrode as reference electrode (RE). Therefore, all potentials in this work are given with respect to Ag/AgCl. The measurements were conducted in phosphate buffered saline (PBS) containing $137\,mM$ NaCl, $2.7\,mM$ KCl, $10\,mM$ Na_2HPO_4 and $2\,mM$ KH_2PO_4 prepared in ultrapure water and with a pH of 7.4 (Recipe from [72]).
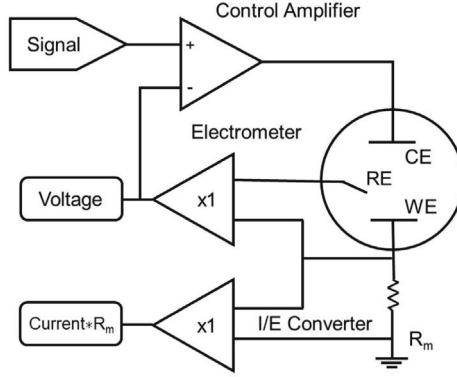
Figure 3.1.: Basic working principle of a potentiostat with three electrode configuration consisting of working electrode (WE), counter electrode (CE) and reference electrode (RE).

The basic working principle of a potentiostat is shown in Figure 3.1. The control amplifier holds the voltage difference between WE and RE by adjusting the current flow across WE and CE (see Figure 3.1). The voltage difference between WE and RE is measured by the electrometer, which ideally has an infinite impedance and almost zero input current. The control of the current is realized by a high-impedance negative feedback mechanism that compensates appearing perturbations. The I/E converter determines the current of the considered cell [67].

3.2.1. Electrochemical impedance spectroscopy

The impedance, Z, is the measure of the opposition to a current flow through an alternating current (AC) circuit in response to an applied potential. The system's output is pseudo-linear if a small excitation pulse is applied. In linear systems, a sinusoidal potential stimulus results in a sinusoidal current response with the same frequency but shifted in phase defined by Ohm's law [67]. Based on the current response, the electrochemical impedance Z can be deduced and by scanning a certain frequency range, the impedance spectrum is obtained. The Bode plot is commonly used to depict the spectrum where the logarithmic impedance

$$|Z| = \sqrt{(Z_{Re})^2 + (Z_{im})^2} \tag{3.1}$$

and the linear phase shift

$$\varphi = arctan(Z_{Im}/Z_{re}) \tag{3.2}$$

with the real Z_{re} and the imaginary Z_{im} parts of the impedance are represented over the logarithmic frequency range [67].
The impedance measurements were obtained with the potentiostat VSP-300 from

Bio-Logic Science Instruments SAS, operated with the EC-lab V11.30 software (Claix, France). A sintered Ag/AgCl pellet electrode served as RE. A 10 mV sine wave was used as excitation stimulus and the response was scanned over the frequency range of 10 Hz to 10 MHz.

3.2.2. Cyclic voltammetry

To investigate thermodynamics of redox reactions, or kinetics of electron transfer, cyclic voltammetry (CV) can be applied. The potential is swept back and forth several times between a higher (E_a) and lower (E_c) switching potential, referred to the reference voltage and with a constant scan rate (v) [73]. The measurements were obtained with the potentiostat CHI1030B from CHI Instruments (Austin, USA). For the CV experiments, the potential was swept linearly between -0.6 and +0.9 V with a scan rate of 0.1 V/s. The DRIREF-2 Ag/AgCl Reference Electrode (World Precision Instruments, USA) was used as RE.

3.3. Atomic force microscopy

Determining topographical properties such as surface roughness is commonly done by atomic force microscopy. Within this work, the atomic force microscope (AFM) analysis was performed in tapping mode (Dimension Edge, Bruker, Germany; Tip: SSS-NCLR-20 with 5 nm radius). To verify the surface roughness, an area of 10x10 µm^2 with a resolution of 256x256 pixels was scanned with a frequency of 5 µm/s and levelling was performed during scanning using brow levelling. The root-mean-square (RMS) roughness is defined as

$$R_{RMS} = \sqrt{\frac{1}{N} \sum_{j=1}^{N} (h_j - \overline{h})^2} \tag{3.3}$$

with h$_j$ as the height above the zero line, $\overline{h}$ the mean height above the zero line and N the number of data points. It was calculated by averaging the values from 2-3 squares. The AFM scans were performed by the HNF staff of the Research Center Jülich.

3.4. Brain slice experiments

3.4.1. Tissue preparation

Brains were obtained from adult pregnant rats and all experiments were approved by Landesumweltamt für Natur, Umwelt und Verbraucherschutz Nordrhein-Westfalen, Recklinghausen, Germany (record number: 81-02.04.2018.A190). The tissue preparation was performed by the staff from the Institute of Biological Information Processing 3 (IBI-3) of the Research Center Jülich. The animal was deeply anaesthetized with CO_2 followed by decapitation. The brain was extracted from the skull within 2-3 min and placed in ice-cold artificial cerebrospinal fluid (ACSF) (125 mM NaCl, 2.5 mM KCl, 1.25 mM NaH_2PO_4, 26 mM $NaHCO_3$, 0.5 mM $CaCl_2$, 5 mM $MgCl_2$, adjusted to 285 mOsm using glucose). 1.5-2 mm thick coronal slices were chopped using a razor blade and transferred to oxygenated ACSF (125 mM NaCl, 2.5 mM KCl, 1.25 mM NaH_2PO_4, 26 mM $NaHCO_3$, 1 mM $CaCl_2$, 2 mM $MgCl_2$, adjusted to 285 mOsm using glucose) at room temperature (RT). The pH of the buffer was maintained between 7.3–7.5 by equilibration with carbogen gas (The Linde Group, Germany) containing 95 % O_2 and 5 % CO_2. If needed, the pH was adjusted using 1 M HCl or $NaHCO_3$. After storing the slices in oxygenated ACSF for 1 h, the measurements were started and completed within 4 h.

3.4.2. Experimental setup

The setup used for the slice experiments was based on [74] and is briefly described below. For the electrophysiological recordings, the slice was transferred to a fully-submerged squared quartz glass chamber. It comprised a PDMS (Sylgard® 184, Dow Corning, Germany) pillow that allowed the fixation of the slice using insect pins. An in- and outflow ensured constant perfusion with oxygenated ACSF with a flow rate of 2.5-2.8 ml/min. Furthermore, the setup consisted of the headstage of the BioMAS system (see Chapter 3.4.3). Additionally, a micromanipulator system (Luigs & Neumann, Germany) was used to move the device along three axes. All mentioned components were mounted on an anti-vibration optical table and built within a Faraday cage to shield external electrical noise. Additionally, the tubing used for the in- and outflow were grounded to the headstage. A digital microscope (VHX-950F, Keyence Deutschland GmbH, Germany) mounted on a flexible arm outside of the Faraday cage was placed in front of the perfusion chamber at 90-70° for a controlled insertion of the penetrating probes.

3.4.3. Data acquisition

The BioMAS system is an in-house data acquisition system comprising of pre-amplifier and main amplifier connected to the controlling PC via an analog-digital converter (ADC) (USB-6255, National Instruments, USA) [75]. The total amplification yields 1010 x with a pre-amplification within the headstage with a factor of 10.1 and a main gain of 100. Data acquisition is enabled by an in-house programmed LabView software (National Instruments, USA) giving the possibility to define recording parameters. A high-pass filter at 1 Hz and a sampling rate of 20 kHz were used for the slice recordings. Furthermore, a sintered Ag/AgCl pellet electrode served as RE.

3.5. Acute in vivo experiments

The animal experiments were performed in the Institute of Biology II, RWTH Aachen University (Germany) and were in accordance with European Union legislation and recommendations by the Federation of European Laboratory Animal Science.

3.5.1. Animal surgery

Three month old wildtype mice (n=3) were used for the acute recordings. The mice were housed under standard laboratory conditions with 12 h light/dark cycle and with access to food and water *ad libitum*. Animals underwent two surgeries. One week before the acute experiments, the head holder was implanted onto the skull. After anaesthetising using 5 % inhaled isoflurane (during the surgery reduced to 1.5-2.5 %) and placing the animal on a heating blanket, analgesia (0.2 ml buprenovet with a concentration of 300 µl/ml) was administered subcutaneously and bupivacain (PUREN Pharma GmbH & Co. KG) was used as local anesthetic by injecting at the incision site. After exposing the skull, a small craniotomy was made above the cerebellum to implant a ground pin. The headbar was placed and fixed with dental cement followed by covering the remaining exposed skull areas with the biocompatible glue Vetbond. One day before the experiments, the craniotomy with a diameter of 3 mm was made above the barrel cortex (AP:-1, ML:-3). To prevent brain swelling, prednisolon (0.12 ml) was applied via intramuscular injection after the surgery and at the start of the acute recordings. After the first surgery and until the day of the experiments, the analgesic buprenovet (1.2 µl/µl) and the antibiotic baytril (0.65 ml, 5 %) were added to the drinking water. A duratomy was prepared just before inserting the probes. During the entire experiments, the mice were placed under anesthesia with 0.5-1 % isoflurane and head-fixed.

3.5.2. Sensory stimulation

The whisker stimulation was performed by generating airpuffs from pulses of compressed air. The airpuffs were delivered via computer-controlled custom scripts written in Python 3 [76]. Three airpuffs within three seconds and with a duration of 100 ms were applied and repeated 50 times with an inter stimulus interval of 10 s.

3.5.3. In vivo electrophysiology

Data were recorded using RZ5 BioAmp digital acquisition system (Tucker Davis Technologies, USA). The sampling rate was 24 kHz. The raw data was analysed offline using custom software written in MATLAB 2020 (Mathworks Inc., USA) and Python 3 [76].

3.5.4. Data analysis

To extract individual waveforms, amplitude thresholding was utilized after filtering the raw data using a 5th order Butterworth band-pass (300 Hz-10 kHz). For each spike exceeding the threshold of 3.9 standard deviations above and below the mean of the filtered trace, a 1.5 ms snippet centred on the absolute minimum of the waveform was extracted. Afterwards, spikes were sorted in MATLAB 2020 (Mathworks Inc., USA) using the package UltraMegaSort2000 [77]. For further analysis, the raw and the sorted data were imported to Python 3 [76]. Peak-to-peak spike amplitudes were determined as the difference between the maximum and minimum voltage of the average waveform for each unit. Signal-to-noise ratio (SNR) for each cluster was defined as peak-to-peak spike amplitude divided by two times the RMS background noise of the associated channel. The noise was calculated using 1 s of filtered trace excluding peaks. Furthermore, interspike intervals (ISIs) defined as the time between successive spikes were considered to distinguish between single units and multiple units. Clusters with more than 100 individual spikes, and with a refractory period violation (RPV) less than 1% for a refractory period of 2.5 ms were classified as single units. All remaining clusters were considered as signals from multiple neurons. The units were further subdivided based on their SNR into moderate (SNR≤4) and quality units (SNR>4). Responses to the whisker stimulation were analysed by calculating the mean firing rate (spikes/s). Clusters were identified as responsive when the mean firing rate during stimulation was at least one standard deviations above the mean firing rate during the 3 s before stimulation.

3.5.5. Histology

The probes were stained with DiI (D282, Invitrogen, USA) for postmortem reconstruction of the penetrations. The dye powder was mixed with ethanol (50 mg/ml) and the compliant probes were submerged repeatedly (5-10 times) into the solution and in between allowed to dry in air for 5 s [78]. This was done one day prior to the acute experiments.

At the end of the acute experiments, the mice were overdosed with pentobarbital and perfused with PBS and 4 % (v/v) paraformaldehyde in PBS. After extraction, the brain was stored in paraformaldehyde solution or in 30 % (w/v) sucrose solution. For sectioning, the brain was embedded in 3 % low-melting point agarose. A vibratome (752/M vibroslice; Campden Instruments) was used to make 100 µm thick coronal brain slices. A mounting medium with DAPI (Invitrogen, USA) was used to visualize the cells besides the penetration tracks. DiI fluorescence and DAPI labelling were imaged at a ZEISS Axio Imager Z1 (Carl Zeiss AG, Germany).

4. Fabrication of compliant intracortical implants

P. Rousche, et al. [79] reported one of the first compliant multi-site penetrating MEAs based on polyimide, which could reach a maximum signal-to-noise ratio (SNR) of 5:1 under acute *in vivo* conditions. Inspired by this work, several attempts were made to show that compliant probes improve the immune acceptance by reducing the mechanical stress at the device/tissue interface. In efforts to produce next-generation neural probes suitable for chronic implantation, two main approaches have been investigated: low Young's modulus polymers as substrate materials [15, 21, 44], and the minimization of the physical probe dimensions [43, 48]. Several studies have shown that compliance is a result of material properties and probe cross-section [7, 80]. Therefore in the following sections, the material choice, design concept and fabrication of compliant polymer based neural probes are introduced with the goal to improve long-term stability within *in vivo* applications.
This chapter was in part reproduced from the following publication:
K. Srikantharajah, R. Medinaceli Quintela, B. M. Kampa, S. Musall, M. Rothermel, and A. Offenhäusser, **Minimally-invasive insertion strategy and in vivo evaluation of multi-shank flexible intracortical probes**, *Scientific Reports*, vol. 11, 2021.

4.1. Polymer choices

Different low Young's modulus polymers have been explored for the fabrication of compliant probes such as parylene [44, 90], polydimethylsiloxane (PDMS) [91], polyimide [79], SU-8 [48, 92], liquid crystal polymers [93] and benzocyclobutene [94]. In Table 4.1, characteristics of the two prominent polymers parylene and PDMS are summarized. Even though their elastic moduli is roughly 10^3-10^6 higher than the mechanical properties of the brain (*e.g.* 0.1-7 kPa in rodents [6]) polymers with a modulus up to a few GPa are commonly classified as flexible [6, 7].
Parylene, and especially paryleneC (PaC), has been widely used within the last years due to its low Young's modulus and its biocompatibility since it received USP Class VI and ISO 10993 compliance (see Table 4.1). As parylene is deposited via chemical vapour deposition (CVD), a transparent, uniform and pinhole-free layer can be
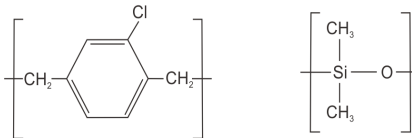
Property	Silicon [a]	ParyleneC [b]	PDMS [c]
Biocompatibility	-	USP VI	USP VI [81]
Young's modulus [GPa]	150	2.76	$0.56 \cdot 10^{-3}-$ $3.59 \cdot 10^{-3}$ [82]
Dielectric constant	11.9 [83]	2.95-3.15	2.68-2.72
Elongation to break [%]	-	2-200	140
Moisture absorption [%]	-	< 0.1 [after 24 h]	-
Degradation temperature [°C]	-	100 [85]	350 (oxidation) [84] 750 (decomposition) [84]
CTE [ppm/°C]	$2.56 \cdot 10^{-6}$	35	340
Achievable thickness [µm]	-	0.1-100 [86, 87]	10-100 [87]
Structural formula	-		

Table 4.1.: Properties of polymers commonly used for flexible implants. Silicon used for traditional stiff probes mentioned as reference. PDMS: polydimethylsiloxane. CTE: Coefficient of thermal expansion. Values from a: [20], b: [88], and c: [89], unless otherwise noted.

obtained, which facilitates the integration into microfabrication methods. The thickness of PaC films can be easily varied, as it is proportional to the dimer mass used for deposition. Furthermore, with a water absorption of less than 0.1 % within 24 h it has a low permeability to moisture [88] resulting in good barrier properties, which are crucial for usage as encapsulation material. However, PaC suffers from poor adhesion to itself and underlying materials such as boron silicate glass, silicon (Si), other polymers and metal films, especially in wet environments. Silanization adhesion promotion process using Gamma-Methacryloxypropyltrimethoxysilane (A-174 silane) has been proven to enhance adhesion by introducing a silane layer covalently bound to the surface that acts as anchor for PaC [95, 96]. It is assumed that the low toxicity of A-174 silane ($LD_{50} > 2000$ mg/kg [97]) can be neglected, as only a monolayer is used and the silane is not in direct contact with the tissue when implanted [96]. Further tests should be performed to confirm the compatibility of the silanization process with chronic neural interfaces. Additionally, the low degradation temperature should be considered when establishing the fabrication process of parylene based devices (see Table 4.1).

PDMS is commonly used in microfluidic applications [98, 99] and for surface electrode arrays [100, 101] but has not been used for penetrating neural probes up to now. Furthermore, its low modulus, high viscoelasticity and permeability to gases make PDMS a prominent choice as substrate material for compliant probes (see Table 4.1). By varying the ratio of pre-polymer and curing agent [82] or the curing temperature [102], the Young's modulus can be tuned. Additionally, some commercially available formulations of PDMS received USP Class VI. Due
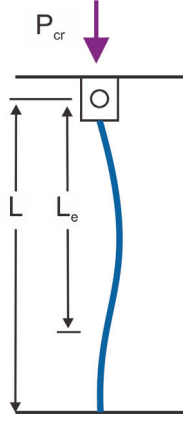
Figure 4.1.: Schematic representation of a fixed-pinned column used to determine the theoretical buckling force P_{cr} of a flexible single shank. The upper end is fixed to the insertion tool whereas the lower end is pinned as soon as it reaches the tissue surface. For a fixed-pinned column, the length L actually resisting the buckling decreases to the effective length L_e.

to the high coefficient of thermal expansion (CTE) the integration of PDMS into microelectromechanical systems (MEMS) techniques is challenging but several approaches have been reported to reduce the thermally induced stress [91, 103, 104].

4.2. Design considerations

To improve the chronic stability, compliant probes with stress relief at the device/tissue interface were explored. Compliance is defined as resistance upon mechanical deformation and cannot be associated exclusively with the material softness defined by the elastic modulus. The buckling force describing the minimal load that induces lateral displacement, also known as bending, can be used as an indicator to specify the compliance of implants. By modelling single shanks of intracortical probes as fixed-pinned columns (see Figure 4.1), the critical load for buckling can be determined using Euler's formula [79]:

$$P_{cr} = \frac{\pi^2 E I_m}{L_e^2} \quad \text{with} \quad I_m = \frac{1}{12}(bh^3) \quad \text{and} \quad L_e = L \cdot K \tag{4.1}$$

where P_{cr} is the buckling force load [N], E the Young's modulus [Pa], I_m the moment of inertia [m⁴], L_e the effective length [m], b the column width [m], h the column thickness [m], L the column length and K the effective length constant which equals 0.7 for a fixed-pinned column. This equation is applicable for shanks that are classified as long columns when exhibiting a slenderness ratio, λ, above 120 [105]:

$$\lambda = \frac{L_e}{r_x} \quad \text{and} \quad r_x = \left(\frac{I_m}{A}\right)^{\frac{1}{2}} \tag{4.2}$$

where r_x the radius of gyration [m] and A the cross-sectional area [m^2]. The theoretical critical load is valid under the assumption that the cross-sectional area is a rectangle and the probe shape is constant over the entire length therefore, tapered tips are neglected. Furthermore, the mechanical influence of the metal stack sandwiched between the polymer layers is ignored as well as any lateral translation the probe might experience at the pinned end [79].

From Euler's formula, it can be deduced that apart from employing polymers that exhibit low Young's modulus, compliance can be achieved by minimizing the probe dimensions. Even thin Si probes feature flexible properties. However, such brittle material have a higher risk of failure due to damaged shanks compared to polymer based probes. Thus, several requirements have to be considered when down-scaling neural implants. The dimensions need to be adjusted to the target brain region and intended application. Depending on the species, the length of intracortical probes can vary, for example from 1.7-5.3 mm for mice to 73.7-105.3 mm for humans for hippocampal studies [6]. The shank width is mainly determined by the metal interconnects and therefore, by the required number of electrodes per shank. During implantation, probes with small geometrical dimensions can lower the penetration force needed to successfully insert the device into the brain due to less tissue displacement [106, 107]. Furthermore, it was shown that a tapered probe tip facilitates insertion and therefore reduces tissue dimpling [106, 107]. Traditionally, neural probes haven been tethered to the skull resulting in an enhanced immune reaction as micromotions from respiration and cardiac pumping can cause forces of 80-130 µN and 14-25 µN at the device/tissue interface, respectively [25, 26]. Besides wireless solutions that are still under development, one approach to avoid tethering induced forces is the integration of a flexible interconnection. Different works from bonding/soldering [27, 108] implants to cables towards monolithically integrated [28, 45, 109] cables have been proposed to establish a free-floating probe fixation. Paradoxically, intracortical implants compliant enough to minimize the body's immune reaction are unable to penetrate the tissue without support, due to the low buckling force threshold. Several insertion strategies to successfully position flexible devices in neural tissue have been introduced in the last years and are discussed in detail in Chapter 6.

4.3. Microfabrication of organic electrodes

With the development of MEMS techniques, batch processing of organic probes with complex designs became feasible to meet the need for disease diagnosis and treatment. The general principle of the microfabrication is a layer-by-layer process mainly involving several steps of deposition, photolithography, and micromachining [110, 111]. The fundamental structure of flexible implants is oriented towards the MEA design described in Section 2.2.3 where a thin conductive layer is sandwiched between two insulation layers. In polymer MEMS, glass or silicon substrates are
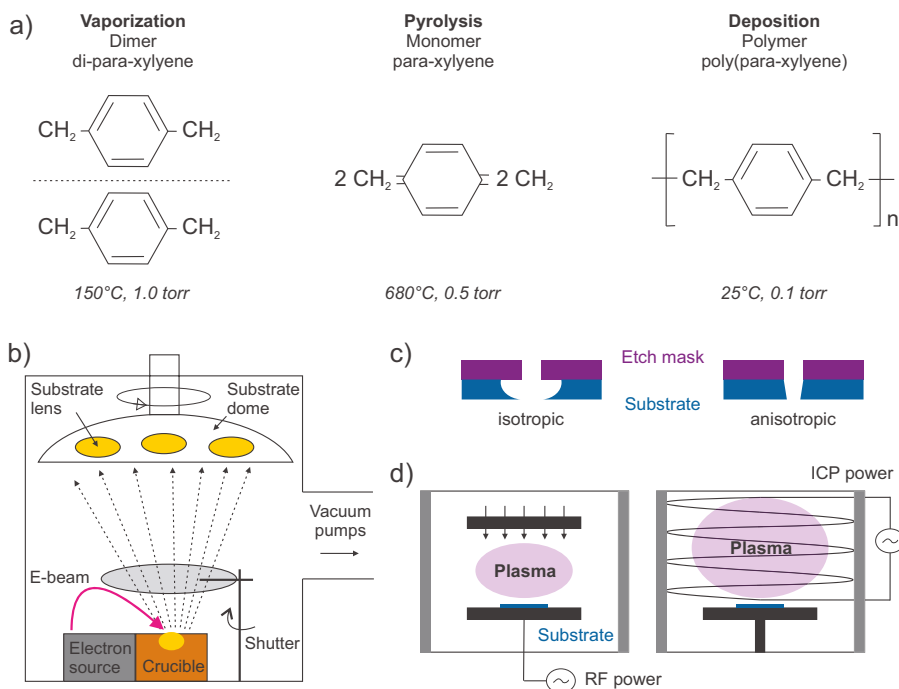
Figure 4.2.: a) Chemical vapour deposition of ParyleneC involving three different stages to polymerize into a uniform coating at room temperature. Figure adapted from [88]. b) E-beam physical vapour deposition to obtain thin metal films. c) Etch profiles obtained by either wet (isotropic) or dry (combination of both) etch. Figure adapted from [115]. d) Reactive ion etching based on capacitive radiofrequency (RF) discharges in a plane parallel geometry or utilizing a inductively coupled plasma (ICP) source. Figure adapted from [115].

used as carrier wafers to support the thin and flexible layers during fabrication. Polymer films are produced via spin-coating (*e.g.* PDMS) or CVD (*e.g.* PaC). On top of the substrate polymer layer, metal films are deposited via physical vapour deposition (PVD). Afterwards, the metal film is structured using lift-off or etching processes [6, 111, 112]. Following the deposition of the second polymer film as insulation layer, dry etching is employed to define the device shape and pattern the electrode sites. The final flexible device is released from the carrier wafer by either mechanical peel off (dry release) or etching a sacrificial layer of thin metals or oxides (wet release). Pre- and post-treatment steps are introduced between the different fabrication stages to ensure clean surfaces or better adhesion between adjacent layers. For example, plasma treatment of the polymer [113], introducing chemical promoters [85, 114] or using metal adhesion layers like titanium [43, 90] are utilized to enhance polymer-metal adhesion.

In the following paragraphs, a detailed description of the microfabrication steps such as CVD, PVD, photolithography, and micromachining are given, which were employed within this work to produce flexible intracortical implants. PaC is deposited via a three-stage CVD process (see Figure 4.2 a) [88]. The solid polymer dimer is vaporized under vacuum at 150 °C. Afterwards, the dimer flows into the pyrolyse furnace where the dimer is heated up to 680 °C and transformed into radical monomer vapour. The reactive monomers enter the deposition chamber, which is kept at room temperature, and polymerize with other monomers covering the entire chamber with a uniform coating.

PVD is employed to deposit thin metal films, which can either be performed via electron beam (e-beam) evaporation, thermal evaporation, or sputtering [111]. Within a vacuum chamber, metal pellets are thermally vaporized and condense onto the substrate positioned above the evaporating material (see Figure 4.2 b). For e-beam evaporation, the sublimation energy is delivered by an e-beam generated from a filament by focusing it onto the metal via magnetic fields.

Micropatterning is performed using photosensitive resists [110–112]. After spin-coating and soft-baking the resist to ensure a homogeneous layer thickness, the desired pattern can be transferred into the resist layer by exposing with UV light through a photomask. During the exposure step, the resist is chemically altered thereby changing its solubility in specific developer mixtures. Depending on the type of resist, the developer removes the exposed areas (positive resist) or the un-exposed layers (negative resist).

Micromachining includes different processes such as chemical etching, laser cutting, and direct laser writing, which are utilized to transfer patterns into materials without photosensitive properties. The employed etching chemistries are sub-divided into dry and wet etch. A high selectivity against the etch mask is crucial to successfully transfer the desired pattern into the substrate [111, 112]. Commonly, photoresists are used as the masking layer. However, for more aggressive processes, hard masks such as Al [116] can be employed. During wet etching, liquid etchant chemically removes the target material not protected by the etch mask. At the interface between etchant and target material, a chemical reaction occurs, usually a reduction-oxidation (redox) reaction where the target material is oxidized. After dissolving the un-protected substrate layer, the resulting byproducts diffuse into the etch solution. The etching rate is influenced by the concentration of etchant, the solution temperature, and the agitation. As this process is diffusion dominated, the etching proceeds uniformly in all directions (isotropically) (see Figure 4.2 c). A fundamental issue of wet etching is under-etching, which is attributed to the isotropic nature of the process [111, 112, 117]. In contrast to the liquid etchant-based structuring, dry etching utilizes a reactive plasma to perform the redox reactions. Besides the chemical nature of the etchant, the ionized gas species can be spatially shaped via electromagnetic fields yielding a physical etch (see Figure 4.2 d). This combination of different etch mechanisms enables the tuning of etching profiles, meaning that a anisotropic profile can be obtained (see Figure 4.2 c). Various

process parameters such as gas mixture, flow rate, generator power, pressure, and temperature need to be optimized to improve etch rate and selectivity. Wet etching of polymers is challenging due to their chemical inertness. Therefore, oxygen plasma etching [118], RIE [118–121] or deep reactive ion etching (DRIE) [118, 119] are commonly used.

4.4. ParyleneC based electrode array fabrication

As part of this work, two different fabrication methodologies have been utilized to produce flexible intracortical neural implants. Both approaches are discussed in detail in the following sections. The probes were produced in the Helmholtz Nano Facility (HNF) of the Research Center Jülich with a ISO class between 2-4.

4.4.1. Single-metal-layer process

In this section, the fabrication of PaC based flexible probes with a single-metal-layer is briefly described. The detailed parameters of the device production are reported in the Appendix A.1. The microfabrication was started with a 5 µm thick parylene film as substrate layer, which is deposited via CVD (see Figure 4.3 a-b). In a vacuum deposition system (PDS2010 Labcoater from Specialty Coating Systems, Inc., USA), 8.5 g of parylene dimer was vaporized at 160 °C, pyrolysed to its monomer at 690 °C, and deposited evenly on Si wafers at RT. Film thickness was verified on a test Si piece by creating a step using tape to partially cover half of the piece during deposition and measuring step height with a profilometer (Dektak 150 Surface Profiler, Veeco Instruments Inc., USA) after peeling off the tape. In the next step, the metal interconnects and electrode sites were defined using a double resist system of LOR3b (MicroChemicals, Germany) and AZ nLOF2020 (MicroChemicals, Germany). This results in an undercut profile, which facilitates the lift-off following metal deposition. After the photolithography process, the PaC surface was treated with a gentle O_2 plasma (50 W, 80 sccm, 2 min) to induce hydrophilicity without significant surface etching [122]. This improves the adhesion between the substrate PaC layer and the metal film [123]. Afterwards, the metal stack was deposited by evaporating 10 nm titanium (Ti) as adhesion layer, 100 nm platinum (Pt) or gold (Au) and 10 nm Ti as etch stop layer with rates of 0.1 nm/s, 0.5 nm/s, and 0.1 nm/s, respectively (see Figure 4.3 c). To remove the resist and excess metal stack, the samples were placed in an acetone bath for 2 to 3 h (see Figure 4.3 d). Afterwards, a 5 µm passivation layer of PaC was deposited as described above (see Figure 4.3 e). Gamma-Methacryloxypropyltrimethoxysilane (A-174 Silane, Specialty Coating Systems, Inc., USA) was added to the deposition chamber to ensure good adhesion onto the underlying Pt film and the PaC substrate layer [96]. 20 µm of AZ 10XT (MicroChemicals, Germany) obtained by a double
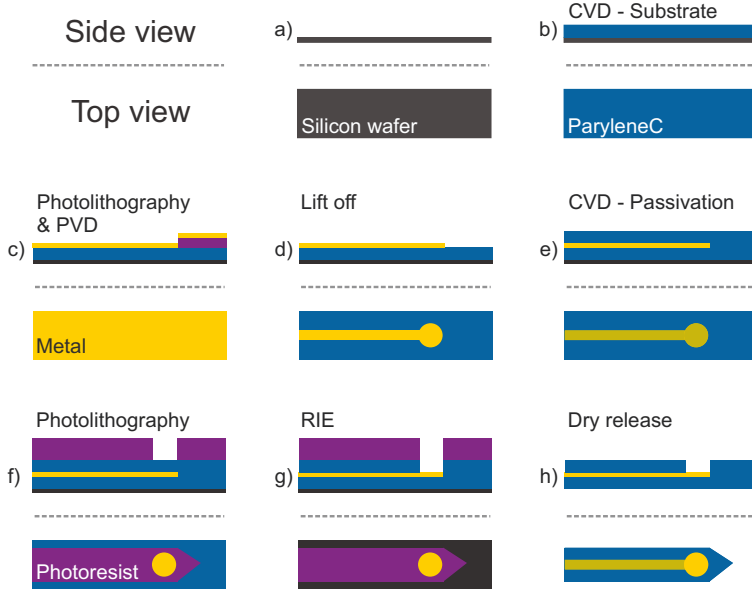
Figure 4.3.: Fabrication process for ParyleneC (PaC) based single-metal-layer probes: Starting from a plain Si wafer (a), PaC is deposited via chemical vapour deposition (CVD) and used as substrate (b) and passivation layer (e). Physical vapour deposition (PVD) is utilized to evaporate metal (c), which is patterned using a lift off process (d). Photolithography is employed to define probe shape and expose electrode sites (f). The structure is transferred into the PaC layers via reactive ion etching (RIE) using resist as etch mask (g). Afterwards, the final device is peeled from the wafer (h).

spin-coating scheme was photolithographically structured and used as etch mask during the RIE process to define the probe shape and to expose contact pads and electrode openings (see Figure 4.3 f). When an electrode coating is desired as shown in Section 5.2.2 electrode sites can be structured in a second etching step after defining probe shape. Etching of PaC was performed with a rate of 0.65-0.70 µm/min (CF$_4$:O$_2$, 4:36 sccm, 0.007 mbar, radiofrequency (RF) plasma 50 W, inductively coupled plasma (ICP) 500 W (see Figure 4.3 g). The remaining resist was removed with AZ 100 Remover (MicroChemicals, Germany). To establish an electrical interconnection, single probes were dry released with a few drops of deionized (DI) water if needed (see Figure 4.3 h) and soldered (soldering paste: NC-31, AMTECH, USA) to custom made DIP connector at 180 °C and sealed with epoxy (EPO-TEK 302, Epoxy Technology, USA) at 110 °C for 30 min (see Appendix A.3). As PaC degrades at 100 °C a direct contact between the hotplate and the polymer should be avoided to not damage the flexible probes.

4.4.2. Double-metal-layer process

The double-metal-layer fabrication of flexible devices is depicted in Figure 4.4. After the deposition of 5 µm PaC as substrate film on a 4 inch Si wafer as described in the previous section (see Figure 4.4 a-b), the metal interconnects with a minimum line width and pitch of 5 µm were evaporated via PVD and structured using a lift off process (see Figure 4.4 c-d). Due to the small dimensions of the interconnects, the photolithography process was changed from the double resist system to using only AZ nLOF2020 (MicroChemicals, Germany). Furthermore, the exposure dose was adjusted for feedline widths less than 5 µm (see Appendix A.2). An interlayer of PaC (500nm) was deposited as insulation between the two metal layers (see Figure 4.4 e). Openings with a diameter of 5 µm were introduced in the interlayer over the interconnect ends via RIE (see Figure 4.4 f-g). Electrode sites and contact pads were defined within the second metallization step (see Figure 4.4 h-i). To ensure electrical connectivity between the two conductive layers, the thickness of the second metal stack was increased to 600 nm (10 nm Ti, 100 nm Pt, 500 nm IrOx or 10 nm Ti, 500 nm Au). After depositing the third PaC film as passivation (see Figure 4.4 j), the probe shapes were patterned and the electrode sites were exposed within the final etching step (see Figure 4.4 k-l). Finally, the probes were peeled from the wafer (see Figure 4.4 m) and soldered to custom made PCBs. The detailed fabrication protocols are attached in Appendix A.2 and A.3.
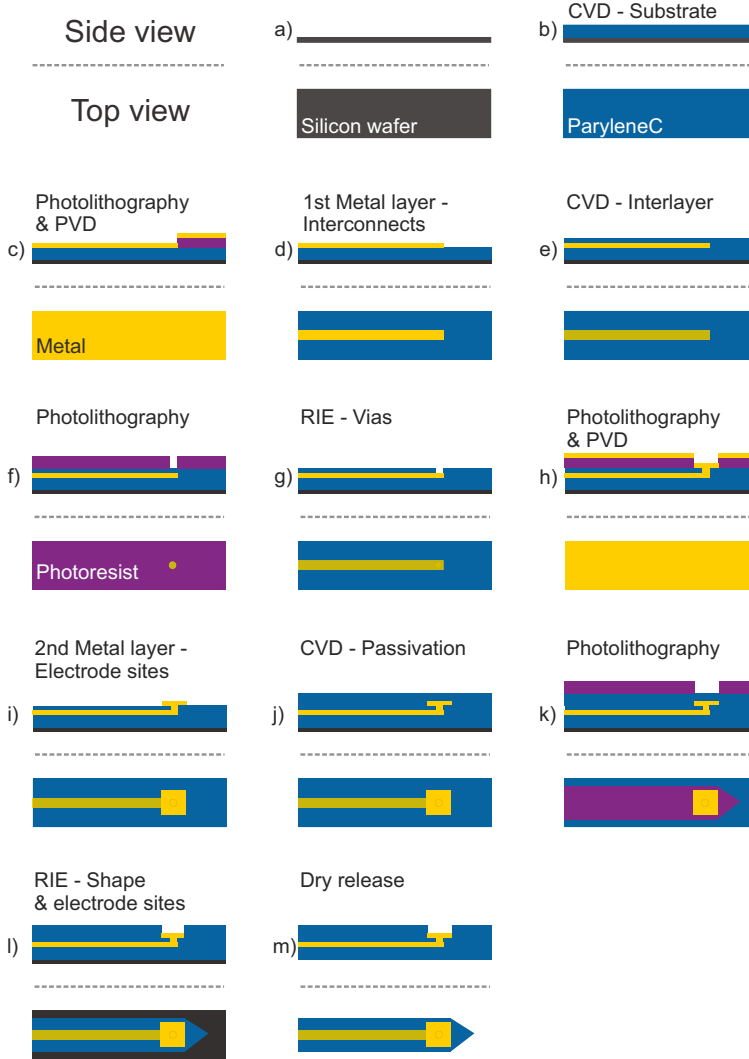
Figure 4.4.: Fabrication scheme of dual-metal-layer MEAs based on ParyleneC (PaC): Starting from a plain Si wafer (a), PaC is deposited via chemical vapour deposition (CVD) serving as substrate layer (b). Physical vapour deposition (PVD) is employed to deposit metal (c), which is patterned using a lift off process (d). Within this first metal layer, the interconnects are patterned. Introducing a PaC interlayer (e) ensures the insulation of both conductive layers and etching vias establishes electrical connectivity (f-g). The second metal layer was evaporated via PVD (h) and structured using a lift off process to define the electrode sites (i). After the deposition of the passivation layer (j), the probe shape is patterned and the electrode exposed using reactive ion etching (RIE) (k-l). The final probe is dry released from the carrier wafer (m).

Figure 4.5.: Metallization challenges of ParyleneC (PaC) based flexible devices: a) When depositing 100 nm Pt on PaC, micro-cracks (white arrows) w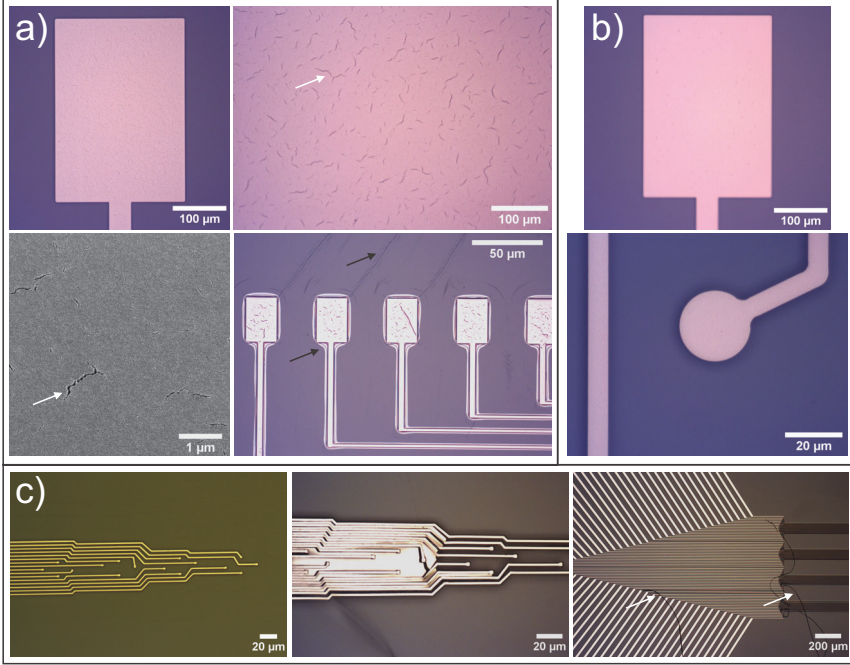ere observed within the metal layer. Additionally, wrinkling of the PaC around Pt was seen when increasing the thickness to 500 nm (black arrows). b) The deposition of 100 nm Au resulted in a smooth layer without cracks and deformations. c) Structuring 2 µm interconnects was feasible (left image) however, occasionally a poor lift-off (centre image) or delamination (right image, arrows) was observed.

4.4.3. Fabrication considerations

Even though working PaC based devices could be produced based on the aforementioned microfabrication process, several challenges were encountered and are further discussed below.

Metal deposition: The e-beam evaporation of Pt on PaC films leaded to cracking of the conductive layer for a thickness of 100 nm. When the thickness was increased to 500 nm, deeper cracks and wrinkling of the PaC around the metal structures were observed (see Figure 4.5a). Based on AFM scans on test Si pieces, it was seen that the microcracks within 100 nm Pt had a length of up to 5-10 µm and a depth of 20-30 nm.

High temperature processes such as evaporation using high melting point metals

such as Pt can lead to thermal stress and therefore, cracking as a result of the mismatch in the thermal coefficients of expansion [85]. However in the presented case, the wafer did not exceed $60\,°C$ when evaporating $100\,nm$ Pt with a rate of $0.5\,nm/s$ as measured via a thermal couple (covered with aluminium tape to enhance thermal contact) placed on the wafer frontside. Increasing the thickness of Pt would result in a rise of the final temperature to $\approx$25-35 $°C/100\,nm$ and therefore the wafer can indeed surpass the degradation temperature of PaC (see Table 4.1) at thicknesses above $200\,nm$ resulting in stress induced deformation of metal layers and PaC films. This phenomenon is pronounced with increased metal thicknesses and therefore, longer evaporation times (see Figure 4.5a). To minimize the thermal radiation from the metal target, a stepwise deposition was performed where $100\,nm$ Pt evaporation was followed by a cooling step of $10\,min$ before the deposition of the second $100\,nm$, which still resulted in cracks though smaller in size. Furthermore, deformations were not observed after the e-beam evaporation of $100\,nm$ Au with rate of $0.5\,nm/s$ (see Figure 4.5b). Compared to Au, Pt has a higher melting point and during evaporation, more secondary electrons are generated indicating that besides the thermal stress, additional factors such as electron radiation are contributing to the cracking. Further investigations are needed here to verify this hypothesis. To reduce the stress induced cracking of metal layers and wrinkling of PaC films, a stepwise deposition or a different ratio of adhesion and conductive layer might be helpful and use metals with lower melting points, such as Au, to avoid thermal radiation.

In contrast to sputtering Pt on PaC [124], no stress induced bending of the flexible shanks was observed after releasing the probes. Furthermore, $100\,µm$ microcracked Pt films on PaC still resulted in conductive interconnections therefore, PaC based probes with Pt as conductive layer were successfully produced and further used within this work. As microcracked or wrinkled metal layers have been introduced for flexible and stretchable electronics [116, 125], using microcracked Pt could be beneficial for designing intracortical implants with long and thin shanks, which can undergo bending stress during the packaging or implantation process.

During the fabrication of thin metal interconnects with a width and interspacing of $2\,µm$, a poor lift-off process or delamination of the thin traces was noticed (see Figure 4.5c). It is known that PaC suffers from poor adhesion to metal as the latter exhibits hydrophilic surface properties whereas PaC is hydrophobic. Several approaches have been introduced to improve the adhesion such as plasma polymerization process using Trimethylsilane as gaseous precursor [126] or treatment with the commercially available adhesion promoter AdPro Plus® [123].

For the fabrication of the proposed flexible probes, the width and interspacing of the metal interconnects was increased to $5\,µm$ to ensure a stable process as for smaller feature sizes, little variations within the photolithography process can affect the final structures. Furthermore, the PaC film was treated with oxygen plasma to induce hydrophilicity just before the evaporation to enhance the adhesion of the metal stack to the substrate layer, which was sufficient to avoid any delamination

of the thin metal traces.

Dry etching: RIE through a photoresist mask was used to pattern the PaC based probes. Gas bubbles were observed underneath the PaC film following the UV exposure (see Figure 4.6a). This phenomenon was in particular observed for big areas of PaC not covered with resist after development and for high UV dose. In the proposed fabrication protocol, 20 µm thick photoresist was exposed with 2100 mJ/m^2 to structure 10 µm PaC films. Previous works have reported similar effects which were attributed to the off-gassing of resists during UV exposure in combination with the gas permeability of PaC [85]. As at this point of patterning the probe shape, the bubbles did not impair the process fabrication was continued without removing the bubbles. However, when using PaC as a sacrificial layer an elimination of the bubbles could be necessary (see Chapter 5.3.1).

After dry etching the PaC probes, cracks were observed within the etch mask and in the underlying polymer films subsequent to stripping the resist (see Figure 4.6b). That the off-gassing of volatile components within the photoresist during plasma etching can lead to the formation of gas bubbles was reported before [85]. Furthermore, it was stated that minor off-gassing especially when processing PaC on carrier wafers might be unnoticeable. Nevertheless, the cracks indicate an intrinsic stress release within the photoresist etch mask although they were not noticed over the entire wafer. It seemed like certain design features such as sharp corners were prone to crack formations. Changing the design into round corners reduced the effect however, did not completely solved the issue (see Figure 4.6b).

Photoresists are commonly stripped with acetone followed by a rinse with isopropanol. However, the removal of the photoresist with acetone was not sufficient after the etching of PaC films with conductive layers embedded as residues were seen on metal structures and probe edges (see Figure 4.6c). The prolonged exposure to plasma during the RIE can cause a cross-linking of the resist and the re-deposition of resist and metal can hamper the etch mask removal [85]. This issue could be solved by using the AZ 100 Remover (MicroChemicals, Germany) especially designed to strip positive photoresist. Furthermore, using a two tank system in combination with a low power ultrasonication where the majority of the resist was removed in the first bath improved the stripping result without leaving any residues.

During the removal of the resist etch mask, some probes especially the shanks were partially or completely released (see Figure 4.6d). When the stripping is the last fabrication step the release is negligible. However, when a second RIE step is needed to expose, for example, the electrode sites partially released probes can impede the alignment of the etch mask. Cleaning the wafers in acetone and isopropanol using sonication for 10 min followed by a rinse in DI water before starting the MEMS process helped to avoid the complete release of the PaC probes. It was assumed that a clean surface ensured a good adhesion between carrier wafer and PaC films during the fabrication. The partial release, especially of the long and thin features
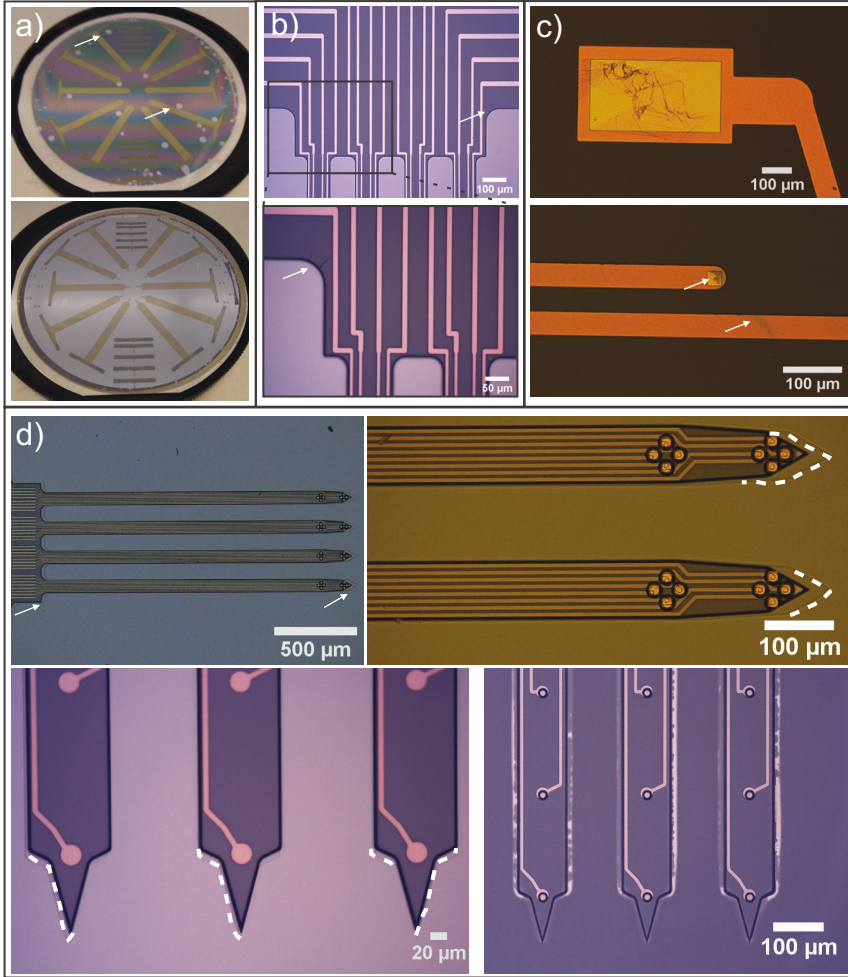
Figure 4.6.: Dry etching challenges of ParyleneC (PaC) based flexible devices: a) Gas bubbles after UV exposure of the photoresist etch mask before (top) and after RIE (bottom). b) Crack formation (arrows) within resist and underlying PaC during etching process. c) Resist residues when stripping with acetone due to cross-linking of resist after pro-longed exposure to plasma. d) Partial release (arrows and dashed lines) of flexible shanks after stripping the etch mask impeding precise alignment of following fabrication steps (bottom right). Dashed lines indicating the actual position of probes before the shift.

was still observed and was predominant for big PaC structures (Chronic probes C-MEA-32L & -32T (see Chapter 4.5)) (see Figure 4.6c). It is unclear whether

Figure 4.7.: Shape and critical dimensions of A-MEA-16 probes, the first generation of PaC based intracortical implants.
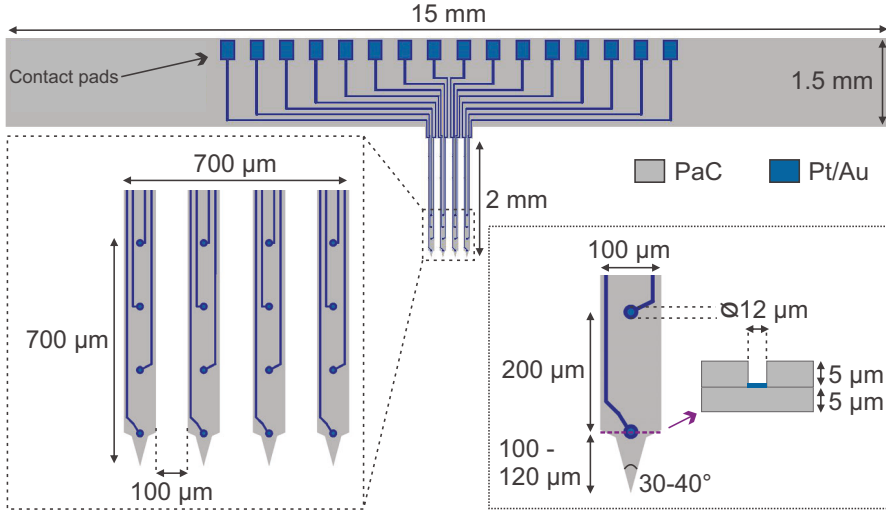
the partial release arises from film stress induced during the RIE step or from prolonged contact with the AZ 100 Remover for more than 15 min. Since AZ 100 Remover had to be used to successfully remove the photoresist without any residues the stripping time and the sonication treatment were adjusted for each wafer to minimize the contact between PaC and the stripper solution. For the small structures (Acute probes A-MEA-16 (see Chapter 4.5), this procedure still resulted in a slight shift of the shanks in the range of 5-7 μm. For the proposed design, a successful alignment was still feasible as the electrode sites were bigger in diameter than the electrode openings leaving a margin for alignment errors (see Figure 4.6d). Furthermore for big structures, where the partial release could not be avoided, the thickness of the etch mask was adjusted so that the entire resist was etched during the RIE resulting in a redundant stripping step. The latter is only practicable if the etching rates of polymer and resist have been precisely determined.

4.5. Flexible intracortical implants

From polymer MEMS fabrication, paryleneC (PaC) based proof-of-concept electrode arrays were produced. The technique allows batch processing of multi-site probes on 4 inch silicon (Si) wafers (see Figure 4.8). A first generation of devices was proposed with the aim to test the performance under acute *in vivo* conditions. These intracortical implants constructed of Pt film sandwiched between two mechanically flexible and insulating PaC layers are Michigan-style devices consisting of four
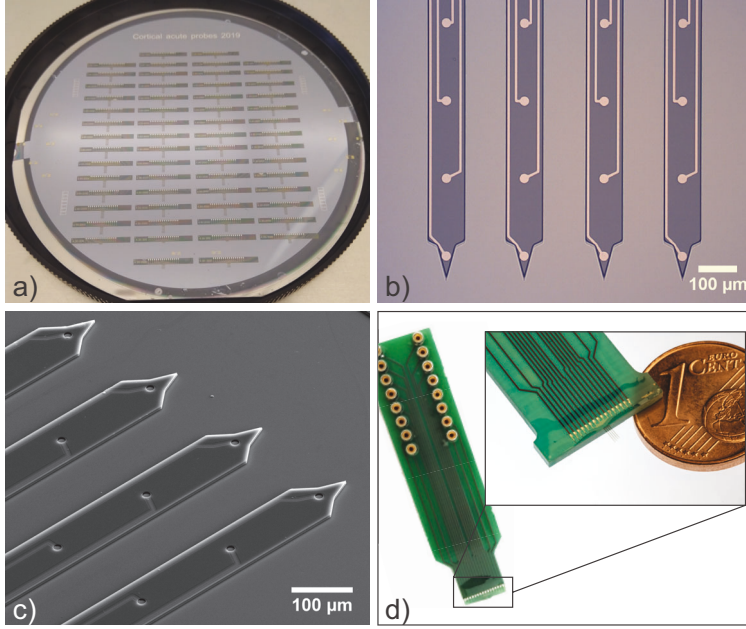
Figure 4.8.: Presentation of the flexible array A-MEA-16: a) Photograph of the PaC probes produced on a 4 inch Si wafer. Close-up microscope (b) and SEM (c) pictures of the four shanks with electrode sites and metal traces. d) Photograph of flexible probe soldered to 16-DIP connector.

shanks with four electrodes per shaft, here after named as A-MEA-16. Aiming for a single unit resolution the electrode sites are 12 µm in diameter with a pitch of 200 µm resulting in an active length of 700 µm. Single shanks have a width of 100 µm and a thickness of 10 µm. A shank length of 2 mm is used to reach a cortical depth of 1.0-1.5 mm where regions of interest like the mitral layer of the olfactory bulb and the different layers of the visual cortex are located. With a shaft interdistance of 100 µm, the array spans 700 µm allowing for a 2D representation of the cortical tissue. To facilitate probe insertion, the shanks have a tapered tip with an opening angle of 40-30 ° [107]. The critical dimensions of the probes are presented in Figure 4.7. The final devices were dry released from the Si wafer and soldered to custom made PCBs (see Figure 4.8). A detailed electrochemical characterization of the neural probes is provided in Chapter 5.

A bulky 16-DIP connector was used for an acute validation of the first generation of probes (see Figure 4.8). However, for chronic implantation, the head implant should met more stringent criteria. Based on G. Buzsáki's experience [127], the probe backend should not exceed 10 % of the rodent's body weight to not impede the free behaviour. Assuming that an adult mouse has an average mass of 30 g, the implant with boards and headmount should be less than 3 g, for experiments with free

moving animals even lower. Therefore, smaller and light-weight custom connectors were designed, consisting of two mated PCBs as depicted in Figure 4.10. The first PCB with contact pads for probe bonding and a female stacking connector (61082-041400LF from Amphenol ICC, USA) can be permanently fixed to the rodent's head whereas the second PCB supporting the male stacking connector (61083-041402LF from Amphenol ICC, USA) and the omnetics connector (A79024-001-NPD-36-AA-GS from Omnetics Connector Corporation, USA) is detachable minimizing the total weight of the headmount. Furthermore to establish a free-floating probe fixation on the rodent's head, a 3 cm long flexible cable was monolithically integrated into the probe design. Besides the backend of the devices, the electrode density is a crucial parameter for chronically implanted probes. For coping with the neural density of $9.2 \cdot 10^4$ neurons/mm^3 in the mouse's cortex [128], a high ratio between recordings sites and neural tissue is needed to enable a large scale monitoring and decoding of tissue. With the aim to increase electrode density but keep the small cross-section and therefore, minimize the tissue damage, the double-metal-layer process was utilized, resulting in the second generation of intracortical implants named as C-MEA-32. The metal traces mainly influence the shank width. Therefore, 5 µm wide interconnects with 5 µm interspacing were chosen in combination with the double-metal-layer process to double the number of electrodes by keeping the shank width (see Figure 4.9). The design of C-MEA-32 is based on 4 shank MEAs with 8 electrodes per shaft. Shank dimensions are similar to A-MEA-16. The electrodes with a diameter of 12 µm are arranged with a spacing of 50 µm. In order to facilitate insertion, the opening angle of the tip was kept at 30°.
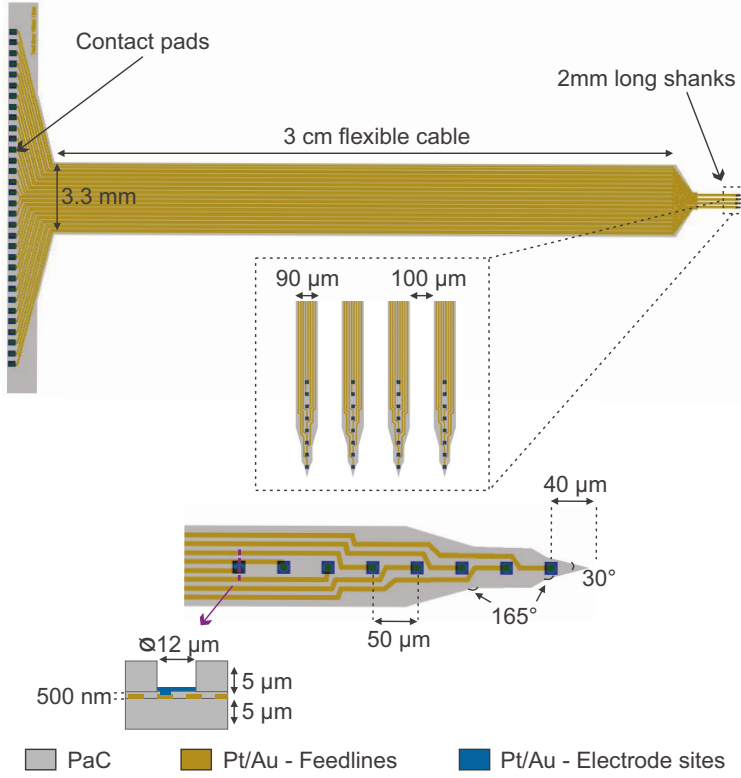
Figure 4.9.: Critical dimensions of the second generation PaC based penetrating probes.
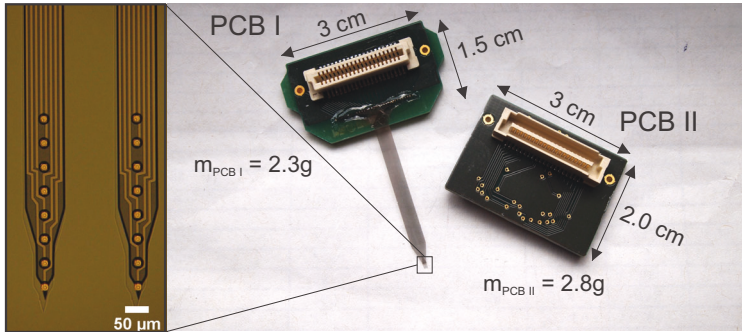
Figure 4.10.: Presentation of the flexible array C-MEA-32L: Microscope image of two shanks with electrode sites and metal traces (left) and photograph of neural probe soldered to PCB I (right), which is proposed as headmount for a chronic application. The detachable PCB II is needed to establish an electrical connection between implant and electrophysiological recording system.

Probe type	Probe cross-section [μm^2]	Number of electrodes	Cross-section per electrode [μm^2]
C-MEA-32 [This work]	**945**	**8**	**118**
Si - A4x4-3mm-100-125-177 [?]	825	4	206
PaC/SU-8 [129]	1800	8	225
Si - A4x8-5mm-50-200-177 [?]	1845	8	231
PaC [21]	700	3	233
A-MEA-16 [This work]	**1000**	**4**	**250**
PaC [130]	1520	6	253
PaC [45]	2600	8	325
PaC [131]	3600	6	450

Table 4.2.: Comparison of representative neural probes with implants proposed within this work. Probe cross-section is obtained by multiplying shank width and thickness. For cross-section per electrode, number of electrode per shank were considered. NeuroNexus Si probes A4x4-3mm-100-125-177 and A4x8-5mm-50-200-177 are comparable in design to A-MEA-16 and C-MEA-32, respectively.

The multi-site intracortical implants produced within this work for acute and chronic applications have cross-sections per electrode of $250\,\mu m^2$ and $118\,\mu m^2$, respectively (see Table 4.2). When comparing to PaC based probes introduced in the last years the A-MEA-16 device has similar cross-sectional profile however, with the C-MEA-32 design, a further reduction by half was possible. To our knowledge, these are the smallest PaC based penetrating probes reported so far with regards to electrode number per single shank. A major challenge when down scaling neural probes is the increase in electrical crosstalk between nearby interconnections and electrode sites. Therefore, especially the C-MEA-32 probes should be characterized in regard to crosstalk before using them for electrophysiological measurements. Furthermore, it was possible to reach electrode densities comparable to state-of-the-art commercial Si probes.

4.6. Conclusion

Compliant probes have been explored as chronic neural interface to study the brain by considering low Young's modulus polymers as substrate materials and by reducing probe cross-sections. Within this work, the microfabrication of such a compliant intracortical implant was demonstrated. The probes were designed for reaching cortical depths of up to 2 mm so that regions of interest like the visual cortex and the olfactory bulb could be targeted. Even though PaC is prone to thermal degradation, a successful fabrication process could be established. Furthermore, to our knowledge, the smallest PaC based penetrating probes could be produced utilizing the double-metal-layer process.
From the fabrication perspective, a further reduction in cross-section would be

feasible, which is ideal to increase the probe compliance. However, this is impractical for handling due to bending or breakage. In efforts to produce next-generation neural probes, PDMS was considered with a Young's modulus one-tenth lower than PaC. In Appendix A.4, the microfabrication protocol for PDMS based implants is provided. Even though probes could be produced, the main challenge was the handling of these ultra-soft devices. They curled without any mechanical support after releasing them from the carrier wafer due to residual stress within the thin polymer films. To avoid curling, probes with balanced internal stress need to be produced. Implementing the insertion aid into the microfabrication process could be an option to mechanically reinforce the probes after release. As more optimization is needed to make these probes usable, the PDMS based devices were not further studied within this work.

No matter which polymer is considered for the production of penetrating probes the limits for device flexibility and size still need to be further studied as a function of tissue response and chronic stability of implants. Before testing longevity of the introduced flexible intracortical implants, the electrochemical performance was optimized by establishing a low impedance electrode coating (see Chapter 5) using the A-MEA-16 design. Afterwards, an insertion system was developed (see Chapter 6) and tested within acute *in vivo* experiments (see Chapter 7) to demonstrate the implant feasibility.

5. PEDOT:PSS as electrode coating material

MEAs have been introduced as a versatile tool to interface neuronal networks, enabling the recording and stimulation under *in vitro* as well as *in vivo* conditions (see Section 2.2.3). Commonly, the electrode geometry is restricted to the size of single neurons to ensure a high spatial resolution. Densely packed MEAs used to decode the spatial pattern of extracellular activity additionally limit the size of single electrodes [132, 133]. However, small electrode sites exhibit low capacitance and high impedance. The electrode impedance is dominated by capacitive reactions at the electrode-electrolyte interface and therefore, is inversely proportional to the surface area [71]. Brownian motion of electrons and diffusion of ions at the interface can cause noise, which scales with impedance resulting in low signal-to-noise ratio (SNR) recordings impeding high quality measurements [31, 134]. For stimulation purposes, a high charge storage capacity (CSC) and a high maximum charge injection capacity (CIC) within a potential window that minimizes irreversible faradaic reactions at the electrode are favourable. Low impedance electrodes reduce the thermal noise and the charge injection limit needed to successfully stimulate neuronal tissue and are therefore beneficial for monitoring and manipulating biological cells. Different approaches have been introduced to increase the electrochemical active surface area of electrodes. For example, coatings with high intrinsic conductivity have been investigated to fulfil the above mentioned requirements of recording and stimulation electrodes. Examples are iridium oxide (IrOx) [135–137], carbon nanotubes [138, 139], and conductive polymers (CPs) like poly(3,4-ethylenedioxythiophene) (PEDOT) [140–142] and polypyrrole (PPy) [140, 143, 144]. Besides the electrochemical characteristics, the chronic stability of electrodes is a crucial aspect especially for implantable devices. Different aspects such as abiotic mechanisms comprising electrode related degradation [17, 18] and biotic mechanisms dictated by interactions with the neural tissue [14, 15, 17] can cause a failure of conductive films.

Within this work, poly(3,4-ethylenedioxythiophene) doped with poly(styrene sulfonate) (PEDOT:PSS) coated neural probes were produced utilizing two different methods; spin-coating and electrochemical deposition. The electrochemical properties of the different coatings were compared with regard to impedance and CSC. Furthermore, the abiotic stability was determined utilizing an accelerated ageing test and the electrochemical robustness by applying CV charge-discharge cycles.

5.1. Conducting polymer PEDOT:PSS

Conductive polymers (CPs) possess the unique feature of electrical activity that is realized by doping the conjugated bonds within the backbone of the organic polymer [145, 146]. The double bonds with their delocalized electrons can be n-doped or p-doped by introducing or removing electrons, respectively, obtaining a conductivity similar to those of semiconductors ($10^{-6} - 10^2$ S/m) [145]. Despite the lower conductivity compared to conventional metals, CPs exhibit low impedance and high CSC and, CIC while maintaining small electrode geometry [134, 142]. Main reason for the superior properties is that these polymers exhibit both electronic and ionic conductivity involving the entire polymer volume in charge transport processes [147]. Additionally, the coatings increase the surface roughness or porosity, resulting in a high ratio between the electrochemical surface area (ESA) and geometric surface area (GSA). The volumetric capacitance has been introduced to describe the mixed conductivity of CPs [148]. In contrast to the standard electrode/electrolyte interfaces, where the capacitance depends on the surface area [67] (*e.g.* 50-60 μFcm^{-2} for Pt electrodes [149, 150]), the capacitance of CPs is believed to scale with volume (6-57 Fcm^{-3} [148]). Furthermore, in combination with flexible substrate materials, the soft mechanical properties of CPs make them ideal candidates to improve chronic *in vivo* stability of neural implants by reducing the mechanical mismatch between electrode and biological tissue [151] (see Sections 2.1.1 and 4.1). S. Baek, *et al.* [152] have shown that the choice of dopant has an effect on the mechanical characteristics. Dopants can further alter the electrochemical [141, 152, 153] and biological properties [141, 153] giving the opportunity to engineer customized CPs for various applications. Overall, the properties of CPs are dictated by the type of CP and dopant, and the deposition method.

Several CPs have been introduced, however, PEDOT doped with poly(styrene sulfonate) (PSS) (see Figure 5.1) has been reported to show outstanding electrochemical properties and stability [140, 143, 155, 156]. PEDOT:PSS coatings can be prepared by vapour-phase [157, 158] or electrochemical polymerization [140]. For the vapour-phase polymerization, PEDOT:PSS is chemically synthesized from an aqueous solution of 3,4-ethylenedioxythiophene (EDOT) by oxidation using Fe(III) salts and by incorporating PSS as counterions resulting in a blue polymer powder [157]. Such chemically polymerized PEDOT:PSS is commercially available as ready-to-use mixtures. The company Heraeus, for example, offers suspensions with different PEDOT:PSS ratios and conductivities [159]. These solutions are spin-coated, drop-casted, or ink-jet printed to obtain thin polymer films and can be easily incorporated into MEMS fabrication [160–163]. Spin-coated PEDOT:PSS films are believed to consist of PEDOT-rich and PSS-rich regions organized in a pancake-like morphology (see Figure 5.1) [154, 164]. It has been shown that the addition of solvents to the suspension can improve the conductivity, stability, and adhesion of the resulting PEDOT:PSS films. 3-glycidoxypropyltrimethoxysilane (GOPS) is
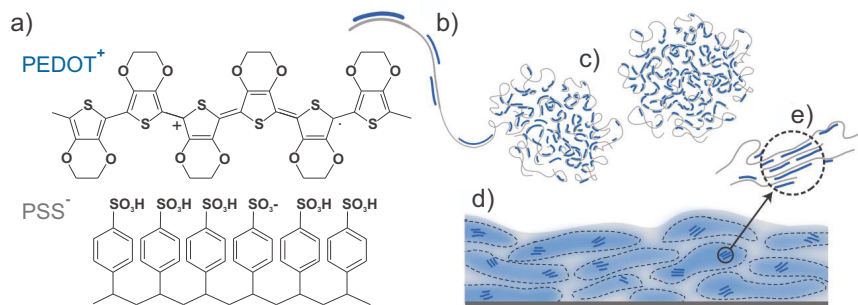
Figure 5.1.: Chemical structure of PEDOT:PSS (a) and morphology of spin-coated films: PEDOT oligomers polymerize onto PSS chains (b), formation of gel-like particles in dispersion (c) resulting in pancake-like morphology with PEDOT-rich (blue) and PSS-rich (grey) regions (d). Aggregates within the particles enhance intrinsic conductivity (e). Figure adapted from [154].

commonly used as adhesion promoter and to improve the mechanical stability [165] whereas dodecylbenzenesulfonic acid (DBSA) added as surfactant facilitates an even film formation [166]. Ethylene glycol (EG) and dimethyl sulfoxide (DMSO) enhance the conductivity of PEDOT:PSS [154, 167]. In contrast to the vapour-phase synthesis, electrochemical polymerization of EDOT in aqueous solution with poly(sodium 4-styrenesulfonate) (NaPSS) is performed under electrical bias employing galvanostatic, potentiostatic or potentiodynamic methods [140, 168]. This approach requires a conductive material that oxidizes the monomer into high order oligomers stabilized by the polyanion NaPSS. In contrast to spin-coated films, electrochemical deposition results in globular or cauliflower-like morphologies [168, 169]. By tuning the polymerization parameters, the morphology, and conductivity of the PEDOT:PSS films can be controlled [168, 170].

5.2. Experimental section

To produce PEDOT:PSS coated electrodes, two techniques, namely electrochemical deposition and spin-coating were utilized, and compared. For both methods, a 100 nm thick Pt layer with GSA of 113 μm^2 sandwiched between two PaC layers was used as WE (see Chapter 4.5).

5.2.1. Electrochemical deposition

The electrochemical polymerization was carried out using the potentiostat CHI10-30B from CHI Instruments (Austin, USA). A coiled Pt wire was used as CE and a DRIREF-2 Ag/AgCl Reference Electrode (World Precision Instruments, USA) as RE. To ensure a uniform deposition, the Pt surface was electrochemically cleaned by means of 10 CV cycles (-0.6 to +0.9 V vs. Ag/AgCl, 0.1 V/s, 0.1 M PBS), rinsed with ultrapure water and activated using O_2 plasma (80 W, 0.8 mbar, 3 min). The electrodes were coated by potentiostatic polymerization for 7-20 s at 1 V from 0.1 % (w/v) 0.01 M EDOT (Sigma-Aldrich, Germany) and 0.7 % (w/v) NaPSS (Sigma-Aldrich, Germany) prepared in ultrapure water. The deposition charges for the different times were determined by integrating the current over time and dividing by the GSA.

5.2.2. Spin-coating

The wafer-scale coating with PEDOT:PSS was enabled using a PaC sacrificial layer. Probes were fabricated based on the single-layer process described in Section 4.4.1. During the dry etching step, the probe shape and the bondpads were defined separately from the electrode openings. Before patterning the electrode sites, a 4 μm (6.5g) thick PaC sacrificial layer was deposited. To facilitate the release of this layer, Micro90 soap solution was spin-coated prior to the PaC deposition. Dry etching of the electrode sites was performed as described in Section 4.4.1 by introducing the openings into the passivation and the sacrificial layer.
For the preparation of the PEDOT:PSS solution, 93.9 % (v/v) Clevios PH-1000 (Heraeus Holding GmbH, Germany) was mixed with 5 % (v/v) EG (Sigma-Aldrich, Germany), 1 % (v/v) GOPS (Sigma-Aldrich, Germany), and 0.1 % (v/v) DBSA (Sigma-Aldrich, Germany) (similar to [160]). After stripping the remaining AZ 10XT (MicroChemicals, Germany), the electrodes were spin-coated with the PEDOT:PSS. A first layer was spin-coated, shortly soft baked to remove most of the solvent and followed by several layers of PEDOT:PSS until a desired thickness was achieved. After peeling off the sacrificial layer with a few drops of water and hard baking the PEDOT:PSS to improve film stability, the samples were soaked for several hours in water to remove Micro90 residues and excess low molecular weight compounds within the PEDOT:PSS coating. The detailed fabrication protocol is attached in the Appendix A.5.

5.2.3. Iridium oxide as adhesion layer

The details of the fabrication are provided in the Appendix A.6 and shortly described here. The probes were produced based on the single-metal-layer process

(see 4.4.1) thus, after patterning the interconnects and the electrode sites and before the deposition of the passivation layer, an additional photolithography step was introduced to cover the recording electrodes with IrOx. The same lift-off process used to structure the first metal layer was utilized. However, the spin-coating speed was adjusted to ensure a good lift-off as a thicker IrOx film of 450 nm was sputtered in contrast to the first metal layer with a total thickness of 120 nm. The sputtered IrOx was provided from the cleanroom facility at the Institut für Werkstoffe der Elektrotechnik (IWE-1), RWTH Aachen University (Germany).

5.2.4. Characterization

Electrochemical impedance: The electrochemical impedance of the different PEDOT:PSS coatings in comparison to bare Pt electrodes was measured by applying a 10 mV alternating voltage stimulus and scanning from 10 Hz to 10 MHz as described in Section 3.2.1. The impedances of bare Pt or Au electrodes were recorded after cleaning the surface by means of 10 CV cyles (-0.6 to +0.9 V vs. Ag/AgCl, 0.1 V/s, 0.1 M PBS).

Charge storage capacity (CSC): The redox characteristics of the PEDOT:PSS coatings were determined using CV cycles (see Section 3.2.2). For the measurements, the potential window was restricted to -0.6 to 0.9 V (vs. Ag/AgCl), the water window of Pt, to avoid any degradation of the electrodes. The samples were characterized in 0.1 M PBS and with a scan rate of 0.1 V/s. The CSC [mC/cm^2] was averaged over 10 cycles and derived using:

$$CSC = \frac{1}{v} \int_{E_c}^{E_a} |i| dE \tag{5.1}$$

where E is the WE potential [V], i the measured current density [mA/cm^2], E_a and E_c the anodic and cathodic potential limits [V], respectively, and v the scan rate [V/s] [135].

Ageing test: Storing implants in electrolyte solution at elevated temperatures is commonly used to study the long-term robustness and passive degradation mechanisms of electrode coatings. The resulting accelerated ageing factor (AAF) can be estimated by the Arrhenius equation [171]:

$$AAF = Q_{10}^{\frac{T_{accelerated}-T_{target}}{10}} \tag{5.2}$$

where T_{target} is the ambient temperature [°C] (for implants: 37 °C) and $T_{accelerated}$ the accelerated ageing temperature [°C]. The factor Q_{10} is commonly set to 2 as a conservative approximation for determining the ageing factor of polymers [171]. To validate the abiotic stability, PEDOT:PSS films were stored in 0.1 M PBS (pH=7) at 70 °C for 168 h. Petri dishes with a slit were taken as storage containers for the samples (see Figure A.2). The flexible probes soldered to custom-made

PCBs were inserted through the slit and glued with PDMS. PDMS (Sylgard 184, Dow Corning, USA) was prepared by thoroughly mixing base and curing agent at a ratio of 10:1 and degassing the mixture at -20 °C for a couple of days to remove gas bubbles. As the frontend of the PCB would be in contact with the electrolyte, it was made sure, that the PCB was completely sealed with PDMS. After a storage time of 48 and 168 h, the samples were taken out of the oven and let cool down to RT for determining impedance and CSC as described above. At the end of the study, the electrode coatings were additionally imaged using a digital microscope (VK-X150, Keyence Deutschland GmbH, Germany).

Electrochemical stability: The adhesion and robustness of the PEDOT:PSS films were investigated by applying electrochemical stress in form of CV charge-discharge cycles. Blocks of 50-100 cycles were applied (-0.6 to +0.9 V vs. Ag/AgCl, 0.1 V/s, in 0.1 M PBS) followed by an impedance measurement and an optical validation under a digital microscope (VK-X150, Keyence Deutschland GmbH, Germany.

Surface roughness: The roughness of Pt and IrOx films was characterized using small Si test pieces that had the same stack as the wafers used for probe fabrication (Si/PaC/Ti/Pt or Si/PaC/Ti/Pt/IrOx). However, the test samples did not undergo fabrication steps following the metal deposition, such as deposition of PaC as passivation layer and dry etching to expose electrode sites. Areas of $10x10 \, \mu m^2$ were scanned and the RMS roughness determined as descried in Section 3.3.

Imaging: Besides optical microscopy, the morphology, adhesion and thickness of the coatings were further analysed by SEM and FIB sectioning (see Section 3.1).

5.2.5. Statistical analysis

Continuous variables such as impedance and CSC are reported as median [median± 95 % CI (confidence interval)], unless otherwise indicated. The various PEDOT:PSS coatings were tested for difference in regard to normalized impedance and CSC. The normality was rejected for some of the studied variables after performing the Shapiro-Wilk test. Therefore, the non-parametric Kruskal-Wallis H-test was applied to compare the properties of electrochemical deposited and spin-coated PEDOT:PSS. When a significant difference was observed using the Kruskal-Wallis H-test, post-hoc pairwise testing was performed using Dunn's test with Bonferroni correction. If p-values lower than 0.05 ($p < 0.05$), differences in studied variables were considered to be statistically significant. The tests were implemented in Python 3 [76] using the module SciPy.

5.3. Spin-coated and electrochemically deposited PEDOT:PSS films

As part of the effort to develop intracortical implants two different methods were investigated to establish a PEDOT:PSS coating on flexible MEAs. Comparisons were made between electrochemically deposited PEDOT:PSS obtained under potentiostatic condition and spin-coated PEDOT:PSS crosslinked with EG, GOPS and DBSA. The fabrication challenges, morphology, electrochemical performance and coating stability were considered for the benchmarking study. The flexible intracortical probes A-MEA-16 comprising 100 nm thick micro-cracked Pt microelectrodes with a GSA of $113\,\mu m^2$ were used to study the different coatings (see Chapter 4.5). To minimize batch-to-batch variations, all probes used for either the electrochemical deposition or the spin-coating were produced within one fabrication run.

5.3.1. Fabrication challenges of spin-coated PEDOT:PSS

To establish a high through-put electrode coating procedure, spin-coating was established by implementing a PaC sacrificial layer within the fabrication process. During the microfabrication of PEDOT:PSS coated probes, challenges were encountered and are discussed here in detail. Prior to structuring the electrode sites, a PaC sacrificial layer in combination with a soap solution was deposited. Electrodes were exposed via RIE using a photoresist etch mask. Following the UV exposure, gas bubbles were seen underneath the PaC sacrificial layer (see Figure 5.2 a). As stated in Chapter 4.4.3 this phenomenon can be induced by the off-gassing of resists during UV exposure in combination with the gas permeability of PaC [85] and seems to occur more frequently when a release layer is used. The etch mask utilized for defining the probe shape was $20\,\mu m$ thick and exposed with a dose of $2100\,mJ/m^2$. In contrast to this mask, for exposing the electrode sites a $13\,\mu m$ thick resist exposed with $900\,mJ/cm^2$ was used to reduce the bubbling as this issue is pronounced for higher exposure doses. This solution is only applicable when the thickness of PaC films in combination with the etch rates of polymer and resist allow the use of a thinner etch mask. Thus, the gas bubbles could not be completely avoided and were mainly observed for big areas not covered with resist after development. At this point of fabrication, the wafer edge and the area with the alignment markers were free of resist (see Figure 5.2 a). Not removing the gas bubbles can lead to crack formation within the resist layer during the etching process. These cracks are transferred to the underlying PaC films. Since an intact sacrificial layer is crucial for a successful dry release the big bubbles occurring in non-critical areas were pierced and within the next processing step, the RIE, the vacuum removed the bubbles.
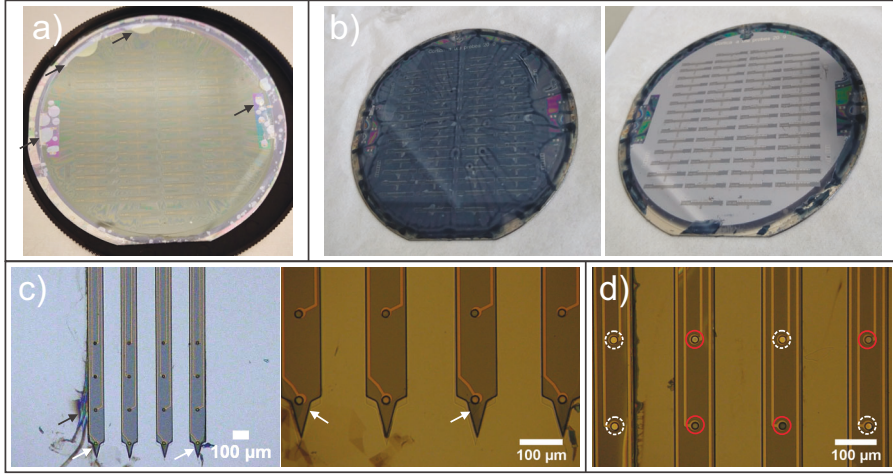
Figure 5.2.: Challenges of spin-coated PEDOT:PSS: a) Gas bubbles after UV exposure of the photoresist etch mask (arrows). b) After exposing the electrode openings, PEDOT:PSS solution was spin-coated and soft-baked over the entire wafer (left image). The release of the PaC sacrificial layer left PEDOT:PSS films confined on top of the electrodes (right image). c) After dry releasing the sacrificial layer, bluish residues were seen, especially around the shank tips (white arrows) and residues of the release soap solution were observed on top of the wafer around the probes (black arrow). d) Complete (white rings) or partial (red rings) peeling off of the PEDOT:PSS coatings during the release of the sacrificial layer.

After spin-coating and soft-baking the conductive polymer, the PaC sacrificial layer was released to obtain PEDOT:PSS coated electrodes 5.2 b). A complete dry release of the sacrificial layer was not possible. Therefore with a tweezer, the sacrificial layer was lifted from one edge of the wafer and a few drops of water were applied between sacrificial layer and carrier wafer to facilitate the release (see Figure 5.2 a). Furthermore, the process from spin-coating the soap solution to dry releasing the sacrificial layer should be completed as quickly as possible. On the on hand, a prolonged contact to the release agent without the PaC deposition can cause a partial release of the probes impeding accurate alignment of the following process steps. On the other hand, with greater time frame it seems to be more difficult to remove the sacrificial layer without leaving residues. Blueish residues were occasionally observed around the electrode openings, mainly for the electrodes at the shank tip (see Figure 5.2 c). By changing the design this phenomenon might be avoided, for example, by increasing the distance between shank tip and electrode. Additionally, the electrode coating was completely or partially peeled off during the release of the sacrificial layer, which was pronounced for thicker layers of PEDOT:PSS (see Figure 5.2 d). It is assumed that above a certain conductive polymer thickness, the edges of the electrode openings are
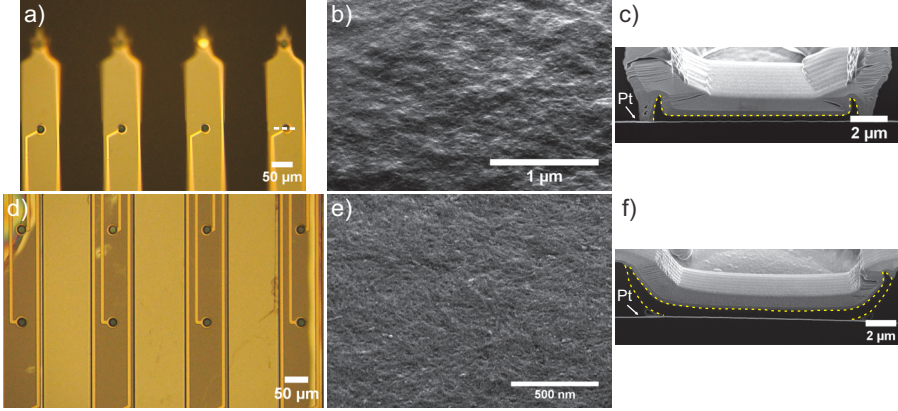
Figure 5.3.: Images of electrochemically deposited (a-c) and spin-coated (d-f) PEDOT:PSS: Electrodeposition was performed at a charge of $90\,mC/cm^2$ and the spin-coated film was obtained upon stacking 3 layers. Optical images reveal the blue colour of the PEDOT:PSS covering the microelectrodes (a, d). SEM pictures show the globular (b) and the sponge-like (e) morphology of electrochemically deposited and spin-coated PEDOT:PSS, respectively. The white dashed line (a) indicates the slicing plane for FIB (c, f). FIB sections depict the electrodeposited PEDOT:PSS confined to the diameter of the Pt electrode (c) and the spin-coated film covering additionally the sidewalls of the electrode opening (f). The PEDOT:PSS coatings are bordered in yellow.

completely covered with PEDOT:PSS. Therefore, a release of the sacrificial layer without pulling off the coating is not feasible anymore. This resulted in thickness variations of the PEDOT:PSS films within probes indicated by various shades of blue (see Figure 5.2 d). To produce thicker PEDOT:PSS films, the height of the sacrificial layer should be increased to ensure a release without removing the electrode coatings. Consequently, a thicker etch mask and therefore, higher exposure dose would be needed to pattern the electrode sites enhancing the appearance of gas bubbles underneath the PaC sacrificial layer. As described above, such bubbles facilitate crack formation during the RIE, which increases the failure rate of the microfabrication process.

5.3.2. Coating morphology and thickness

Optical images show the typical blue colour of the PEDOT:PSS films for both methods (see Figure 5.3 a, d). Furthermore, SEM images depict the globular and the sponge-like morphology for electrochemical deposition and spin-coating, respectively (see Figure 5.3 b, e). The coating thicknesses were determined from the centre of the electrodes based on FIB sectioning and averaged for two electrodes from 1-2 neural probes for each condition (see Figure 5.4). The differences in the edge coverage

when comparing both coatings (discussed below) was neglected for the thickness measurements. For spin-coating, the coating was performed by starting with a thin layer obtained at a spin speed of 3000 rpm followed by several layers spin-casted at 500 rpm. With this approach, the minimum thickness spin-coated onto the Pt electrodes was 375±64 nm (mean±std, n=2) (see Figure 5.4). With 4 spin-coated layers (1x3000 rpm and 3x500 rpm), a thickness up to 780 nm could be reached. For electrochemical deposition, the potentiostatic polymerization was performed at 1 V for 7-20 s. By integrating the current response over time in relation to the GSA, the deposition charges were obtained. The corresponding deposition times for the different charges are provided in Table A.1. To obtain a confluent CP layer via electrochemical polymerization, a minimum deposition charge of 50 mC/µm^2 was needed whereas above 220 mC/µm^2, PEDOT:PSS overgrew the electrode opening. To validate the influence of film thickness on electrochemical performance, deposition charges of 50, 90, 140 and 220 mC/µm^2 were considered resulting in thicknesses of 130-560 nm whereas varying the number of spin-coated layers from 2-5 yielded thicknesses of 450-950 nm (see Figure 5.4). An overview with optical images, SEM images and FIB sections of the different thicknesses obtained with either electrochemical deposition or spin-coating is provided in the Appendix (see Figure A.5 and Figure A.8).

To compare the films obtained with both methods, the thicknesses for the different conditions were determined by least-squares linear regression. Typically, the nucleation and growth process of EDOT under potentiostatic or galvanostatic conditions follows the parabolic rate law (see Section A.8.2.1). However, the initial increase for low deposition charges was not relevant within this work as a confluent PEDOT:PSS layer was obtained above 50 mC/cm^2. Therefore, a linear fit was applied for the charges 50-220 mC/cm^2 to specify the film thicknesses obtained via electrochemical deposition.

Comparing both methods, thicker coatings could be obtained with spin-coating. Furthermore, FIB sections reveal that the films completely covered the electrode sidewalls (see Figure 5.3 f) whereas electrochemical deposition resulted in coatings confined to the size of the Pt electrodes (see Figure 5.3 c). This is in accordance with the chemical nature of electrochemical polymerization of PEDOT:PSS as a conductive material is needed to oxidize the monomer. For deposition charges above 50 mC/µm^2, the PEDOT:PSS coating was roughly 1 µm smaller in diameter compared to the Pt electrode with a GSA of 113 µm^2 (see Figure 5.3 c and Figure A.5). This is similar to H. Zhou, *et al.*'s work [172] where the PEDOT:PSS films had a diameter of 80 µm and the underlying Pt a diameter of 100 µm however, for a deposition in galvanostatic mode. Optical images reveal the presence of a thin polymer layer at the electrode edge. However, this layer at the edge went off after the 10 CV cycles used to determine the CSC (see Figure A.6). It is assumed that PaC residues around the electrode edges cause a weak adhesion of the deposited PEDOT:PSS resulting in a lift-off after a few charge-discharge cycles. Pre-treating the probes with a short Ar plasma (0.4 mbar, 100 W, 3 min) before
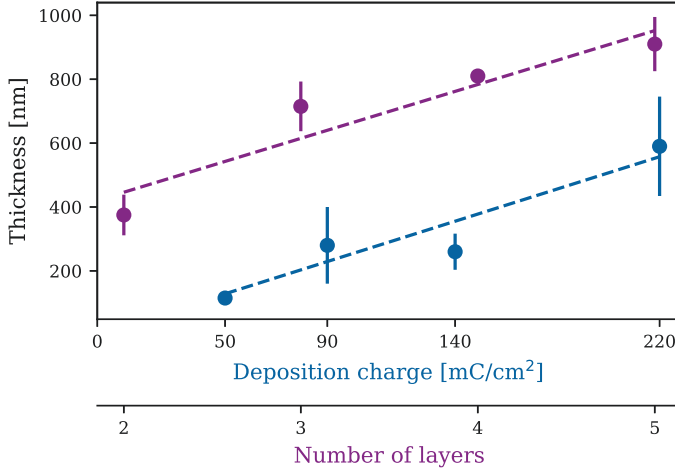
Figure 5.4.: PEDOT:PSS film thicknesses (mean±std, n=2) for various deposition charges obtained via electrochemical deposition (blue dots) and upon stacking of spin-coated layers (purple dots). One section for 4 layers is missing due to facility closure. Linear regressions (dashed lines) were used to determine the thicknesses for the different conditions, R^2=0.845 (blue line) and R^2=0.918 (purple line).

the PEDOT:PSS deposition resulted in a better edge coverage (see Figure A.7) supporting the assumption that PaC residues influence the PEDOT:PSS growth, especially around the electrode edges. However, the Ar etch had an impact on the electrochemical properties. For deposition times of 15 s, a deposition charge of 140 mC/cm² was observed without pretreatments whereas for the pretreated electrodes, a charge of 490-590 mC/cm² could be determined. As shown by V. Castagnola, *et al.* [168] the surface quality has an influence on the growth of the conductive polymer. Therefore, for a better comparison of both coating methods, the Pt electrodes were not pretreated. This highlights that the RIE process to expose the electrode openings has to be well controlled to ensure a residue free electrode and consequently, a good adhesion between the PEDOT:PSS and the underlying metal layer.

5.3.3. Electrochemical performance

To compare the recording and stimulation capabilities, the different PEDOT:PSS coatings were characterized in regard to impedance and CSC using EIS and CV, respectively. For the experiments, 12 electrodes from 4 different probes were averaged for electrochemical deposition and 3 different probes each consisting of 16 electrodes for the spin-coating. Outlying electrodes with fabrication defects
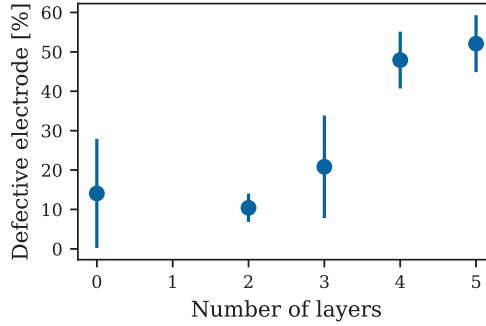
Figure 5.5.: Fraction of defective electrodes for different layers of spin-coated PEDOT:PSS. Electrodes with an impedance of $>10\,M\Omega\cdot\mu m^2$ and $<1\,M\Omega\cdot\mu m^2$ at $1\,kHz$ were excluded as outliers. Bare Pt electrodes used for electrochemical deposition are represented by 0 layers. Single dot: mean±std, n=3 probes (except for 0 layers where n=4).

not related to PEDOT:PSS resulting in an impedance higher than $10^3\,M\Omega\cdot\mu m^2$ at $1\,kHz$ were excluded. For spin-coating, impedances below $1\,M\Omega\cdot\mu m^2$ at $1\,kHz$ were removed as these low values resulted from residues of the sacrificial layer around the electrode opening and therefore, increased the ESA (see Figure 5.2 c and Figure A.9). Furthermore, impedances above $10\,M\Omega\cdot\mu m^2$ were excluded as for an intact PEDOT:PSS coating the expected impedance value was a few $M\Omega\cdot\mu m^2$ at $1\,kHz$. This was determined empirically and derived from the impedance values of electrochemically deposited PEDOT:PSS assuming a similar behaviour for both methods as show by D. Koutsouras, *et al.* [173]. The thicker spin-coating films (equivalent to layers 4-5) resulted in a higher percentage of outlier electrodes compared to the probes with bare Pt electrodes (equivalent to 0 layers) (see Figure 5.5), which could be caused by the issues during the release of the sacrificial layer (see Section 5.3.1).

EIS is a powerful method to describe how input signals such as neuronal activity are translated at the electrode/electrolyte interface dependent on their frequency components. Figure 5.6 shows the bode plot of the impedance for bare Pt electrodes with a GSA of $113\,\mu m^2$ after the electrochemical cleaning. With decreasing frequency, the electrode impedance is monotonically increasing meaning that input signals with low frequency contents can be lost within the high thermal noise, which scales with impedance. Furthermore, the impedance was capacitance dominated over the entire frequency range as additionally indicated by the phase angle. At $1\,kHz$, Pt had an impedance of $744.180\,[646.278\text{-}842.083]\,M\Omega\cdot\mu m^2$, median $[95\,\%\,CI^1]$ (n=12). The impedances at $1\,kHz$ are specified here for a comparison of the different thicknesses and methods. Even though, the entire frequency range is of interest, as

---

[1]Confidence interval, 95 % CI of median = median±1.57·IQR/n$^{0.5}$ (IQR = interquartile range)

LFPs and APs reside in the time frames of less than 300 Hz and 300–10,000 Hz, respectively [174]. Furthermore, fast stimulation pulses commonly have a time range of more than 1 kHz [175].
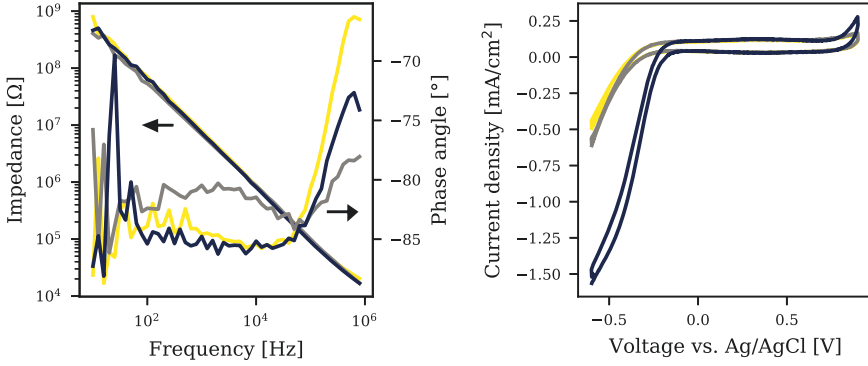
Figure 5.6.: Electrochemical properties of three Pt microelectrodes with a GSA of 113 μm². Representative bode plots (left): High impedance electrodes are sensitive to noise, mainly visible here for the phase angle measurements as the impedance is depicted in a double-logarithmic scale. Representative current over voltage curves (right): CV scans obtained within the water window of Pt (-0.6 to +0.9 V (vs. Ag/AgCl)) at a scan rate of 0.1 V/s.

Figure 5.7.: Representative impedance spectra of electrochemical deposited (top) and spin-coated (bottom) PEDOT:PSS for the different thicknesses.

5. PEDOT:PSS as electrode coating material

The PEDOT:PSS films produced with both methods caused a considerable reduction in the impedance compared to bare Pt electrodes. Representative bode plots for the different PEDOT:PSS films are prese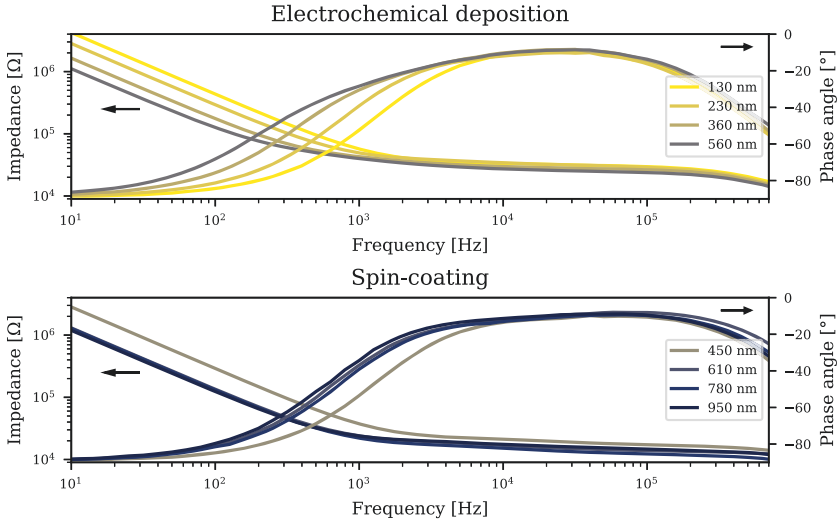nted in Figure 5.7. Especially in the low frequency range ($<10^3$ Hz), a decrease was observed by around two orders of magnitude. All thicknesses exhibited a similar trend, with an increasing impedance for decreasing frequency. Above a certain cut-off frequency ($\approx 10^3$ Hz), the impedance of PEDOT:PSS changed from a capacitive into a resistive behaviour, as the impedance plateaued into a frequency-independent response [173, 176]. This characteristic was supported by the course of the phase angle with the rise from -90° to 0°. The frequency-independent response seems not to be affected by the polymer thickness. In contrast to low frequencies where the impedance is dominated by the electrode and its double layer capacitance, at high frequencies, the impedance is determined by the solution resistance. The solution resistance scales with the GSA and not the ESA and thus, is independent of any electrode coating [71]. For frequencies above 10^5 Hz, parasitic capacitances caused a drop of the phase angle, which is unavoidable for high frequency circuits.

For both methods, with increasing thickness a decrease in impedance could be observed except for the thickest layer obtained by spin-coating (see Figure 5.8). The latter showed the highest variation, probably due to the issues encountered during the release of the sacrificial layer and the resulting thickness variations (see Section 5.3.1 and Figure 5.2). In general, the spin-coating resulted in more outliers compared to the electrochemical deposition except for the thickness of 610 nm. As the CP film was deposited at once for the entire wafer using spin-coating, the thickness varied depending on the device location on the wafer. Furthermore, the impedances of the spin-coated films were lower compared to electrochemical deposition (see Figure 5.8). As the capacitance of PEDOT:PSS scales with volume [148], lower impedance values should result from thicker films. However, when comparing similar thicknesses, such as 500-700 nm, the normalized impedances of spin-coated PEDOT:SS were still significantly lower. The impedance at 1 kHz of electrochemically deposited PEDOT:PSS with a thickness of 360 nm was 4.552 [4.170-4.934] MΩ·µm², median [95 % CI] (n=12) (see Figure 5.8) whereas for spin-coating with a thickness of 450 nm, a further reduction to 3.232 [3.112-3.353] MΩ·µm², median, [95 % CI] (n=43) was observed. Due to the high amount of outliers, no significant difference was seen for the thicknesses 300-500 nm. Among all thicknesses, the lowest and most stable (defined by considering fraction of defective electrodes (see Figure 5.5) and number of outliers (see Figure 5.8)) impedance was obtained with spin-coating PEDOT:PSS in 3 layers resulting in a film thickness of 610 nm. The corresponding normalized impedance at 1 kHz was 2.650 [2.601-2.699] MΩ·µm², median [95 % CI] (n=38). A comparison to similar works in regard to impedance can be found in the Appendix (see Table A.2).

In the next step, the CSC of the PEDOT:PSS coatings were determined using CV cycling. CV is a common tool to study charge transfer processes at the electrode/electrolyte interface. The enclosed area of a CV cycle is proportional
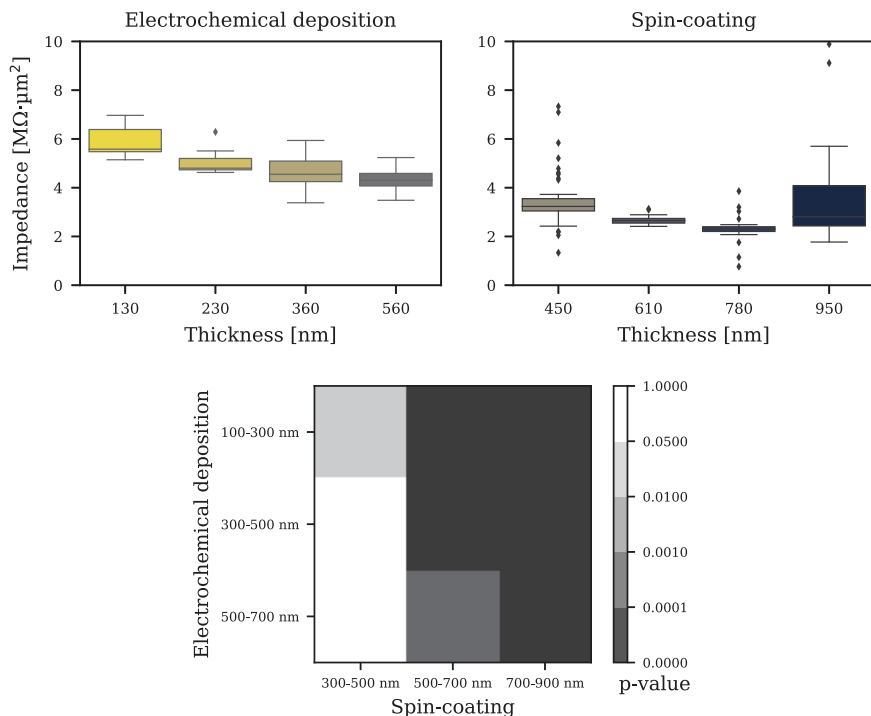
Figure 5.8.: Normalized impedance for increasing thicknesses of electrochemically deposited (top left) and spin-coated (top right) PEDOT:PSS. In the boxplots, left: n=(12, 12, 12, 12), right: n=(43, 38, 25, 23), line: median, box: 1st-3rd quartile, whiskers: 1.5x interquartile range above and below the box, and diamonds: outliers. P-value matrix (bottom) after performing the Dunn's post-hoc test with Bonferroni correction. P-values between 0.05 and 0.01 indicate statistical significance whereas values below 0.01 denote highly significant differences.

to the CSC within the examined potential window. Figure 5.6 depicts the CV curves of bare Pt electrodes within their water window of -0.6 to +0.9 V (vs. Ag/AgCl) obtained at a scan rate of 0.1 V/s. For potentials above -0.2 V, constant positive and negative current responses were observed originating from capacitive charging and discharging. However, for negative potentials, an increased cathodic current was measured indicating faradaic charge transfer processes. The maximum current density varied between -0.5 to -1.5 mA/cm^2 (at -0.6 V) for the different Pt microelectrodes as shown in Figure 5.6. Oxygen reduction occurs at potentials less than +0.25 V (vs. Ag/AgCl) resulting in an increased current response in the cathodic region [177–179]. For micro-sized Pt electrodes, the cathodic current density is further increased compared to macroelectrodes [179] as the mass transport
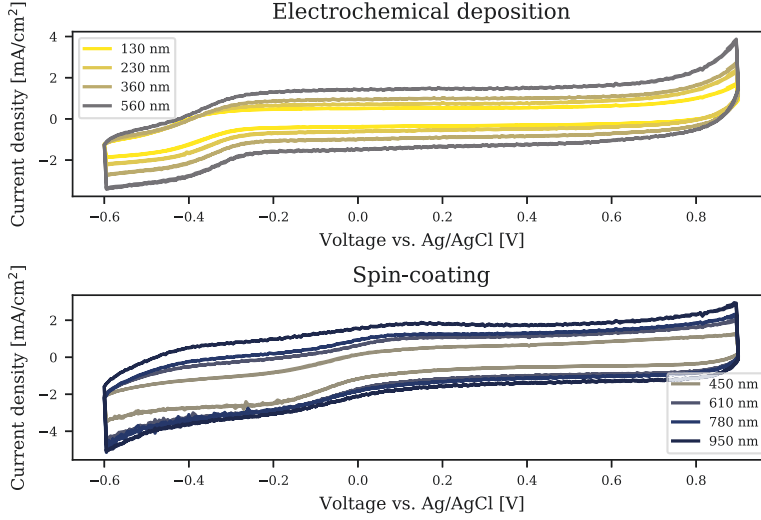
Figure 5.9.: Representative CV cycles of electrochemical deposited (top) and spin-coated (bottom) PEDOT:PSS for the different thicknesses for a scan rate of 0.1 V/s.

at the interface is limited rather by spherical than planar diffusion [180]. To ensure that the increased cathodic current was material independent and not caused by the micro-cracks within the Pt layer, PaC based probes with Au were produced since for e-beam evaporated Au, no cracks were found (see Section 4.4.3). The CVs for both metallic electrodes were similar in shape with the increased cathodic current below -0.2 V (vs. Ag/AgCl) (see Figure 5.6 and Figure A.3). This is in accordance with S. Cogan, *et al.*'s work [179], where the increased cathodic current dominated by oxygen reduction was observed for negatively polarized Pt as well as Au electrodes. At the anodic potential limit, the increase in current indicated the start of oxygen evolution, which was pronounced for higher voltages (see Figure A.3).

The areas enclosed by the CV curves for the different PEDOT:PSS coatings were bigger compared to the bare Pt electrodes resulting from higher CSCs (see Figure 5.6 and Figure 5.9). PEDOT:PSS films exhibit high surface porosity and additionally, show electronic and ionic conductivity involving the entire polymer bulk in charge transport processes resulting in increased charge storage properties in contrast to Pt electrodes [147, 148]. For negative potentials, an increase in the cathodic current response was observed, which might be attributed to the underlying metal and the aforementioned cathodic oxygen reduction processes. Furthermore, the CV of electrochemically deposited films approached a rectangular shape without any characteristic redox peaks [181] whereas for spin-coating, broad reduction and oxidation peaks were observed around −0.4 to +0.1 V and −0.2 to +0.4 V [182].
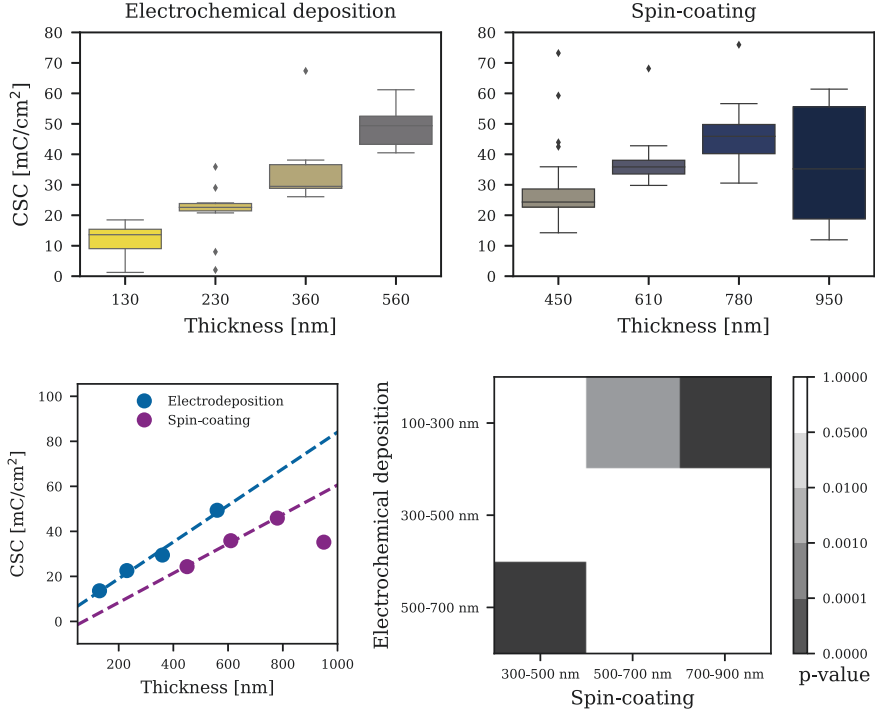
Figure 5.10.: CSC for increasing thicknesses of electrochemically deposited (top left) and spin-coated (top right) PEDOT:PSS. In the boxplots, left: n=(12, 12, 12, 12), right: n=(41, 37, 24, 21), line: median, box: 1st-3rd quartile, whiskers: 1.5x interquartile range above and below the box, and diamonds: outliers. Linear regressions (bottom left, dashed lines) of CSCs (dots: median) for both types of PEDOT:PSS with R^2=0.993 (blue line) and R^2=0.998 (purple line). P-value matrix (bottom right) after performing the Dunn's post-hoc test with Bonferroni correction. P-values greater than 0.05 show no significant difference and are coloured white whereas p-values below 0.05 denote significant differences.

Nevertheless, all CVs approached a rectangular shape indicating that the capacitive charge transfer dominates.

610 nm thick spin-coated films had a CSC of 35.863 [34.697-37.029] mC/cm^2, median [95 % CI] (n=37), which is 31 times larger than the underlying metal with 1.141 [1.035-1.299] mC/cm^2, median [95 % CI] (n=12). The CSC of 360 nm thick electrochemically deposited PEDOT:PSS was 26 times greater with 29.488 [25.961-33.014] mC/cm^2, median [95 % CI] (n=12) compared to bare Pt electrodes. The CSC values for the different thicknesses are presented in Figure 5.10. As expected from the impedance analysis, the thickest layer obtained via spin-coating exhibited

the highest deviations regarding CSC. Except this thickness, a linear dependency could be identified between CSC and polymer thickness for both methods (see Figure 5.10, bottom left). A linear correlation suggests that the entire PEDOT:PSS bulk contributes to the charge transfer processes at the electrode/electrolyte interface. Among all thicknesses, the highest CSC was obtained for 560 nm thick electrochemically deposited PEDOT:PSS (49.382 [45.195-53.570] mC/cm^2, median [95 % CI] (n=12)) and 780 nm thick spin-coated PEDOT:PSS (45.899 [42.825-48.972] mC/cm^2, median [95 % CI] (n=24)). A comparison to similar works in regard to CSC is summed up in the Appendix (see Table A.2).

In contrast to the EIS, where spin-coated PEDOT:PSS showed significantly lower impedances than the electrochemical deposition the CSCs were similar for both methods. No significant differences were observed for comparable thicknesses such as 300-500 nm and 500-700 nm. Additionally, no difference was seen between 230 nm, 360 nm and 560 nm thick electrochemically deposited and, 450 nm, 610 nm and 780 nm thick spin-coated PEDOT:PSS, respectively (p>0.05) (see Figure 5.10). The CSCs from 950 nm spin-coated PEDOT:PSS can be neglected due to the high variations. CPs like PEDOT:PSS exhibit electronic and ionic conductivity involving the entire bulk in charge transfer processes. As a consequence, with thicker polymer films, the capacitance should increase resulting in higher CSC. As thinner electrochemically deposited films exhibited similar CSCs to thicker spin-coated films, it is assumed that the charge transfer processes are different for both coating methods.

Similar to the trend observed within this work (see Figure 5.10), a linear dependency was identified between coating thickness and CSC for spin-coating (stacked layers) [183] and electrochemical deposition [181] in previous works. D. Koutsouras, *et al.* [173] showed that the impedances and capacitances were comparable for spin-coated and electrochemically deposited PEDOT:PSS films with similar thicknesses. However, polymer films obtained with both methods have not yet been compared in regard to CSC. Especially, a comparative study for varying thicknesses is still missing.

5.3.4. Abiotic stability

The abiotic stability of electrochemically deposited and spin-coated PEDOT:PSS films was determined utilizing an accelerated ageing test, which was designed based on the ISO for the biological evaluation of medical devices [184]. The neural probes were subjected to 70 °C for 168 h, which is the recommended condition for implants with an intended use of less than 30 days. The electrochemical properties were determined using EIS and CV after 48 h and 168 h, and the PEDOT:PSS coatings were imaged at the end of the study. As the lowest and most stable impedance for spin-coated films was observed for a thickness of 610 nm (see Figure 5.8), this thickness was used for the ageing study. Ideally, for a comparison of the two
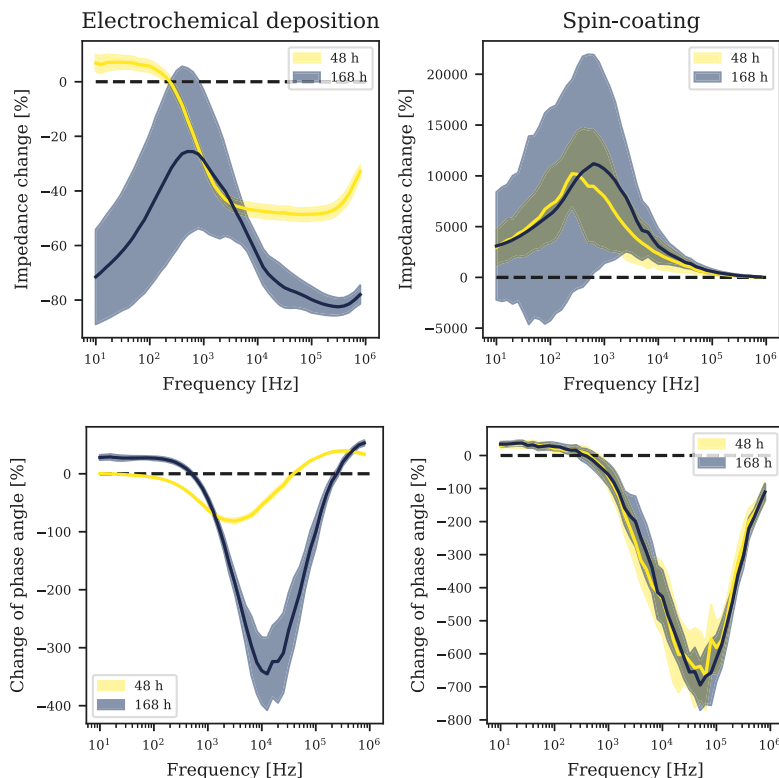
Figure 5.11.: Normalized changes of impedance (top) and phase angle (bottom) for electrochemically deposited (left) and spin-coated (right) PEDOT:PSS induced by accelerated ageing for a test period of 168 h at 70 °C. Median±95 % CI are depicted with n = 24, 18, 17 and 17 for electrochemical deposition - 48 h, electrochemical deposition - 168 h, spin-coating - 48 h and spin-coating - 168 h, respectively. Representative bode plots of the PEDOT:PSS film before accelerated ageing are given in Figure 5.7.

methods, similar properties such as impedance should be considered. However, the impedances differed significantly when comparing electrochemical deposition and spin-coating. Therefore, similar CSCs were favoured (see Figure 5.10). To compare both coating methods, 360 nm thick electrochemically deposited PEDOT:PSS was considered. For both methods, the ageing test was performed with two different neural probes each consisting of 16 electrodes. Microelectrodes with an impedance above $10\,\text{M}\Omega\cdot\mu\text{m}^2$ at 1 kHz were excluded as outliers.

The normalized impedance changes in response to the accelerated ageing are shown in Figure 5.11. An interesting trend seen for both types of PEDOT:PSS coatings was that around 10^3 Hz a transition in impedance changes was observed. Above this

cut-off frequency, the impedance of native PEDOT:PSS changed from a capacitive into a resistive behaviour (see Figure 5.7). Therefore, the changes due to ageing are still dominated by the double layer capacitance and the solution resistance at low and high frequencies, respectively. For the test period of 48 h, the electrochemically deposited films exhibited a reduction in electrode impedance with a maximum of 49 % [46-51 %], median [95 % CI] (n=24) at high frequencies. For frequencies below 10^4 Hz corresponding to APs and LFPs, the impedances were affected less than 45 %. After 168 h, the reduction was higher compared to the shorter test period. The decrease within the mid frequency range was similar to the behaviour after 48 h whereas at low and high frequencies, a decrease down to 80 % was observed. Multiple factors can cause an increase in conductivity such as delamination of insulation layers exposing more of the underlying metal film [18, 185] or swelling of the PEDOT:PSS coating [186, 187]. Substantial degradation of insulation layers results in decreased impedances over the entire frequency range as larger conductive areas are exposed to the electrolyte. Slight defects in PaC passivation layers were identified as reduced impedances at 10^5 Hz by R. Caldwell, *et al.* [185]. With increasing degradation, they observed an additional reduction in impedance for low frequencies. These findings are consistent with the impedance changes seen within this work indicating that a delamination of PaC due to ageing induced the reduction in conductivity. This degradation mechanism was not detected for spin-coated PEDOT:PSS. Commonly, silane is used to enhance adhesion between PaC films. However, within the microfabrication of the probes used for the electrochemical deposition of PEDOT:PSS, silane was not used during the CVD of the PaC passivation layer in contrast to probes utilized for spin-coating (see Section 4.4.1). The reason for this difference is that the process with silane was established at a later time. Optical evaluation did not reveal any delamination of PaC. Rather, a degradation of PEDOT:PSS was observed in the form of delamination and colorimetric changes (see Figure 5.13 a-b), which should result in a decreased conductivity. However, it could be possible that the increased conductivity due to delamination of PaC overshadowed the degradation of PEDOT:PSS resulting in an overall decreased impedance response.

Compared to electrochemical deposition, the spin-coated films exhibited a less robust behaviour in form of increased impedances. Especially, frequencies below 10^4 Hz were affected by the rise with a maximum of roughly 10^4 % for both test periods. As described by G. Dijk, *et al.* [188], electrical connection issues can result in higher impedances mainly when using ZIF connectors to interface flexible probes as the force needed to close the connector can easily cause damages. Within this work, the probes were soldered to a PCB. Additionally, the impedance was in the range of the impedance of bare Pt microelectrodes indicating the delamination of PEDOT:PSS caused the increase in impedance. Due to these defects, the double layer capacitance of the underlying Pt dominates the electrode-electrolyte interface. This is further manifested as a decrease in the phase angle, especially at high frequencies. The impedance at high frequencies changes from a resistive
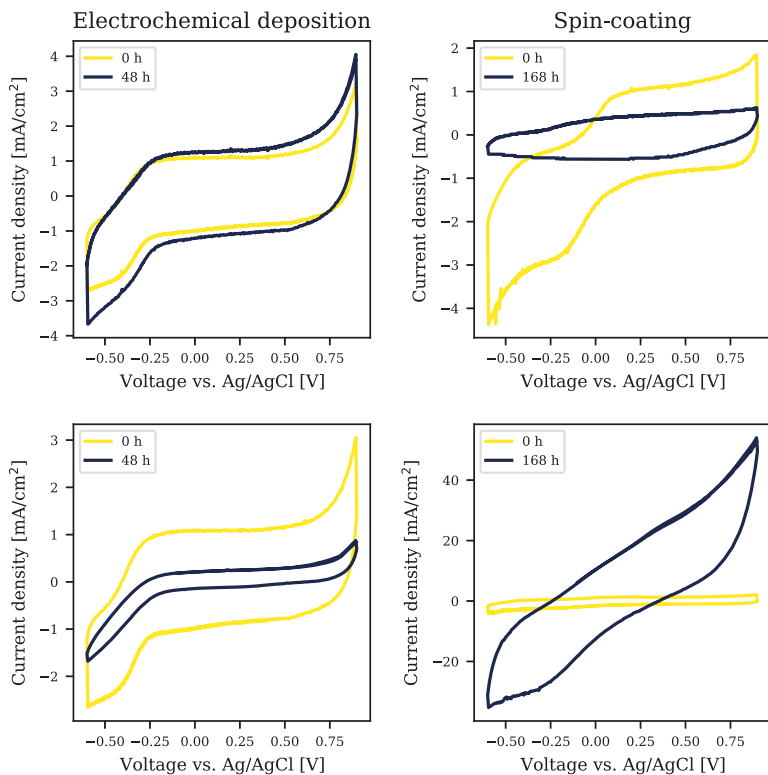
Figure 5.12.: Representative changes in current over voltage curves in response to accelerated ageing of electrochemically deposited (left) spin-coated (right) PEDOT:PSS.

to a more capacitive conductivity as it was observed for bare Pt microelectrodes with a capacitance dominated mode for the entire frequency range (see Figure 5.6 and Figure 5.7). High impedance electrodes act like a high-pass filter, meaning low frequency contents within the input signals such as LFPs and slow APs are attenuated. The optical images did not reveal any substantial delamination. As the probes were imaged under dry conditions, it is possible that the detached areas laid down flat. Some of the electrodes exhibited a darker blue colour in response to the ageing (see Figure 5.13 e-f).

For electrochemical deposition, some of the characterized electrodes were analysed utilizing 5 CV cycles after 48 h and 168 h. However, the performance varied from probe to probe as shown in Figure 5.12. For the first sample, an increase in CSC (20 % [−11-+51 %], median [95 % CI] (n=4)) was observed after the 48 h storage time whereas the second probe exhibited a decrease (81 % [75-87] %, median [95 % CI] (n=6)). Furthermore, impedance measurements after the CV scans revealed

that the impedances drastically increased for the second samples in contrast to the first probe. These differences in the electrochemical performance might originate from quality variations among probes. To minimize batch-to-batch variations, neural implants produced within one fabrication run were considered for the ageing test. However, besides the fabrication, probes undergo additional processes such as packaging and electrochemical and optical characterization, which might induce handling damage and affect the performance. After the test period of 168 h, unstable current responses were observed for most of the electrodes from both samples. Therefore, the CSC was not determined. Decreased CSCs and increased impedances as seen for the second sample after the 48 h test period originate from the underlying Pt film after delamination of the PEDOT:PSS coating, which is consistent with the optical validation (see Figure 5.13 d). An increase in CSC can have multiple causes. Similar to the corresponding impedance changes, it is assumed that degradation of the PaC passivation layer induced the increase in CSCs. The optical inspections confirmed this as for a few electrodes, a bubbling of PaC was observed at the interface to PEDOT:PSS (see Figure 5.13 c).

Due to the bad performance when considering the electrode impedance, spin-coated PEDOT:PSS was characterized in regard to CSC only after the entire storage time of 168 h. In contrast to electrochemical deposition, a stable change was observed with a reduction in CSC of 66 % [11-121 %], median [95 % CI] (n=5). The decrease could result from delaminating PEDOT:PSS, which is consistent with the impedance changes. However, the degradation was pronounced for the impedance in contrast to CSC. Two out of 7 electrodes exhibited a drastic increase in CSC (see Figure 5.12). However, their impedances were comparable to the remaining electrodes. Swelling of spin-coated PEDOT:PSS might induce an increase in CSC as observed within previous works however, this would additionally result in a decreased impedance [186–188].

The accelerated ageing factor (AAF) based on the study parameters used within this work is roughly 10, calculated by applying the Arrhenius equation (see Equation 5.2). This results in a simulated time of 70 days (=1680 h) at 37 °C, which is roughly twice the intended use proposed by the ISO for the biological evaluation of medical devices (<30 days) [184]. Ignoring the PaC delamination issues observed for the probes with electrochemically deposited PEDOT:PSS, this electrode coating seems to withstand the ageing for at least 20 days at 37 °C (equal to 48 h at 70 °C). For longer test periods, the impact of degrading insulation layers was too high to draw any conclusion about the coating stability. Within previous works, a stable performance was observed for roughly 8 days at 60 °C, with an increase in impedance of 100 % due to coating delamination [189, 190]. Therefore, it is assumed that the electrochemically deposited PEDOT:PSS can withstand longer test periods.

For spin-coating, delamination of PEDOT:PSS resulted in a poor long-term stability already for the shorter test period of 48 h. In contrast to electrochemical deposition, spin-coated films have not yet been characterized in regard to abiotic stability. An
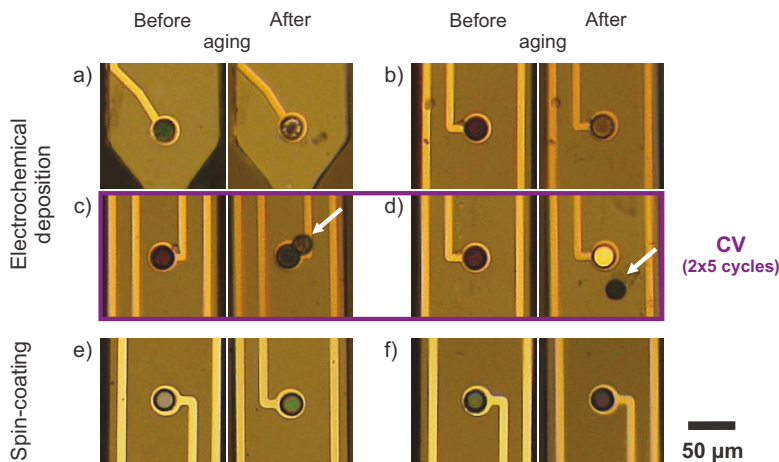
Figure 5.13.: Failure mechanisms of PEDOT:PSS coatings induced by accelerated ageing for a total test period of 168 h at 70 °C. For electrochemically deposited PEDOT:PSS, partial delamination (a) and colorimetric changes (b) were observed. In response to CV cycling (2 x 5 cycles), bubble formations underneath the PaC passivation layer (c) and complete delamination (d) were additionally seen. For spin-coating, no substantial changes besides a slightly darker colouring of the coating were detected (e-f).

exception is a recent work where the long-term stability of spin-coated PEDOT:PSS was characterized over a test period of four months at 37 °C in cell culture medium [188]. Within this study, 5 out of 10 characterized electrodes exhibited a stable low impedance. Furthermore, 80 % of the electrodes showed no visible substantial degradation except for a few electrodes, with colorimetric changes or partial delamination of PEDOT:PSS. As the microfabrication and the PEDOT:PSS formulation were comparable, it is unclear why the spin-coated PEDOT:PSS underperformed within this work compared to G. Dijk, *et al.*'s work [188].

5.3.5. Electrochemical stability

The stability of polymer coatings obtained via electrochemical deposition and spin-coating was studied by applying repetitive electrochemical stress in form of charge-discharge cycles. PEDOT:PSS films were exposed to several hundreds of CV cycles. In between, optical images and EIS were taken to characterize the changes and failure modes within the electrode coatings. Additionally, samples were imaged with SEM after the final stability test. The lowest and most stable impedance for spin-coated films was observed for a thickness of 610 nm (see Figure 5.8). To compare both coating methods, 360 nm thick electrochemically deposited PEDOT:PSS was considered as it exhibited similar CSCs like 610 nm thick spin-coated films (see
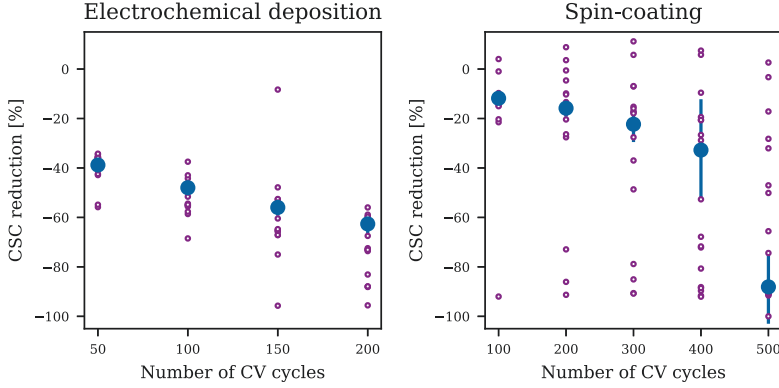
Figure 5.14.: Charge storage capacity (CSC) reduction in response to CV charge-discharge cycles for electrochemically deposited (left) and spin-coated (right) PEDOT:PSS. Besides the reduction for each characterized microelectrode (purple circles), the median±95 % CI (n=24 for electrochemical deposition and n=21 for spin-coating) is displayed (blue dots and bars).

Figure 5.10). For both methods, the stability test was performed with 21-24 functional electrodes from three different neural probes defined as those with an impedance below $10\,M\Omega\cdot\mu m^2$ at $1\,kHz$.

Figure 5.14 shows the reduction in CSC of PEDOT:PSS films for progressive CV cycles. As considerable variations were seen in the performance of spin-coated PEDOT:PSS, besides the median and 95 % CI, the reduction for each electrode is displayed. After 100 charge-discharge cycles, a reduction of 48 % [46-50] %, median [95 % CI] (n=24) and 12 % [11-13 %], median [95 % CI] (n=21) was observed for electrochemical deposition and spin-coating, respectively. Therefore, a faster decay was observed for electrochemical deposition. However, the increase in impedance at $1\,kHz$ was higher for spin-coating (see Figure 5.15). For electrochemical deposition, the rise in impedance was observed over the entire frequency range whereas for spin-coated films, no changes were seen at low frequencies ($10\text{-}10^2\,Hz$) for the first 200 cycles. Furthermore, for spin-coating, the electrode impedance was more sensitive to the degradation upon applying electrochemical stress in contrast to the CSC. 14 out of 21 electrodes with spin-coated PEDOT:PSS exhibited a stable CSC with a reduction of less than 25 % up to 300 CV cycles (see Figure 5.14) but impedance increased by around one order of magnitude at $1\,kHz$ (see Figure 5.15). After 400-500 CV cycles, a behaviour similar to bare Pt microelectrodes was observed (see Figure 5.15 and Figure 5.6).

For electrochemical deposition, the film changed the colour from dark blue over light blue to purple for increasing CV cycles (see Figure 5.16 a). Furthermore, pieces of PEDOT:PSS delaminated exposing the underlying Pt layer, which was optically evident after 150 CV cycles (see Figure 5.16 a). Contrarily, the spin-
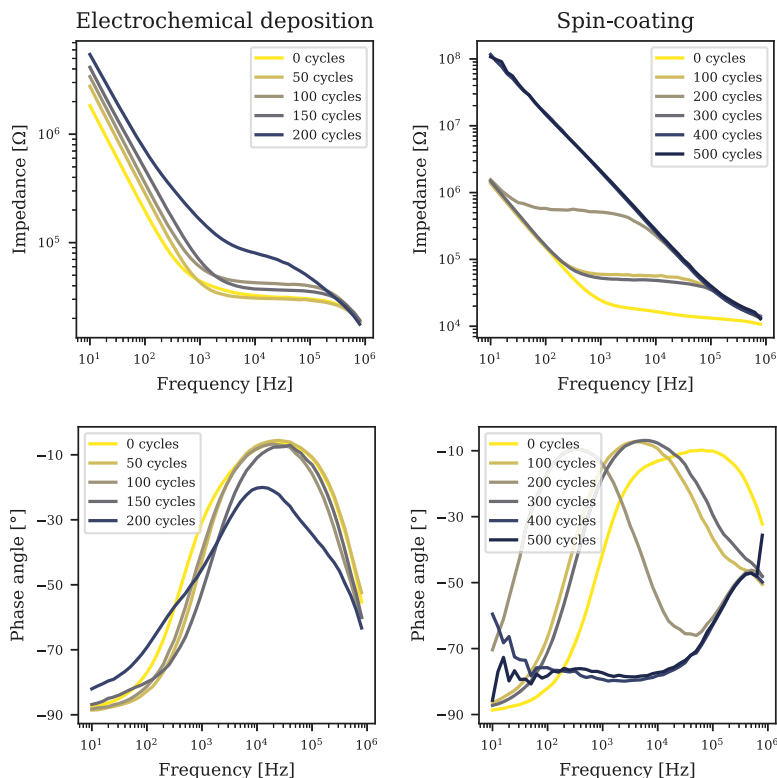
Figure 5.15.: Representative impedance and phase angle changes for increasing CV cycles of 360 nm electrochemically deposited (left) and 610 nm spin-coated (right) PEDOT:PSS.

coated films failed due to wrinkling and delamination from electrode sidewalls (see Figure 5.16 c). Repetitive charge-discharge cycles trigger the exchange of ions between electrolyte and intrinsically conducting polymers such as PEDOT:PSS causing a volumetric change of the film [143, 189]. The resulting mechanical stress can cause a degradation of the electrode coating in the form of cracking and delamination as observed for spin-coated films (see Figure 5.16 c), consistent with findings from G. Dijk, *et al.* [183]. Furthermore, deterioration in the form of over-oxidation can be the reason for failure. Such degradation was observed near the polymerization potential of EDOT [191], for example, when the anodic potential limit within a CV scan exceeded 0.8 V (vs. SCE) [192, 193]. Above this potential, the CV is dominated by an oxidation peak without a corresponding reduction peak indicating irreversible changes within the polymer film. Over-oxidized PEDOT:PSS has a micro-cracked morphology with islands of polymer spread over the underlying metal layer [192]. Additionally, changes in the typical blue colour of PEDOT:PSS

67
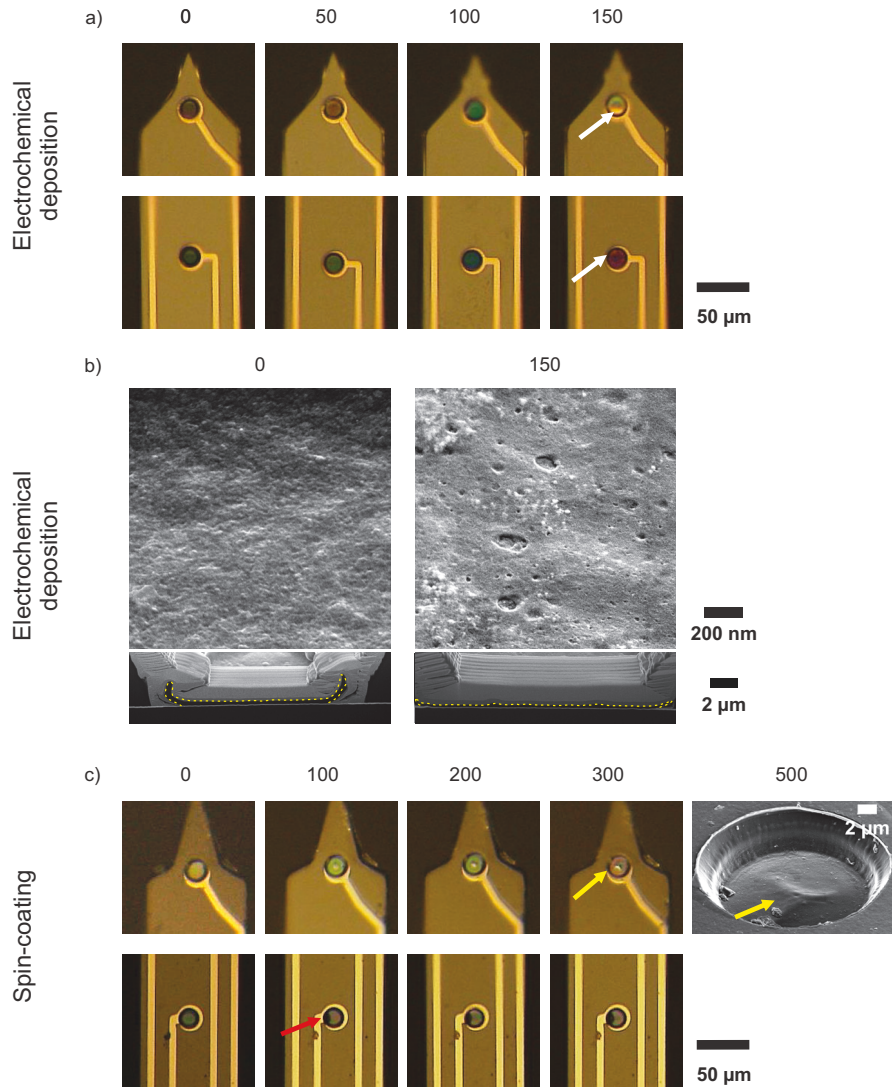
Figure 5.16.: Failure mechanisms of PEDOT:PSS. Degradation of electrochemically deposited PEDOT:PSS (a) in form of colorimetric changes and delamination (white arrows). The colorimetric changes resulted from thickness reductions accompanied by morphological changes from a globular to a large-pored surface (b). The PEDOT:PSS coatings are boarded in yellow. Spin-coated PEDOT:PSS (c) degraded due to wrinkling (yellow arrows) and delamination (red arrow). The number of CV cycles equivalent to the applied electrochemical stress are displayed on top of the images.

in response to electrochemical stress can indicate deterioration [140, 189]. As within this work, the polymer coatings were exposed to potentials below +0.9 V (vs. Ag/AgCl), an over-oxidation can be excluded. The colorimetric modification, that the electrochemically deposited polymer underwent during the CV cycling, could rather be a reduction in coating thickness. For increasing polymer thicknesses equivalent to higher deposition charges, a change from light to dark blue was seen (see Figure A.5), which was comparable to the observations from the CV cycling (see Figure 5.16). Additionally, FIB sections reveal a thickness reduction when comparing treated with un-treated films correlated with changes of the morphology from a globular to a large-pored surface (see Figure 5.16 b). The poor adhesion of electrochemically deposited PEDOT:PSS on Pt/Au has been demonstrated within several works where cracking and delamination resulted in a reduction in CSC and an increase in impedance [176, 194]. This is comparable to the findings within this work. To the best of our knowledge, the electrochemical stability of spin-coated films was characterized for the first time within this work.

To summarize, the different coating morphologies obtained for electrochemical deposition and spin-coating (see 5.3.2) exhibited different failure mechanisms upon electrochemical stress. Spin-coating mainly failed due to optically evident delamination of the films. Furthermore, a slight reduction in CSC for the first 300 cycles was observed as the conductive polymer was still partially in contact with the underlying metal (see Figure 5.16). However, the change in impedance was more pronounced. As the underlying Pt was exposed to the electrolyte, its double layer capacitance dominated the interface with an increase in impedance and a decrease in the phase angle at high frequencies (see Figure 5.15). Contrary, electrochemically deposited films degraded by thickness reduction and delaminated pieces with a consistent change in CSC and impedance.

To improve the poor adhesion between PEDOT:PSS and the underlying metal substrate, different approaches have been studied. On the one hand, the surface roughness of the metal was increased to enhance physical interactions [189, 195, 196] and on the other hand, chemical adhesion promoters were considered [189]. It is, for example, assumed that carbide bonds between IrOx and PEDOT:PSS improve the chronic adhesion of the conductive polymer [189]. Due to the superior electrochemical stability of PEDOT:PSS by introducing IrOx as an adhesion layer demonstrated by C. Boehler, *et al.* [189], a similar approach was tested to improve the adhesion between PEDOT:PSS and Pt within this work. As described in Section 5.2.3, the Pt microelectrodes were covered with a 450 nm thick sputtered IrOx film (SIROF) during the microfabrication of the neural probes before spin-coating or electrochemically depositing PEDOT:PSS. The IrOx films sputtered at 200 W and 10 sccm O_2 had a cauliflower-like morphology [135, 197, 198] (see Figure 5.17 b) and exhibited a RMS roughness of 68.68±28.91 nm (mean±std, n=3) compared to bare Pt with 21.63±11.78 nm (mean±std, n=2). Unfortunately, it was not possible to obtain a dendritic morphology similar to C. Boehler, *et al.* [189] with a roughness of 177±18 nm (measured as feature height). IrOx sputtered at similar
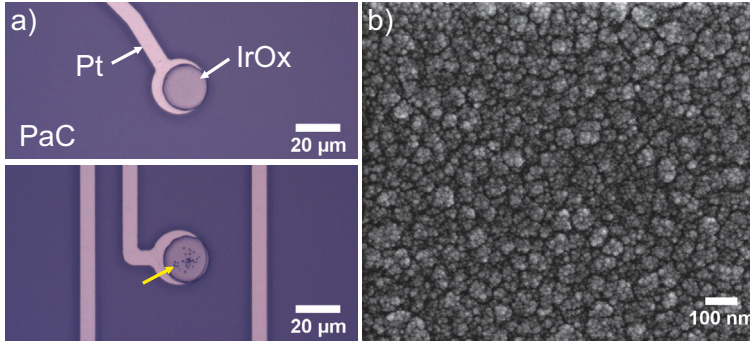
Figure 5.17.: Sputtered IrOx film (SIROF) as adhesion promoter for PEDOT:PSS. IrOx coating onto Pt electrodes for the fabrication of flexible neural probes (a). Bigger particles of IrOx were occasionally observed at the centre of the coating (yellow arrow). SEM image of SIROF employing 200 W and 10 sccm O_2 (b).

parameters (100 W and 15 sccm O_2) still exhibited a cauliflower-like morphology. Therefore, the parameters resulting in a higher surface roughness were used for further experiments.

The impedance at 1 kHz for spin-coated PEDOT:PSS with SIROF as adhesion layer was 5.351 [4.599-6.102] MΩ·µm^2, median [95 % CI] (n=7) (see Figure 5.18), which was higher than PEDOT:PSS spin-coated on bare Pt electrodes (see Figure 5.8, 610 nm). This difference might indicate that the electrochemical properties are not only defined by the conductive polymer, which should ideally be the case but, is rather additionally affected by the underlying metal films. To determine the charge storage performance, the PEDOT:PSS films were exposed to 10 CV cycles resulting in a CSC of 23.077 [18.326-27.827] mC/cm^2, median [95 % CI] (n=7) (see Figure 5.18). The CSC was lower compared to PEDOT:PSS spin-coated on bare Pt electrodes (see Figure 5.10, 610 nm). Furthermore, for the potentials below -0.2 V noisy artefacts were observed and the impedance after the potential cycling increased drastically to 52.816 [39.864-65.769] MΩ·µm^2, median [95 % CI] (n=7) indicating a deterioration of the conductive polymer.

As for the bare Pt microelectrodes, faradaic charge transfer processes were identified for potentials below -0.2 V (see Figure 5.6), it was assumed that these reactions might induce a degradation of the IrOx/PEDOT:PSS stack during CV cycling. To verify this, flexible probes with bare SIROFs, which were released before spin-coating PEDOT:PSS, were characterized in regard to impedance and CSC. Figure A.10 in the Appendix depicts the bode plot with 222.293 [183.627-260.960] MΩ·µm^2, median [95 % CI] (n=4) at 1 kHz and the CV scan of SIROF with a CSC of 7.446 [6.353-8.539] mC/cm^2, median [95 % CI] (n=4). Furthermore, the activation of IrOx known as film hydration [198] was done by applying 100 CV cycles (-0.6 V to +0.9 V (vs. Ag/AgCl), 0.1 V/s, in 0.1 M PBS). As shown in previous works [135, 198, 199], the activation increases the CSC and decreases the impedance of

IrOx due to reversible redox processes (see Figure A.10). As SIROFs exhibited expected electrochemical behaviour, it was assumed that the combination of Pt and SIROFs did not induce any deterioration.

In the next step, the influence of activated SIROF on the performance of PEDOT:PSS was determined. Spin-coating results in ready-to-use probes at the end of the MEMS fabrication before packaging. Therefore, electrochemical deposition was considered as it offers the possibility to try different pretreatments within one probe before the deposition of PEDOT:PSS. Some electrodes of an A-MEA-16 probe with SIROF were activated before the electrochemical deposition of PEODT:PSS, whereas others remained untreated. After the deposition of PEDOT:PSS, the samples were first exposed to 10 and then to 100 CV cycles and the impedance was measured in between. The deposition charges and the impedances of the electrochemically deposited PEDOT:PSS were similar for native and activated SIROFs (see Table 5.1). However the deposition charges were slightly higher compared to bare Pt (see Table A.1) whereas the electrode impedance was lower (see Figure 5.8). Furthermore, the CSC and the impedance after exposing the PEDOT:PSS to 10 CV cycles were higher for activated SIROFs compared to un-treated SIROFs. The activation process of SIROFs results in an increased film microporosity [135, 198] and therefore, improved electrochemical properties (see Figure A.10). In comparison to PEDOT:PSS, the SIROF exhibits higher CSCs and impedances after activation. Thus, the increased parameters of PEDOT:PSS on SIROF upon CV cycling might be an indication that besides PEDOT:PSS, IrOx affects the electrochemical interface. Representative bode plots and CV scans are provided in the Appendix (see Figure A.11). The progressive degradation
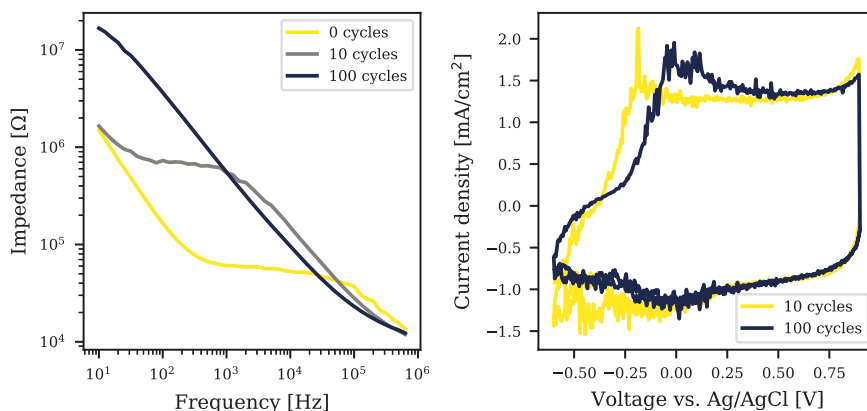

Figure 5.18.: Bode plots (left) and current over voltage curves (right) of spin-coated PEDOT:PSS on top of a SIROF adhesion layer. During the CV scan, deteriorations in the form of noisy artefacts were observed below -0.2 V (vs. Ag/AgCl), resulting in an increased impedance.

| PEDOT:PSS | Sputtered iridium oxide film (SIROF) | | Activated SIROF |
	Spin-coating	Electrochemical deposition	
Deposition charge [mC/cm^2]		188.775 (175.935-201.616)	208.228 (200.246-216.210)
Impedance [M$\Omega\cdot\mu$m^2]	5.351 (4.599-6.102)	3.534 (3.321-3.747)	3.602 (3.316-3.888)
CSC [mC/cm^2]	23.077 (18.326-27.827)	45.005 (41.847-48.164)	95.051 (82.956-107.145)
Impedance - Post 10 CV [M$\Omega\cdot\mu$m^2]	52.816 (39.864-65.769)	3.755 (3.424-4.086)	27.143 (17.448-36.838)
CSC - Post 100 CV [mC/cm^2]	26.791 (22.830-30.752)	29.355 (19.013-39.697)	74.361 (67.437-81.284)
Impedance - Post 100 CV [M$\Omega\cdot\mu$m^2]	58.019 (48.455-67.582)	58.302 (50.400-66.203)	35.060 (28.956-41.164)

Table 5.1.: Properties of PEDOT:PSS on native and activated SIROFs (median (95 % CI), n=7 for spin-coating, n=4 for electrochemical deposition). The charges were obtained for a deposition time of 15 s at 1 V (vs. Ag/AgCl). Impedance values at 1 kHz are given.

in response to potential cycling was observed for both PEDOT:PSS methods in combination with native or activated SIROF, especially when considering CSC and impedance after 100 CV cycles. This is a further indication that the structural changes within the IrOx films during CV cycling induce the degradation.

During cycling, IrOx undergoes reversible faradaic reactions between Ir^{3+} and Ir^{4+} valence states within the oxide film resulting in slightly pronounced redox peaks at 0.25, 0.5 and -0.2 V (vs. Ag/AgCl) within the CV scan [197, 200] (see Appendix, Figure A.10). Some of these peaks were observed for PEDOT:PSS deposited on top of SIROF after applying 100 CV cycles. The CV scans of spin-coated and electrochemically deposited PEDOT:PSS on top of native SIROF exhibited a peak at 0.0-0.1 V (vs. Ag/AgCl) whereas electrochemical deposition after activating SIROF resulted in a broad peak at -0.2 V (vs. Ag/AgCl) (see Figure 5.18 and Figure A.11). Additionally, the loss of conductivity was similar for electrochemical deposition (without activating IrOx) and spin-coating (see Table 5.1). Within C. Boehler, *et al.*'s work [189], such degradations were only observed for activated SIROFs however, not for un-treated SIROFs. As reported within this study, a possible reason for the deterioration could be that IrOx facilitates an over-oxidation of PEDOT:PSS as it has been used as oxidizing agent for the polymerization of hybrid nanocomposites such as PEDOT-IrOx [201]. More work is needed to fully understand the interactions between IrOx and PEDOT:PSS in response to potential cycling.

5.4. Conclusion

PEDOT:PSS has been introduced as electrode coating material to overcome low SNR recordings and high charge injection limits of high impedance electrodes.

Such coatings can be obtained by either electrochemical polymerization [140] or by utilizing chemically polymerized PEDOT:PSS as ready-to-use mixtures [157, 158]. The deposition method has a great impact on the electrochemical properties and the robustness of the resulting PEDOT:PSS films. Seeking a good conductivity, stable electrochemical performance, and fast fabrication process, electrochemically deposited PEDOT:PSS obtained under potentiostatic condition was compared to spin-coated PEDOT:PSS crosslinked with EG, GOPS and DBSA.

Considering the microfabrication, spin-coating needs additional steps to establish the polymer films. However, it is a high through-put method resulting in ready-to-use probes. This wafer-scale approach results in higher variations in electrochemical performance in contrast to electrochemical deposition where probes are coated individually enabling precise control of the polymer growth. The chemical nature of electrochemical polymerization confines the deposition to a certain charge range to not overgrow the microelectrode. Contrary, stacking of spin-coated films offers the possibility to produce thicker coatings with even higher conductivity than shown within this work. Furthermore, the impedances of comparable film thicknesses were significantly lower for spin-coating compared to electrochemical deposition whereas no significant difference was observed with respect to CSCs when comparing both coating methods. As even thinner electrochemically deposited films exhibited similar CSCs as thicker spin-coated films, it is assumed that barriers between the stacked layers were formed reducing the ion diffusion for spin-coated films. To verify the reduced conductivity, layers with comparable thicknesses should be produced by tuning the spin speed and by stacking of several layers. The characterization of these films should reveal if there is a difference in CSC upon stacking of several PEDOT:PSS layers. It is worth mentioning, that CSCs determined by slow CV cycling overestimate the charge available during sub-millisecond stimulation pulses [8, 175]. Therefore, besides CSC, CIC should be determined. However, this is only meaningful when parameters specific for a given application are used. As the aim of this work was to produce flexible intracortical implants for long-term recording purposes, the characterization of CSC was sufficient.

As a future chronic implantation was intended for the intracortical implants developed within this work, the abiotic stability of the PEDOT:PSS films and the entire PaC based probes was characterized utilizing accelerated ageing. Based on the preliminary results presented here and previous works, electrochemical deposition seems to be stable for an implantation period of at least 20 days. Therefore, this deposition method is more robust than spin-coating. Additionally, the electrochemical stability of the PEDOT:PSS films was characterized by applying repetitive charge-discharge cycles. Both methods exhibited a poor stability. Interestingly, the observed failure modes were mainly dictated by the different coating morphologies. Electrochemically deposited PEDOT:PSS degraded due to thickness reduction and delaminated pieces whereas spin-coated films failed due to delamination and wrinkling. To improve long-term stability, SIROF was studied as an adhesion layer. However, in contrast to previous works with promising robustness, degradation

	Electrochemical deposition	Spin-coating
High through-put fabrication	-	+
Impedance	-	+
CSC	+	-
Abiotic stability	(+)	-
CV stability	-	-

Table 5.2.: Summary of the comparative study considering electrochemical deposited and spin-coated PEDOT:PSS films. +/- indicates better/worse performance when comparing the two different deposition methods. The impedance and CSC were marked with regard to coating thickness.

mechanisms in response to potential cycling were observed when using SIROF in combination with PEDOT:PSS. A summary of the comparative benchmarking study considering electrochemical deposited and spin-coated PEDOT:PSS films is given in Table 5.2.

Despite the superior electrochemical performance in contrast to bare Pt microelectrodes, the long-term stability of PEDOT:PSS was poor, even though conservative study parameters were used. For accelerated ageing studies, the addition of reactive species has been proposed to mimic the oxidative stress induced by the foreign body response [18, 185]. Furthermore, as mentioned above, the CIC is a better estimate for the charge available during stimulation. Therefore, this parameter should be used to validate how many pulses the electrode coating would survive after the characterization with slow potential cycling using CV. To summarize, much more effort is needed to produce low impedance electrodes utilizing conductive polymers such as PEDOT:PSS with superior biocompatibility, conductivity, and stability suitable for chronic implantation.

6. Shuttle system for implantation of flexible probes

Traditional intracortical probes based on Si enhance acute immune reactions and reduce the long-term stability of high-quality recordings. To minimize the mechanical mismatch between device and neural tissue and thereby the foreign body reaction, compliant probes have been investigated (see Chapter 2). However, such devices are unable to penetrate the brain without buckling. Therefore, a straight insertion into the target region is not feasible without a shuttle system. Several insertion aids have been proposed to temporarily or partially stiffen the flexible device during insertion. Stiff shuttles such as silicon shanks or rods have been proposed to mechanically reinforce the probe, which are retracted after implantation [22, 202, 203]. Aligning the neural probe to a rigid support and ensuring good adhesion during the entire implantation process can be challenging. The integration of such stiff shuttles to arrays of probes is difficult and therefore, such insertion aids are mainly introduced for single shanked devices. Furthermore, positioning the flexible device might be imprecise due to probe displacement while separating the stiffener from the implant [22]. Introducing a rigid insertion system and especially the additional mechanical stress the tissue experiences during retraction can be counterproductive for reducing the acute damage and might hamper the long-term device performance. A new approach introduced in the last couple of years was using mechanically adaptive polymers as substrate material for neural implants [204–206]. Upon a certain stimulus such as humidity, the Young's modulus drops by roughly one order of magnitude from tens of MPa to a few MPa. Therefore, devices based on such smart polymers are able to penetrate the tissue during insertion while reducing the stress at device/tissue interface. The preparation and micromachining of such polymers needs to be further optimized to produce implants with a small footprint, comparable to probes based on PaC and polyimide. Intracortical devices with cross-sectional areas of $10,000\,\mu m^2$ [206] and $20,300\,\mu m^2$ [204] were produced using mechanically adaptive polymers whereas PaC probes with footprints down to $3,000\,\mu m^2$ [45] or $1,000\,\mu m^2$ (see Chapter 4) could be realized. Furthermore, the swelling of such polymers under physiological conditions can lead to mechanical or electrical failure of the devices and harm neighbouring cells or blood vessels [7, 204, 206]. Biodegradable polymer coatings are more commonly employed to temporarily support flexible probes [130, 207, 208]. These polymers are resorbed upon contact with physiological fluids and therefore no shuttle removal is needed

nor structural change of the probe itself needs to be feared. However, the chronic impact of the different shuttle systems on neural tissue is yet to be studied in more detail.

A main drawback of most insertion systems is that they are dramatically increasing the implantation footprint thus enhancing the acute tissue damage. Furthermore, the integration of these shuttles into the fabrication process is time consuming as the mechanical reinforcement is performed manually for single probes, resulting in quality variations and a small yield. Within this work, a tissue-friendly shuttle system based on the biodegradable polymer polyethylene glycol (PEG) is introduced, having the potential to overcome the limitations mentioned above.

This chapter was in part reproduced from the following publication:

K. Srikantharajah, R. Medinaceli Quintela, B. M. Kampa, S. Musall, M. Rothermel, and A. Offenhäusser, **Minimally-invasive insertion strategy and in vivo evaluation of multi-shank flexible intracortical probes**, *Scientific Reports*, vol. 11, 2021.

6.1. Insertion mechanisms

For a successful positioning of the implant a straight insertion into the brain is necessary. This can be accomplished when the buckling force threshold of a device is higher than the minimum force required to penetrate the brain tissue defined as insertion force. During implantation, the device experiences a variety of forces, namely axial tip force, frictional force, and compressive clamping force [4]. The insertion force depends on different characteristics such as insertion localization, depth and speed, presence of dura and pia, and on probe material properties and dimensions. In the literature, forces between 0.5-50 mN are found [107, 209–211]. The dura mater is usually removed, allowing an easier implantation of flexible devices. As rigid probes experienced forces between 0.5-1.0 mN during insertion after dura removal, it is assumed that an individual, tapered, compliant probe should withstand a minimum insertion force of 1.0 mN for a successful implantation [209, 211]. The threshold for buckling of compliant probes can be determined by Euler's formula (see Equation 4.1). As stated in Chapter 4.2, implants compliant enough to reduce the foreign body reaction are not able to penetrate the brain due to the low buckling force threshold and therefore, need to be mechanically reinforced during insertion.

6.2. Biodegradable polymers

Different natural (*e.g.* polysaccharides [46], gelatin [109]) and synthetic (*e.g.* PEG [23, 212], poly(vinyl alcohol) (PVA) [130], silk [23]) biodegradable polymers (BPs)
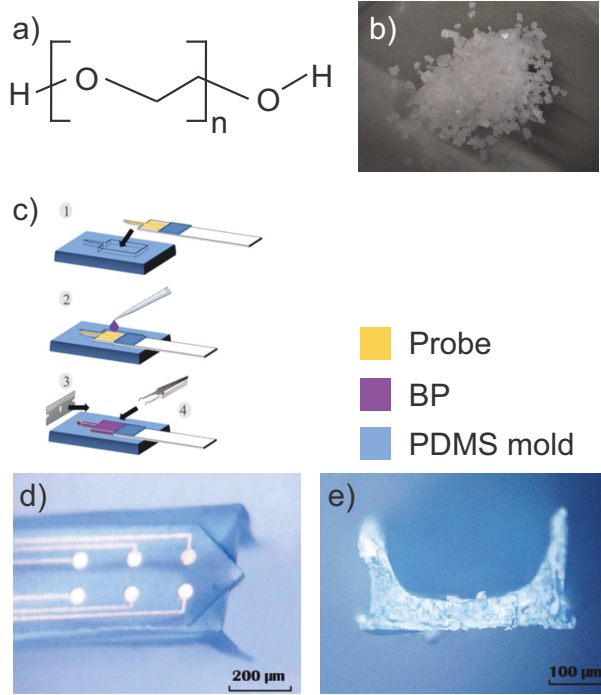
Figure 6.1.: a) Chemical structure of polyethylene glycol (PEG). b) Synthetic PEG granulate (35,000 g/mol). c) Exemplary micro-molding approach utilizing a PDMS mold. Step 1: Alignment of probe into mold. Step 2: Deposition of biodegradable polymer (BP). Step 3: Doctor blading of BP to fill the mold. Step 4: Release of probe coated with BP. Figure from [130]. Top (d) and axial (e) view of PEG coated flexible device. Figure from [23].

have been explored as temporary insertion aids to successfully implant compliant intracortical probes. When designing a shuttle system, the biocompatibility of BPs has to be considered. The introduction of BPs into the body should not evoke any foreign body reactions, neither from the original polymer nor from the by-products. Furthermore, the by-products should be completely metabolized by the body. The mechanical strength of the coating must be sufficient to increase the buckling force of the implant and therefore, ensure a successful positioning. The time scale of the dissolution should match the functional demand. BP based coatings have been developed with dissolution times from a few seconds [46] up to several weeks [130]. As degradation depends on the one hand on polymer characteristics such as chemical composition, molecular weight, crystallinity, hydrophobicity, and coating dimensions and on the other hand on environmental factors such as temperature, pH, and local enzyme concentration [213, 214], the dissolution rate can be tuned to fit the desired application. To produce BPs meeting applicational

needs, synthetic polymers are favourable in contrast to natural polymers as the flexibility in chemistry facilitates the optimization of chemical, biological, physical, and mechanical properties. Additionally, synthetic polymers are commercially available, increasing the reproducibility of proposed shuttle systems. Therefore, in this work, the synthetic polymer PEG was considered to develop an insertion system.

Two different approaches are commonly considered to coat penetrating probes with BPs: dip-coating and micro-molding. For the latter coating method, molds made out of casted PDMS are used and filled by doctor blading [130] (see Figure 6.1 c), syringe jetting [23], or centrifugation [215]. Limitations of this procedure are on the one hand the difficulty in obtaining uniform coatings without trapped air bubbles and on the other hand the risk of stress-induced bending after releasing probes from the mold. Dip-coating can result in more homogenous coating. However, achieving the desired thicknesses is difficult compared to micro-molding. Utilizing drawing lithography, the BP coating could be optimized by tuning the temperature of the liquid BP and the withdrawal speed during dip coating [46].

As PEG is the BP used in this work to temporarily stiffen flexible intracortical implants an in-depth overview of this polymer is provided. The chemical structure of PEG and an image of the synthetic granulate are depicted in Figure 6.1 a-b. Before being considered as a biodegradable coating for penetrating probes, PEG has been widely used for drug delivery [216, 217], tissue engineering [218], and surface functionalization [219] due to its non-toxic and non-immunogenic properties. PEG is available over a wide range of molecular weights (MW) such as 200-200,000 g/mol [220]. Depending on MW, PEG can range from liquid to low-melting solids, that dissolve when in contact with water. Furthermore, the dissolution time increases with higher MWs [221]. However, the clearance mechanism of PEG and its by-products within the body needs to be further investigated. O. Biondi, *et al.* [222] have shown that very low MW PEG, 200 g/mol, induced chromosome aberrations in Chinese hamster epithelial liver cells whereas PEG 400 g/mol did not show any clastogenic activity. In contrast, high MW PEG can locally accumulate due to slow dissolution and clearance processes [214]. Despite the unknown *in vivo* degradation, several works have successfully developed PEG based shuttle systems for compliant probes. A. Lecomte, *et al.* [23] showed that a 236±14 µm thick coating based on PEG 100,000 g/mol (see Figure 6.1 d-e) with a compression force of 47±16 mN is stiff enough to successfully insert PaC based probes. However, the fast dissolution rate of a few minutes enables only one fast attempt at insertion and no repositioning of the probe. In 2005, a PaC based microfluidic channel integrated in a flexible probe and filled with PEG 2700-3500 g/mol was introduced and could be successfully inserted into the rats' sensory cortex [223]. H. Xu, et al. [45] developed a temporary brace based on PEG 3350 g/mol to reduce the effective length of PaC probes. A stepwise implantation was utilized where the PEG was gradually dissolved at the brain surface and the newly exposed probe length was further inserted. As a similar approach was considered within this work,

the dependency between effective length and buckling force of the probe is further discussed in the following section.

6.3. Development of a tissue-friendly insertion system

A novel shuttle system was established that enabled the successful insertion of compliant probes without increasing the implantation footprint and therefore, minimizing the acute trauma. In the following chapters, the mechanical background relevant for the proposed insertion system is discussed, and the fabrication and coating details are provided.

6.3.1. Reduction of effective length

For a successful positioning of the implant a straight insertion into the brain is necessary. This can be accomplished when the buckling force threshold of a device is higher than the minimum force required to penetrate the brain tissue defined as insertion force. During implantation, the device experiences a variety of forces, namely axial tip force, frictional force, and compressive clamping force [224]. The insertion force depends on different characteristics such as insertion localization, depth and speed, presence of dura and pia, and on probe material

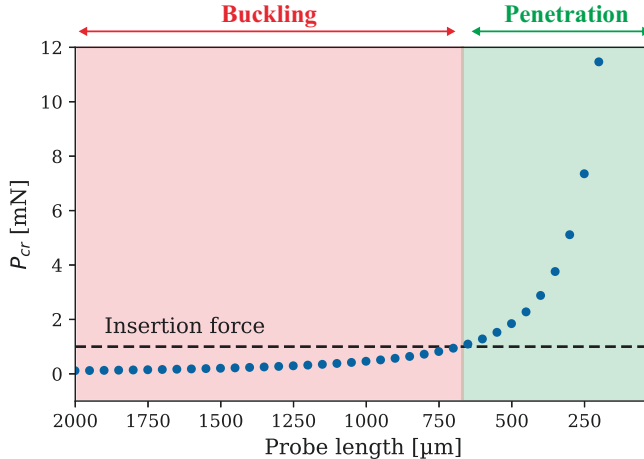**Figure 6.2.:** Buckling force threshold P_{cr} of flexible shanks as a function of probe length. Insertion force of $1\,\text{mN}$ as a reference value that needs to be withstood by the flexible device for a successful penetration of the brain.

properties and dimensions. In the literature, forces between 0.5-50 mN are found [107, 209–211]. The dura mater is usually removed, allowing an easier implantation of flexible devices. As rigid probes experienced forces between 0.5-1.0 mN during insertion after dura removal, it is assumed that an individual, tapered, compliant probe should withstand a minimum insertion force of 1.0 mN for a successful implantation [209, 211]. The threshold for buckling of compliant probes can be determined by Euler's formula (see Equation 4.1). Shank length plays a major role when considering bending and therefore, the mechanical failure of implants, as the buckling force is proportional to $1/L^2$ (see Equation 4.1[1]). Scaling probe length up significantly decreases the threshold for buckling. In contrary, reducing the length raises the threshold and enables insertion.

Considering the PaC based probes proposed in Chapter 4 with a shank length of 2 mm, width of 100 µm, thickness of 10 µm and a Young's modulus of 2.76 GPa, the buckling force threshold exceeds the insertion force of 1 mN when the shank length is shortened to 700 µm (or less) (see Figure 6.2). Based on this fact, an insertion aid was designed to reduce the effective length of the intracortical probes by introducing a temporary PEG coating. During the coating procedure, the shanks were partially covered with PEG, leaving the first 200 µm from the tip exposed (see Chapter 6.3.2). A reduction to 200 µm increases the buckling force threshold hundredfold to 11 mN versus the total shank length of 2 mm, and therefore, would enable a successful insertion without buckling.

6.3.2. Manual coating approach

The insertion system was prepared after the fabrication of the probes (design: A-MEA-16) and soldering them to PCBs (see Chapter 4). A custom made PDMS mold was used for casting PEG on top of the flexible shanks (see Figure 6.3). From a 120 µm PDMS slab, the mold, the base and cover sheet were cut using a blade. After aligning the shanks between the base and the mold layers and, heating up the entire assembly to 80 °C, a granulate of PEG 35,000 g/mol (Sigma-Aldrich, Germany) was molten on top of the mold and carefully distributed over all four shanks. Finally, the biodegradable polymer was solidified at RT and grew the characteristic spherulites (see Figure A.12) and, the cover sheet and the mold were removed. The probe was released leaving the tips (200-300 µm) exposed and the upper part of the flexible shanks covered with PEG. The shanks with the coating on top resulted in a total thickness of roughly 120 µm. If the mold was not gently pressed onto the shank tips it occasionally happened that the molten PEG bleed underneath the mold (see Figure 6.3). As this was only a thin layer it usually dissolved very quickly when approaching the tissue surface. A detailed protocol can be found in the Appendix A.9.

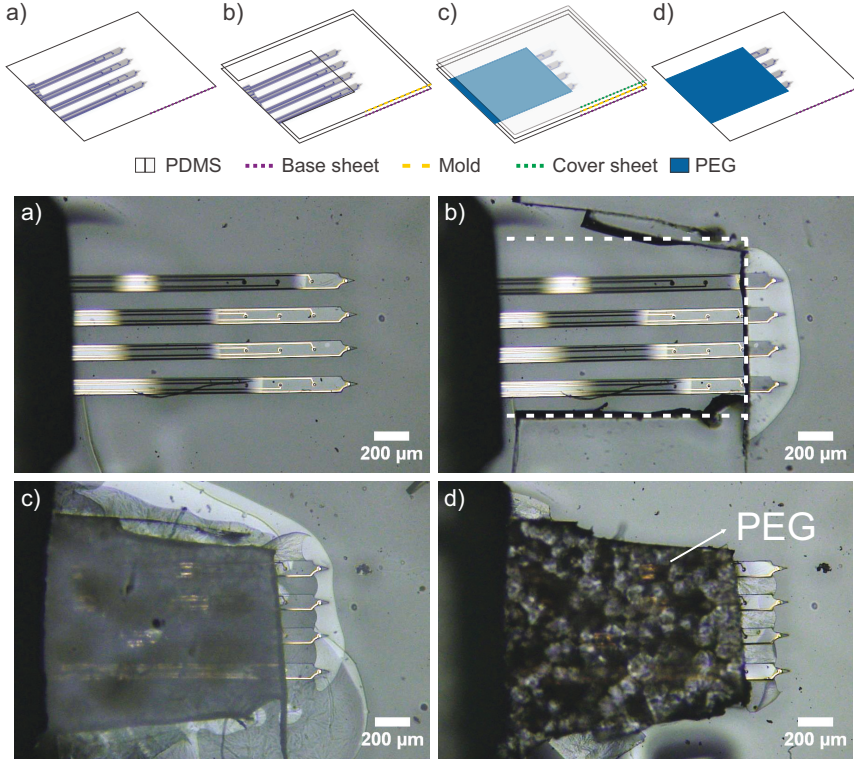[1] $P_{cr} = \frac{\pi^2 E I_m}{L_e^2}$

Figure 6.3.: Manual coating approach to temporarily reduce the effective shank length. PDMS slabs were used to create a mold for casting PEG. Alignment of flexible shanks between PDMS base sheet (a) and mold covering the first 300 μm of the tips (b). Melting of PEG 35,000 g/mol (Sigma-Aldrich, Germany) on top of mold and placing the cover sheet (c). Removal of cover sheet and mold leaving shanks coated with PEG (d).

The coating procedure is a time consuming approach as single probes were manually coated. In contrast to other works [129, 130], neither a homogenous coating nor a minimum thickness was needed as PEG was used to reduce the effective probe length and was not inserted into the tissue. For the shuttle system, any biodegradable polymer could be used. In the proposed case, PEG 35,000 g/mol from the middle range of available MWs was chosen. Additionally, the unknown *in vivo* degradation was negligible as PEG was not introduced into the brain tissue. Furthermore, PEG granulate (see Figure 6.1b) was used for the shuttle system avoiding the time for preparing PEG solution since dissolving PEG in water can be difficult especially for polymers with high MW. Nevertheless, a steady hand was needed to not damage the shanks during the coating process. After a few trials, the entire procedure could be performed within ≈10 min/probe.
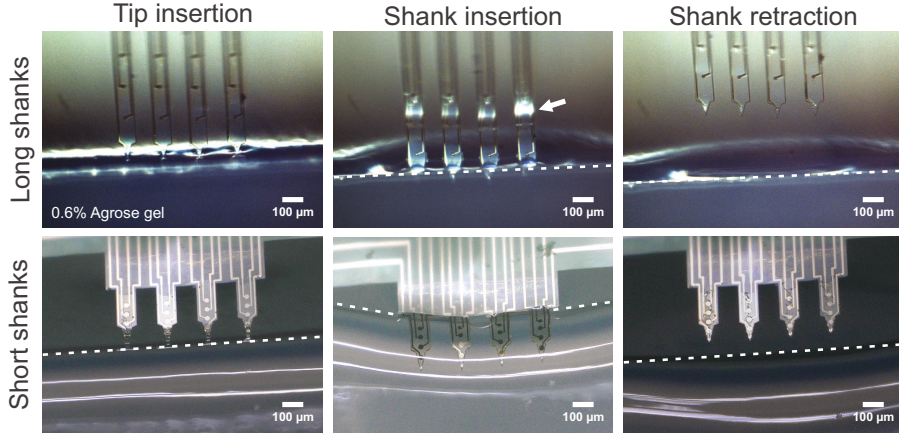
Figure 6.4.: Insertion mechanism of flexible penetrating probes: Optical images showing insertion of the 2 mm long shanks resulting in bending (arrow) in contrast to successful penetration of shanks with a length of 300 µm. Dashed line indicates surface of the 0.6 % agarose gel brain phantom.

6.3.3. Insertion test

The insertion mechanisms of the proposed shuttle system were evaluated by using 0.6 % (w/v in PBS) agarose gel brain phantoms (for preparation see A.11.1). This concentration is commonly used as the gels demonstrate comparable mechanical properties to the mouse brain (3-13 kPa [211]). Nanoindentation measurements, which were performed by the scientific associates at the Institute of Biological Information Processing 2 (IBI-2) of the Research Center Jülich, revealed that the prepared phantoms had a Young's modulus of 2-10 kPa (see Appendix A.11.2). As predicted by the theoretical calculation from Section 6.3.1, the attempt to insert 2 mm long shanks resulted in buckling (see Figure 6.4). However, with a reduction to 300 µm the flexible shanks could penetrate the gel without bending. In the next step, the A-MEA-16 probe coated with PEG was introduced into the phantom tissue (see Figure 6.5). With a speed of 7.5 µm/s, the array was slowly moved towards the gel until the exposed shank tips were inserted and the PEG reached the gel surface. Insertion speeds of compliant probes range from 8-200 µm/s [45, 129, 130, 225]. Within this work, a slow insertion was chosen to reduce penetration forces by allowing the tissue to relax around the implant [211] and because it best matched the surgical implantation (see Chapter 7). While gradually dissolving the coating, the probe was further inserted with 200 µm steps until completely introduced. The full procedure took ≈10 min but varied based on the PEG thickness and the wetness of the gel.
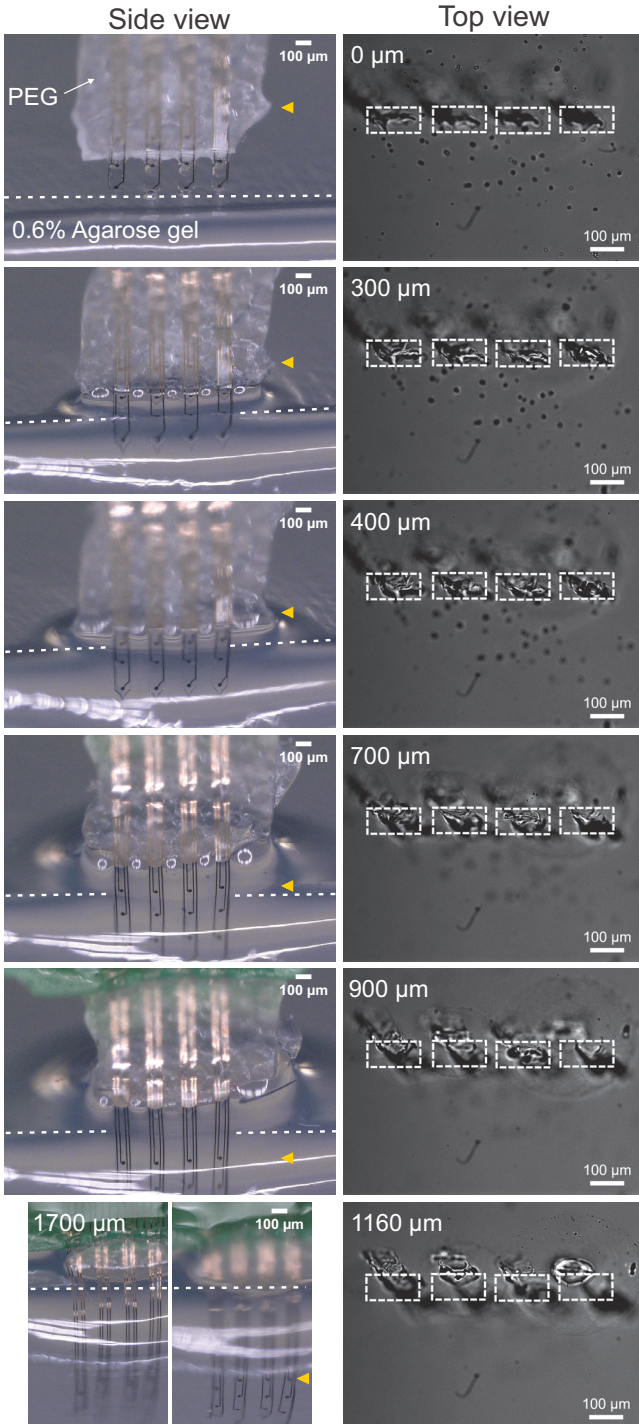
Figure 6.5.: Insertion of flexible intracortical probes into a phantom brain supported by a PEG coating. Stepwise insertion up to the full length indicated by the yellow triangle. Series of top view show punctures resulting only from the flexible shanks and not the insertion aid. As the probe was inserted at an angle, above a penetration depth of 700 μm, a slight shift was observed in the insertion holes. Dashed line indicates surface of the 0.6 % agarose gel. Side and top view were obtained from two different insertions.

Insertion aid	Compliant probe	Probe cross-section [µm^2]	Implantation footprint [µm^2]
PEG [This work]	**A-MEA-16**	**1000**	**1000**
PEG [129]	PaC/SU-8	1800	9000
Si [22]	PI	5360	16000
PVA/PLGA [130]	PaC	1520	33440
Maltose [46]	PI	2000	62000
Silk [207]	PaC	4800	62800
PEG [207]	PaC	4800	87400

Table 6.1.: Comparison of different insertion aids. Probe cross-section is obtained by multiplying shank width and thickness. For the implantation footprint, dimensions of neural implant and insertion aid were summed.

Reducing the effective length to insert compliant probes is a tissue-friendly approach as the implantation footprint is kept small. In Figure 6.5, it is clear to see that the insertion punctures within the brain phantom include the displacement originating from the flexible shanks and not additional damage from the PEG coating. In contrast to the traditional approach, where the implant is introduced into the tissue with the entire shuttle system, the implantation footprint is substantially minimized by using the proposed insertion aid (see Table 6.1). Despite the successful implantation, a shift of the insertion punctures was observed above a penetration depth of 700 µm (see Figure 6.5). As this displacement increased with penetration depth, it was assumed that the probe was inserted at an angle into the phantom and not perpendicular to the gel surface. To validate if compliant intracortical implants can be successfully implanted into target regions of real brains, the proposed shuttle system was tested under acute *in vivo* conditions (see Chapter 7).

6.3.4. Towards a wafer-scale shuttle system

After developing the above mentioned PEG coating as a shuttle system for flexible probes, the next goal was to increase the coating efficiency by going towards ready-to-use devices where the coating should be established on a wafer-scale before releasing the probes. When designing a wafer-scale coating, several criteria need to be fulfilled. The mold that determines the insertion system's thickness should have a certain height so that the flexible probes are sufficiently reinforced for a successful implantation. Additionally, after the PEG drop casting, no liquids should be involved in the following process steps because the biodegradable polymer would dissolve in water as well as in commonly used organic solvents. Taking these facts into consideration, the following fabrication process was proposed: On top of the flexible probes still attached to the wafer, a PDMS mold was formed using MEMS technology (see Figure 6.6). Based on S. Oh's work [226], the mold was produced by first photolithographically structuring sacrificial posts based on AZ 125nXT-10A (MicroChemicals, Germany). After spin-coating and curing PDMS on top of the

resist, the edges of the latter were exposed via RIE. Within the following lift-off step, the sacrificial posts were dissolved in acetone leaving the patterned PDMS mold. PEG 35,000 g/mol (Sigma-Aldrich, Germany) was used to coat the probes through doctor blading and the PDMS mold was removed. The details of the PDMS mold fabrication are provided in the Appendix A.12. MEMS technology is commonly restricted to planar structures with low aspect ratios, therefore not many thick photoresists are commercially available. As with AZ 125nXT-10A (MicroChemicals, Germany) thicknesses up to 120 µm by single coating and 200 µm by double coating with straight side walls could be achieved [227] this ultrathick resist was considered for creating the sacrificial posts. Furthermore, the lithography process is time-saving in contrast to *e.g.* SU-8 and the resist can be easily stripped in solvent-based solution [228], which is crucial for the proposed lift-off approach. Commonly, SU-8 molds are used to pattern PDMS slabs, which would involve a transfer of the latter onto the 4 inch Si wafer with the neural probes with the risk of damaging the polymer slab and misalignment. Dry etching could be considered to structure PDMS. However, with an etching rate of 0.5-1 µm/min [121, 226, 229] patterning a PDMS slab would be time-consuming. Thus, working with sacrificial posts significantly reduced the process time yet for a controlled lift-off with straight PDMS side walls, the thicknesses of the PDMS and of the

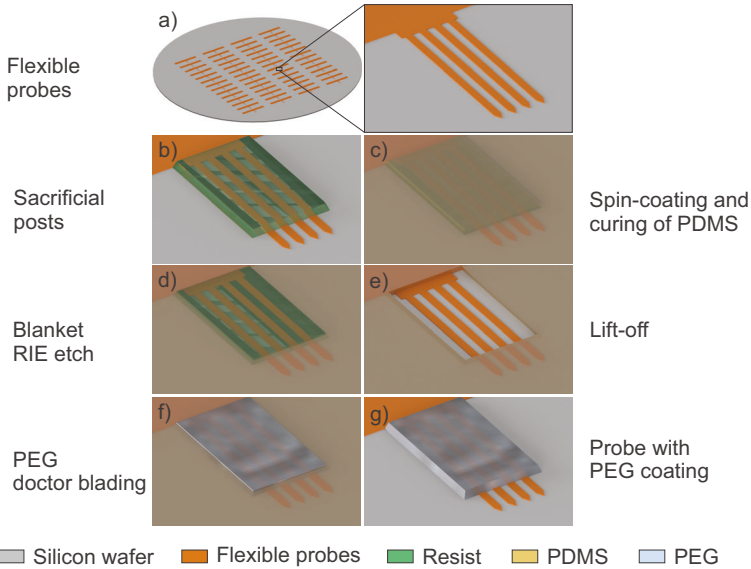**Figure 6.6.:** Fabrication flow for the wafer-scale insertion system: After producing flexible probes on a 4 inch Si wafer (a), the sacrificial posts were photolithography patterned (b) and covered with PDMS (c). Within the following RIE step, the edges of the posts were exposed (d) and the resist dissolved in acetone resulting in a patterned PDMS mold (e). PEG was doctor bladed (f) before removing the mold (g).
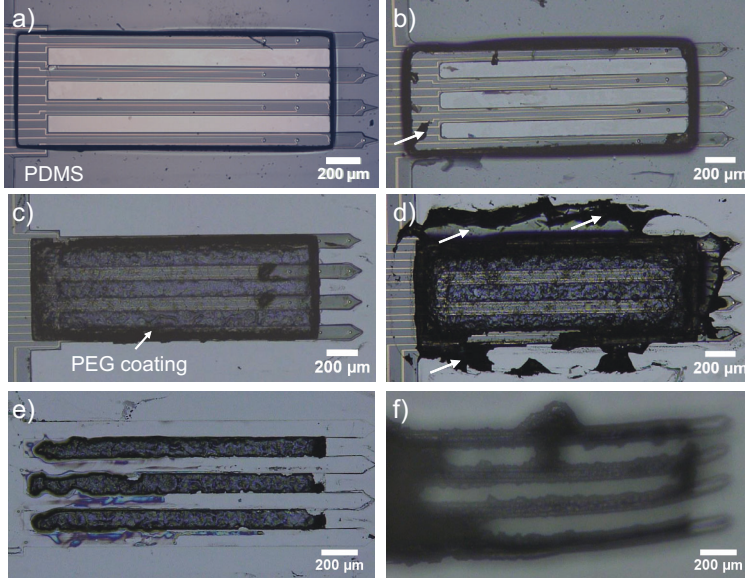
Figure 6.7.: Fabrication challenges of the wafer-scale PEG coating approach: PDMS mold produced on top of the flexible intracortical probes with the heights of 62±3 µm (n=3) (a) and 95±7 µm (n=3) (b). Residues of PDMS were observed occasionally for the thicker slab (b) arrow. Mold release was difficult (c), however not feasible for the thicker slab without residues (d) arrows. Probe release resulted in PEG residues on carrier wafer (e) and bent shanks (f).

resist, and the etching parameters had to be well adjusted. After the lithography process, the resist thickness was measured with a profilometer at several points on the wafer. Within this work, thicknesses of either 95±4 µm (mean±std, n=3) or 145±12 µm (mean±std, n=3) could be obtained by a single coating using AZ 125nXT-10A (MicroChemicals, Germany). Based on the standard deviations for the thicknesses, the resist had a good coating uniformity over the entire wafer, which slightly decreased for the thicker film height. As suggested by S. Oh's, et al. [226] it was aimed to have a thin layer of PDMS on top of the resist which was dry etched before the stripping. Therefore during the spin-coating step, the PDMS was tuned to be 20-25 µm thinner compared to the sacrificial posts and during the dry etch process, the polymer slab was further reduced by 15 µm. Figure 6.7 a-b) shows the produced PDMS molds with heights of 62±3 µm (mean±std, n=3) and 95±7 µm (mean±std, n=3). The sidewalls were straight for both heights, however seemed to be more vertical for the lower one. Furthermore, residues were occasionally observed around the edges for the thicker mold. These differences were crucial for the upcoming PDMS release and will be further discussed in the text below.

Similar to the manual coating process, PEG granulates were melted and doctor bladed to fill the mold and allowed to solidify at RT. However, this approach resulted in a thick layer of biodegradable polymer on top of the mold that hampered mold release. To overcome this issue, 30 % (w/v) PEG 35,000 g/mol was used. After oxygen activation (O_2, 80 W, 0.8 mbar, 3 min), the PEG solution was deposited through doctor blading and dried in the oven at 70 °C for 15 min to speed up the solidification. No matter which PEG option was used, the removal of the PDMS mold remained difficult as residues were left, especially at the edge of the flexible probes. To facilitate the release different anti-adhesion layers were tested. Within nanoimprint lithography, self-assembled films are commonly used to facilitate the peel off of PDMS from Si wafers and molds [230]. Therefore after patterning the sacrificial posts, the wafer was exposed to the vapour of Trichloro(1H,1H,2H,2H-perfluorooctyl)silane (Sigma-Aldrich, Germany) in a desiccator at 45 mbar for 1.5 h under Ar atmosphere. The silanization indeed helped to avoid PDMS sticking to Si however, the peeling off from the PaC probes was not possible. The next approach was to use 2 % (v/v) Micro90 (International products cooperation, USA), an anti-adhesion soap solution usually used to facilitate the removal of PaC. As this method worked well, the wafers were treated with Micro90 before spin-coating PDMS (see Appendix A.12). Furthermore, the thickness of the PDMS mold played a crucial role for a successful peel off. While the release of the 95 µm thick slab was feasible the removal of the thinner slab with a height of 62 µm was challenging, as the PDMS ruptured so that only small pieces could be peeled off. However for the thicker slab, residues were left at the edge of the flexible probes probably due to the steeper sidewalls as described above (see Figure 6.7 d). Nevertheless, a PDMS mold with a height of 95-100 µm seems to have the potential to establish the wafer-scale PEG coating. To implement this, sacrificial posts with a height of 140-150 µm and with vertical sidewall profiles are needed. The photolithography parameters of AZ 125nXT-10A (MicroChemicals, Germany) should be optimized or a different resist such as AZ 40XT (MicroChemicals, Germany) tested to establish such posts.

The final step was the release of the PaC probes with the PEG coating on top. PaC devices can be easily peeled from the Si with the aid of a few drops of DI water if needed. As PEG dissolves in water as well as in solvents this dry release of PaC probes was crucial for the success of the proposed wafer-scale approach. Unfortunately, it was not possible to remove the final probes without leaving PEG residues on the carrier wafer. Especially in between the shanks the PEG stuck to the wafer (see Figure 6.7 e). Additionally, the shanks were bent, which impedes the successful insertion (see Figure 6.7 f). Before the deposition of the PEG, a release layer could be introduced, such as mineral oil, to facilitate the peeling off. To minimize the force needed to release the probes, and thereby avoiding bending, the flexible implants and the PEG coating could be produced on a PaC sacrificial layer and not directly on top of the Si wafer. In the final step, the probes with the PEG coating are not dry released individually but rather released at once by peeling off the PaC sacrificial layer. However, introducing an additional PaC layer can make

the fabrication even more sensitive to failure as small defects in the layers can lead to complete delamination.

Despite the promising design idea, a high through-put coating could not be realized. However, individual steps could be implemented. A PDMS mold was produced on top of the flexible probes still attached to the wafer using MEMS technology. Furthermore, a coating was established by filling the mold with molten PEG and peeling off the mold. However, the release of the mold after PEG deposition and the release of the coated PaC probes with the PEG coating on top remained challenging. Surface pre-treatments might facilitate the release however, when working with different polymers, the chemical composition of the surfaces needs to be considered. For example, it was observed that a silanization with Trichloro(1H,1H,2H,2H-perfluorooctyl)silane facilitated the release of PDMS from Si wafers however, not from PaC films. After establishing a wafer-scale coating, the packaging and sterilization of the compliant probes need to be adapted to the low melting temperature and hydrolytic degradation mechanisms of PEG. The soldering process described in Section 4.4.1 could be further applied if a monolithically integrated cable is implemented in the probe design increasing the distance between the shanks with the PEG coating and the hotplate. Furthermore, ethylene oxide sterilization using a RT system could be used to treat compliant probes before *in vivo* implantation as shown in previous works [22, 131, 231].

6.4. Conclusion

With the aim to develop an insertion aid to successfully introduce intracortical implants into neural tissue, a PEG coating was proposed that increased the buckling force threshold above the minimum insertion force by temporarily reducing the effective shank length. Through PDMS molding, a straight forward coating process was presented and successful penetration into agarose gel brain phantoms was demonstrated. Furthermore, a design idea was introduced showing that this shuttle system has the potential to overcome the time consuming coating procedure by utilizing a wafer-scale PEG deposition. Although this concept could not be implemented within this work, it is believed that with some optimization a high trough-put coating can be established. To validate if the compliant probes A-MEA-16 with the tissue-friendly insertion system can be successfully implanted into target regions of real brains (not phantoms), acute *in vivo* insertions were performed as described in Chapter 7.

7. Application of compliant intracortical probes

In an effort to produce chronically stable neural interfaces, compliant probes have been explored. Within this work, such multi-site and multi-shank intracortical implants based on PaC have been introduced for reaching cortical depths of up to 2 mm (see Chapter 4). Besides establishing a low impedance coating consisting of PEDOT:PSS (see Chapter 5), an insertion system based on a temporary PEG coating was developed and the implantation of the compliant probes was tested using agarose gel brain phantoms (see Chapter 6).

After the successful insertion into phantoms, the flexible implants were tested under more realistic conditions. Several experimental preparations are utilized to validate the performance of neural implants and to study neural circuits. Neurons dissociated from brain tissue and grown on 2D substrate such as planar MEAs are used to study electrical activity from single cells up to small networks [65, 232]. To represent the *in vivo* brain more accurately, slice preparations have been introduced to study isolated neural circuits, like the thalamocortical pathway [233, 234], while keeping the structural integrity [235, 236]. Besides the fast preparation time, peripheral factors influencing the recordings such as anaesthetics, heartbeat and respiration are eliminated [237]. Even though comparable activity was proven between slices and intact brains [238], slice preparations are only a preliminary platform to validate implants intended for chronic application. Based on the ISO for the biological evaluation of medical devices, *in vivo* animal studies are mandatory to determine local tissue responses induced by the probe insertion, degradation of polymers and, acute and chronic immune reactions [239]. Therefore, the compliant probes were inserted on the one hand into brain slices and on the other hand into intact brains within acute *in vivo* experiments. Furthermore, after successful positioning, electrophysiological measurements were performed to determine the recording performance. For the *in vivo* experiments, immunohistochemical staining was additionally utilized to verify that the compliant devices could be inserted successfully into target regions in the brain using the developed shuttle system.

7.1. Brain slice experiments

The compliant intracortical implants were validated using slices from rat cortex. The performance was compared to Si based stiff probes with comparable design, which are the state-of-the-art in cortical implants (see Section 2.1.2). As 2 mm long depth electrodes were characterized, thick slices were prepared.

7.1.1. Experimental section

Penetrating probes: The A-MEA-16 probes (see Sections 4.4.1 and 4.5) with electrochemically deposited PEDOT:PSS as electrode coating material and a temporary PEG coating as insertion aid (see Section 6.3.2) were considered for the experiments. For electrochemical deposition of PEDOT:PSS, the potentiostatic polymerization was performed for 15 s at 1 V from 0.1 % (w/v) 0.01 M EDOT (Sigma-Aldrich, Germany) and 0.7 % (w/v) NaPSS (Sigma-Aldrich, Germany) prepared in ultrapure water (see Section 5.2.1). The Si probes were fabricated at the Institut für Werkstoffe der Elektrotechnik (IWE-1), RWTH Aachen University (Germany) for an intended use as retinal implants [74]. They are Michigan-style devices consisting of 4 shanks with 3 electrodes per shaft. The rectangular electrodes were coated with 500 nm of IrOx and have a GSA of 800-1600 μm^2 with a pitch of 20 μm. Single shanks have a width of 100 μm and a thickness of 10-20 μm. Furthermore, the shaft interdistance is 150 μm and the tip has an opening angle of 50-60 °. In the Appendix, an overview of critical dimensions and properties of the different devices is provided (see A.3).

Thick slice preparation: Brains from adult pregnant rats were isolated and chopped into 1.5-2 mm thick coronal slices as described in 3.4.1. The recordings were performed with slices stored in oxygenated ACSF and completed within 4 h.

Probe insertion: The probes were inserted stepwise into the tissue with a speed of 7-12 $\mu m/s$ and a step size of 100-200 μm. The maximum depth for insertion was 1000 μm so that electrode sites were placed through half the thickness of the slices.

Chemical stimulation: When spontaneous activity could not be recorded, the extracellular potassium concentration (K^+) was increased, resulting in a depolarization of the cells. For the treatment, ACSF was prepared with 25-50 mM K^+ by equimolar substitution of KCl for NaCl. After treating the slices with high K^+ ACSF for 2-3 min, they were kept in regular ACSF.

MEA recording: The data acquisition system is described in 3.4.3. During the recording, the data was high-pass filtered at 1 Hz. The raw data was analysed offline using custom software written in Python 3 [76]. To extract extracellular APs, the raw data was filtered using a 5th order Butterworth band-pass (300 Hz-9 kHz). Fast and slow network oscillations were isolated by band-pass (150-300 Hz) and low-pass (50 Hz) filtering, respectively.
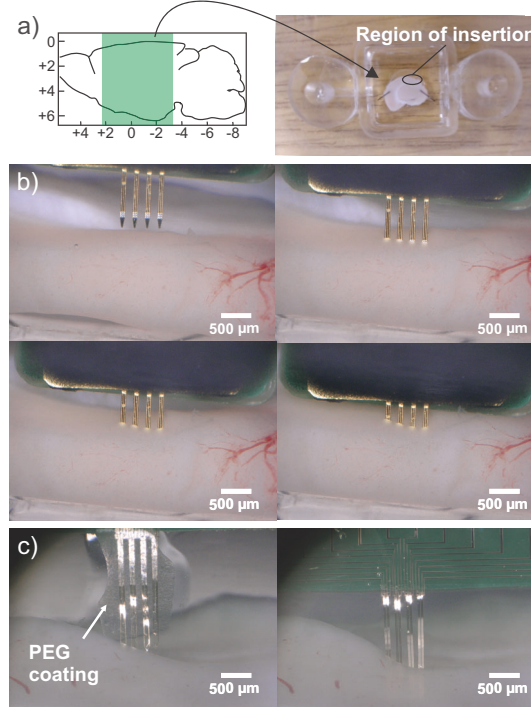
Figure 7.1.: 1.5-2 mm thick coronal slices of adult rats were prepared for the slice recordings. The green marked rectangle (a, left) represents the brain region used for the experiments. The slices were fixed within a glass chamber using insect pins and perfused with oxygenated ACSF during the recordings (a, right). Stiff (b) and compliant (c) intracortical probes were stepwise inserted into the cortex in rostro-caudal direction.

7.1.2. Slice recordings

To validate if the compliant probes with temporary PEG coating introduced within this work can be successfully implanted into target regions, brain slice experiments were performed. 1.5-2 mm coronal slices from both hemispheres were prepared and the devices were inserted in rostro-caudal direction into the cortex (see Figure 7.1 a). Moreover, all the recordings were from the dorsal and medial edge of the slices to record from brain regions similar to the *in vivo* measurements where the probes were inserted in the dorso-ventral direction (see Section 7.2). As the PEG dissolves in water, repositioning the compliant devices was not feasible. Therefore, the stiff probes were inserted to find regions with spontaneous activity and afterwards, the flexible intracortical probe were positioned nearby. Exemplary insertions with both probe types are depicted in Figure 7.1 b-c.

With both probe types, activity could be recorded in the form of spontaneous spiking
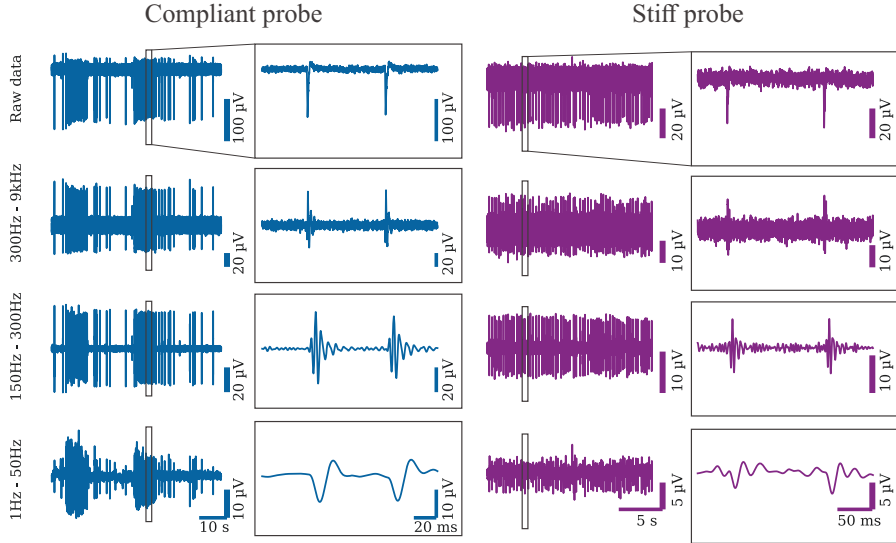
Figure 7.2.: Exemplary traces of extracellular spontaneous activity from brain slices obtained by compliant (left) and stiff (right) probes. The APs (300 Hz-9 kHz) are superimposed on slow and medium (1-50 Hz), and fast (150-300 Hz) network oscillations. Synchronization of neural firing with network oscillations can have physiological and pathological origins. As ultra-thick slices (>1.5 mm) had to be prepared to validate the intracortical probes, it is unclear if the slices exhibited seizure activity rather than healthy activity.

or chemically evoked activity after depolarization with high K^+ ACSF. Exemplary traces are shown in Figure 7.2. For all of the recordings, spiking activity was phase-locked to network oscillations. Synchronous activities within the brain can be subdivided into slow (<8 Hz), medium (8-30 Hz), and fast (30-100 Hz) oscillations [57]. The latter is defined as ripples and can have physiological and pathological origins, such as perceptual information processing [240] and paroxysmal events [241, 242], respectively. Synchronization of neural firing with network oscillations has been described in cerebral cortex [240, 243] and hippocampus [244] within *in vivo* experiments, but also using acute slice preparations.

Optimal viability of slices is only given when preparation and maintenance fulfil high quality standards. To obtain healthy tissues, a fast extraction and minimal handling of the brain is required [245, 246]. Storing the slices at temperatures similar to *in vivo* conditions (32-36 °C) is further recommended [245]. However, for the experiments shown in this work, the recordings were performed at RT. In previous works, preparation protocols have been established for either thin (150-350 μm [245]) or thick slices (500-700 μm [245, 247]). Culturing thicker slices with long-term viability is challenging due to limited media and oxygen supply of deeper layers. Thus, to the best of our knowledge, slices with a thickness of up

to 2 mm have not yet been used for extracellular recordings. To account for the fast metabolic decay of such slices, the recordings were completed within 4 h after the recovery period of 1 h. Especially, neocortical slices seem to be more sensitive in contrast to, for example, hippocampal preparations and therefore, can exhibit seizure activity rather than healthy neuronal activity [246]. In summary, even small variations within the preparation can cause changes in the slice circuits. Therefore, it is unclear if the spiking activity phase-locked to network oscillations observed within this work originates from a physiological or pathological pattern.

Tissue chambers with different media supply systems are available, such as super-fused, static and submerged [237]. Within this work, the brain slices were completely submerged in ACSF. This design was employed on the one hand to ensure that the entire slab of tissue is provided with ACSF and on the other hand to deliver and rinse out high K^+ ACSF in a fast manner. However, the constant perfusion impeded the insertion of the compliant probes with the temporary PEG coating. As the PEG dissolves when in contact with water, the flow was temporally reduced to change from a submerged to a superfused system. The positioning of the flexible implants took several minutes and spontaneous activity was not encountered, probably due to local hypoxia. Therefore, the submerged supply was kept and the probes were inserted stepwise while gradually dissolving the PEG. In contrast to the insertion into agarose gel brain phantoms (see Chapter 6), the PEG liquefied much faster when completely immersed into ACSF. The shorter time between steps impeded tissue relaxation and induced higher dimpling. Furthermore, the faster dissolution of PEG occasionally led to an insertion of only a fraction of the electrodes. To mimic the *in vivo* implantation, a dorso-ventral insertion was attempted. Such positioning was feasible with stiff probes though, the tissue dimpling was pronounced compared to the rostro-caudal insertion and no spontaneous spiking was detected. Membrane residues on the dorsal surface might hamper the positioning close enough to active cells. To overcome this, the surface was roughened. Spontaneous activity was still not recorded, probably due to the physical trauma induced during membrane removal.

Brain slice experiments have been established within the last two decades as a simplified system to study electrophysiological behaviour of neurons within isolated circuits, for example in regard to synaptic plasticity [237]. Within this work, the approach was attempted to use brain slices as a platform to characterize penetrating probes. As intracortical probes have a shank length of higher than 2 mm, well established preparations with 150-350 μm slices could not be considered but ultra-tick slices had to be prepared. Although activity in the form of spontaneous spiking or in response to stimulation with high K^+ ACSF was encountered for compliant and stiff implants, the preparation of ultra-thick slices (> 1.5 mm) still needs to be further optimized to ensure constant and healthy neuronal activity.

7.2. Acute in vivo validation

The compliant intracortical probes were evaluated within acute *in vivo* experiments. The performance was compared to single shank Si based neural probes from ATLAS Neuroengineering bvba (Belgium), which are the state-of-the-art in cortical implants for fundamental research and disease treatments (see Section 2.1.2).

This chapter was in part reproduced from the following publication:

K. Srikantharajah, R. Medinaceli Quintela, B. M. Kampa, S. Musall, M. Rothermel, and A. Offenhäusser, **Minimally-invasive insertion strategy and in vivo evaluation of multi-shank flexible intracortical probes**, *Scientific Reports*, vol. 11, 2021.

7.2.1. Experimental section

Intracortical probes: The A-MEA-16 probes (see Sections 4.4.1 and 4.5) with a temporary PEG coating as insertion aid (see Section 6.3.2) were used for the experiments. Within the fabrication, the microelectrodes were covered with 610 nm thick spin-coated (equivalent to 3 layers) PEDOT:PSS (see Section 5.2.2). The single shank Si based probes with 16 channels were purchased from ATLAS Neuroengineering bvba (Belgium, probe type: E16+R-100-S1-L6 NT). In the Appendix, an overview of critical dimensions and properties of the different devices is provided (see A.3).

Animal surgery: Details regarding the animal surgery and stimulation protocols used for the acute recordings are provided in the Sections 3.5.1 and 3.5.2.

Probe insertion: Using a syringe tip, the dura mater was punctured for the stiff probes or slits were introduced for the flexible arrays to enable implantation. The probes were inserted using a micromanipulator system (Luigs & Neumann, Germany). The compliant probe consisting of 4 shanks was slowly moved towards the brain until the exposed shank tips were positioned and the PEG coating reached the brain surface. While gradually dissolving the coating, the probe was further inserted with 100-200 µm steps up to 700-1000 µm. Similar to the compliant implants, the stiff implants were inserted stepwise into the cortex.

MEA recording: Data were recorded using a RZ5 BioAmp digital acquisition system (Tucker Davis Technologies, USA) and a sampling rate of 24 kHz (see Section 3.5.3).

Statistical analysis: The raw data was sorted and further analysed using custom software written in MATLAB 2020 (Mathworks Inc., USA) and Python 3 [76] as described in Section 3.5.4. Continuous variables such as signal amplitude and SNR are reported as mean±std and compared utilizing the Mann-Whitney-U-Test whereas categorical variables such as single unit yield and quality unit were compared employing the chi-square test. If p-values were lower than 0.05 ($p < 0.05$), differences in studied variables were considered to be statistically significant. The

tests were implemented in Python 3 [76] using the module SciPy.

Histology: To verify that the probes were inserted into target brain regions, some of the probes used for recordings were stained with DiI before insertion. After the final acute recordings, 100 µm thick coronal slices were prepared and imaged as described in Section 3.5.5.

7.2.2. In vivo electrophysiology

The *in vivo* validation of compliant implants in comparison to stiff probes was performed within acute experiments using three anaesthetized mice. The devices were inserted multiple times per animal to record spontaneous and whisker-evoked activity. Representative implantations are shown in Figure 7.3. For both probe types, simultaneous multichannel recordings were achieved from the barrel cortex. An exemplary comparison is depicted in Figure 7.4. A total of 13 trials using three flexible intracortical arrays and 8 trials using two stiff probes were recorded and considered for the subsequent analysis. To verify the physiological nature of the isolated spikes, the whiskers were stimulated and correlated to evoked population and spiking activity (see below). In Figure 7.4 (bottom) the LFPs of one electrode is shown after averaging over the 50 stimulation trials.

The performance of the different devices was evaluated utilizing quality metrics such as spike amplitude, background noise and SNR. After extracting the spikes employing amplitude thresholding, and sorting them, the clusters were distinguished in single units and multiple units. Assuming a refractory period of 2.5 ms, clusters with a RPV less than 1%, and with more than 100 individual spikes were classified as single units. In Figure 7.5, the ISI and the superimposed waveforms of representative single and multiple units are shown. Additionally, the peri-stimulus time histogram and raster plot show a high correlation of these units to the whisker stimulus.
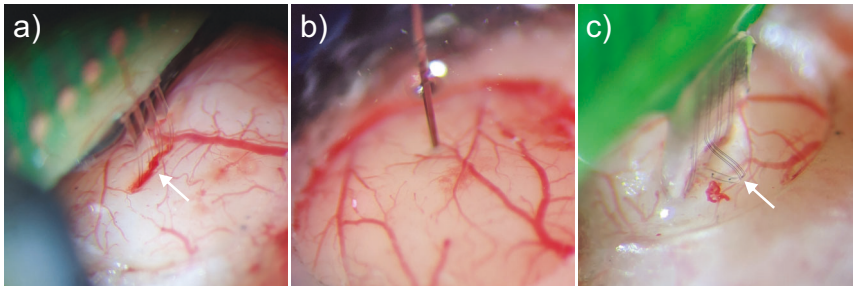

Figure 7.3.: Insertions of compliant (a, white arrow) and stiff (b) intracortical probes into the mouse barrel cortex. Example of a failed insertion (c, white arrow) resulting in implantation of three out of four shanks.
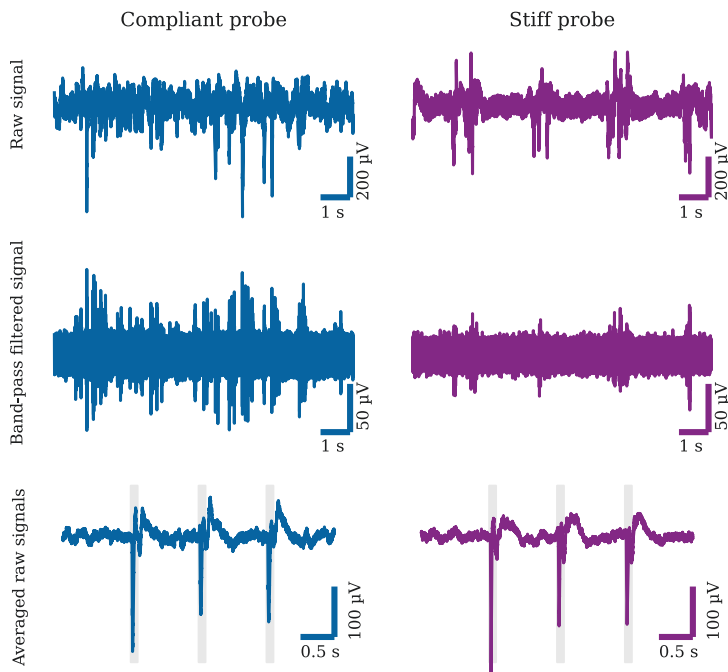
Figure 7.4.: Exemplary multichannel recordings of compliant (left) and stiff (right) neural probes. 10 s raw (top) and band-pass filtered traces (5th order Butterworth band-pass, 300 Hz-10 kHz) (centre). LFPs in response to whisker-stimulation are shown by averaging the raw signal over the 50 stimulation trials (bottom). The stimulation pulses are represented by grey boxes.

In total, 204 and 195 units, and 16 and 24 units/probe were extracted for compliant and stiff neural probes, respectively. As the recording sites of the stiff devices were packed more densely compared to the compliant probes (see Table A.3), the number of units per probe was higher for the stiff probes. The yield of single units was comparable for both device types as they composed 27 % of the total units (p=0.949, chi-squared test). Furthermore, the performance of both probe types was similar with regard to signal amplitude (0.342, Mann-Whitney-U-Test) and SNR (0.788, Mann-Whitney-U-Test) of the SUAs (see Table 7.1). One exception was the amplitudes that were slightly higher for signals recorded with the flexible arrays. Furthermore, 20 % of the SUAs recorded with the compliant devices had a SNR higher than 4 with a maximum of 7.166, whereas only 11 % quality units (SNR>4) were detected with the stiff probes with a maximum of 4.853 (p=0.330, chi-squared test) (see Figure 7.6). For MUAs, the difference was significant, as five times more high quality units were detected for compliant implants compared to
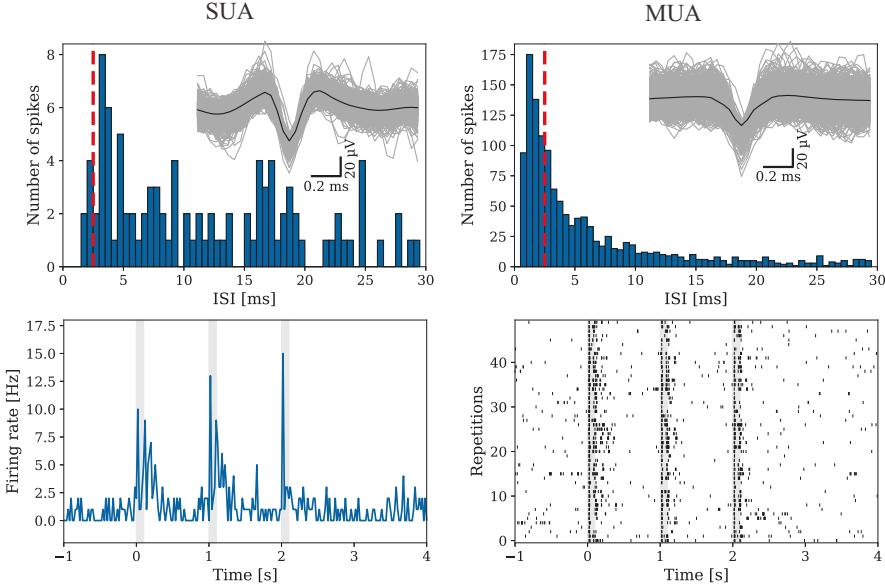
Figure 7.5.: Exemplary single-unit activity (SUA) (left) and multi-unit activity (MUA) (right) recorded with the compliant intracortical implants. ISI distribution and superimposed spike waveforms of the isolated spikes (top). Units where less than 1 % of the ISIs are below 2.5 ms (red dashed line) were classified as single units. The mean waveforms are represented by the black lines. The corresponding peri-stimulus time histogram (bottom, left) and raster plot (bottom, right) show a high correlation between stimulation and firing rate. The stimulation pulses are represented by grey boxes.

the stiff devices (p<0.001, chi-squared test). In contrast to stiff substrate materials, the acute trauma inducing neuronal death around the implant is reduced when using compliant probes [15, 248]. Additionally, the bulky insertion system was not introduced into the brain. This enables a closer contact between healthy tissue and device and therefore, can result in higher signal amplitudes due to a better coupling between neurons and electrodes (see Sections 2.2.3 and 2.2.4), indicating a better biointegration.

Furthermore, DiI stainings showed that the flexible arrays were inserted successfully into target brain regions. An exemplary insertion of compliant probes is depicted in Figure Figure 7.7 a). Within this work, a PEG coating was proposed that increased the buckling force threshold above the minimum insertion force by temporarily reducing the effective shank length. Therefore, it is worth mentioning, that it was indeed possible to insert PaC based intracortical implants with a shank cross-section per electrode of $250\,\mu m^2$ up to $2\,mm$ into the tissue without introducing the shuttle system into the tissue.

During the implantation of the compliant devices some difficulties were encountered.
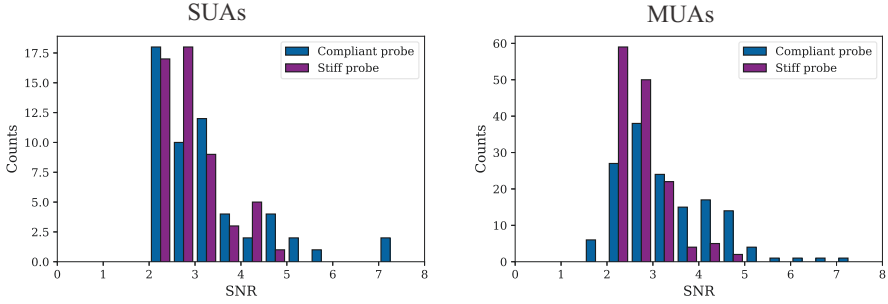
Figure 7.6.: Distribution of the signal-to-noise ratios (SNRs) obtained with compliant and stiff intracortical probes. SNRs were determined for single-unit activities (SUAs) (left) and multi-unit activities (MUAs) (right).

As compliance is achieved by minimizing probe dimensions and employing low Young's moulds polymers (see Sections 2.1.3, 4.1, and 4.2), implantation of such

	Compliant probes	**Stiff probes**
Total number of isolated units	204	195
Single units [%]	27 (55/204)	27 (53/195)
Mean amplitude [µV]	47.956±17.972	41.847±8.724
RMS noise [µV]	7.382±1.312	7.156±0.859
SNR	3.267±1.201	2.949±0.653
Maximum SNR	7.166	4.853

Table 7.1.: Summary of the multichannel recordings in regard to isolated single units obtained with compliant and stiff neural probes. Continuous variables are reported as mean±std.
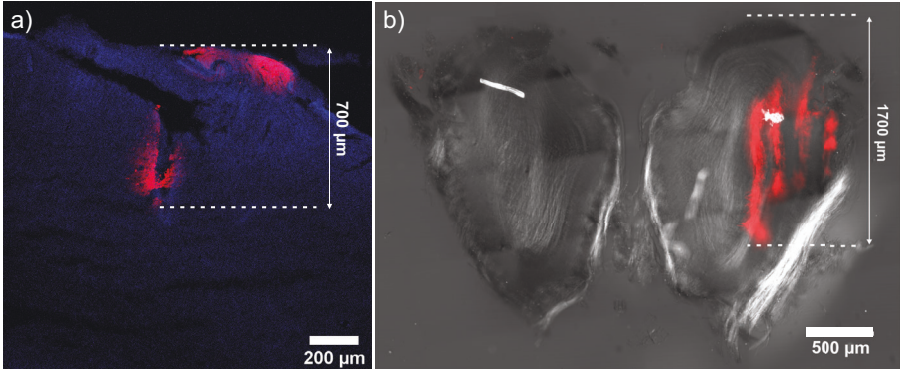

Figure 7.7.: Penetration paths stained with DiI (red) depicting successful insertion of the compliant intracortical probes. Implantation into the barrel cortex (a) superimposed to stained nuclei (DAPI, blue) and into the olfactory bulb (b), where the four single shanks of the probe could be distinguished.

probes becomes challenging compared to stiff devices. Insertion forces higher than 10 mN are needed to penetrate through the dura mater [210, 249] with a Young's modulus of 0.4-1.2 MPa [6]. Therefore, compliant implants are unable to penetrate the dura mater due to their low buckling force threshold, even when mechanically reinforced during insertion using a biodegradable polymer coating. Dura removal can cause brain swelling and vascular damages [24]. Having a future chronic application in mind, the dura mater was not removed during the animal surgery. Slits were introduced into the dura mater using a syringe tip to insert the probes. As the compliant array consisted of four shanks, either one long slit or four small slits were used. However, inserting all four shanks without getting caught on the slits' edges was challenging. Especially when using single slits for each shank, either the slits were too small for single shanks or not aligned properly. Another issue was that the brain surface was dabbed dry, to enable a controlled dissolution of the PEG coating and consequently, a controlled insertion. Dried out tissue can cause closing of the slits and affect the neural activity. If the tissue was too wet, the PEG coating got soaked in saline when approaching the brain surface. A quick retraction of the probe and removing excess saline could solve the problem. However, reusing these devices was not always feasible as the shanks de-attached from the PEG coating, or resulted in inserting only a fraction of shanks as shown in Figure 7.3 c). To avoid this, the biodegradable coating should enclose the arrays as proposed by H. Xu *et al.* [45] and not only be deposited on top of the shanks (see Section 6.3.2). Furthermore, as the mouse barrel cortex is permeated by blood vessels (see Figure 7.3), it was difficult to find suitable spots for the multiple implantations, especially for the compliant arrays spanning 700 µm.

To further validate the flexible probes, they were inserted into the mouse olfactory bulb. The main differences between the two surgeries are that the size of the craniotomy is much bigger for the olfactory bulb (1-2 cm^2), the dura mater was removed, and this brain area is less permeated by blood vessels. Therefore, inserting the implants was much easier. Additionally, the probes were inserted up to 2 mm into the olfactory bulb in contrast to the insertions into the barrel cortex with a maximum depth of 1 mm (see Figure 7.7 b). However, the tissue dimpling was more pronounced when introducing the compliant probes into the olfactory bulb as the dura mater stabilizing the tissue was removed.

7.3. Conclusion

In efforts to produce next-generation neural chronic interfaces, the Michigan-style compliant array A-MEA-16 in combination with a low impedance coating and a tissue-friendly insertion system were developed within this work. Before validating the long-term performance, the devices were tested within acute experiments. The intracortical implants with a shank cross-section per electrode of 250 µm^2 could be successfully inserted into target brain regions such as the barrel cortex as shown

by recordings of whisker-evoked activity and histological reconstruction of the penetrations. The compliant implants comprising recording sites with a GSA of $113\,\mu m^2$ were able to simultaneously record SUAs, MUAs, and LFPs with a performance comparable to state-of-the-art stiff probes. Additionally, more quality units were isolated from the recordings using compliant devices in contrast to stiff probes, indicating a better biointegration under acute conditions. Studying spiking activity synchronized to network oscillations involved in memory formation [243, 250] or mechanisms underlying focal epilepsy [251] are some examples were simultaneous detection of slow and fast activity with high spatio-temporal resolution is a desirable feature of neural probes.

Despite the successful application, the PEG coating used as an insertion system and the surgical procedure need to be further optimized to facilitate the implantation. To reduce insertion failures, the PEG coating should enclose the array. As shown within animal surgeries targeting different brain regions, the insertion of the compliant probes was easier with a durotomy. However, the removal of the dura mater increases surgical time, brain swelling and vascular damage [24] and would not be favourable for chronic implantations. Therefore, it is crucial to consider the intended application, including target brain region and surgical procedure, when designing a compliant intracortical probe and the appropriate shuttle system.

8. Summary and outlook

Over more than half a century, neural interfaces have been advanced from fundamental research to the treatment of neurodegenerative diseases. Within the last years, compliant neural probes have been explored as possible candidates to improve long-term stability by reducing the mechanical mismatch between the device and neural tissue. Inspired by these attempts, compliant intracortical implants were produced within this work. With the goal to reach brain regions like the mouse visual or barrel cortex, Michigan-style A-MEA-16 probes with 2 mm long shanks were designed and such devices with a cross-section per electrode of 250 µm² fabricated employing PaC.

To improve the recording quality of the developed implants, an electrode coating was established utilizing the conductive polymer PEDOT:PSS. Seeking a good conductivity, fast fabrication process, and stable electrochemical performance, spin-coated PEDOT:PSS crosslinked with EG, GOPS and DBSA was compared to electrochemically deposited PEDOT:PSS obtained under potentiostatic condition. Both coating methods exhibited superior electrochemical characteristics in contrast to bare Pt microelectrodes. When comparing similar thicknesses obtained with both methods, the CSCs were comparable whereas the impedances were significantly lower for spin-coated films. The abiotic stability was validated utilizing an accelerated ageing test and potential cycling. Both PEDOT:PSS coatings exhibit poor robustness. Therefore, the stability of PEDOT:PSS needs to be further optimized to be compatible with chronic implantations. Electrodes coatings such as Pt grass and IrOx might exhibit a better stability. However, compared to these electrode coatings, PEDOT:PSS films are more attractive for intracortical implants as they exhibits a lower Young's modulus and therefore, reduce the mechanical mismatch between the electrode and neural tissue [151]. Additionally, conductive polymers can be incorporated with neurotrophic or anti-inflammatory bioactive agents [8].

Paradoxically, compliant implants able to minimize the FBR are unable to penetrate the brain due to the low buckling force threshold. As many of the proposed insertion systems substantially increase the implantation footprint and consequently the acute trauma, a tissue-friendly insertion aid was developed within this work to position multi-shank probes into deeper layers of the brain. A PEG coating was introduced that increased the buckling force threshold by temporarily reducing the effective shank length. This was successfully validated using phantom tissues. Furthermore, a design idea was proposed towards a wafer-scale coating procedure

to circumvent the time-consuming manual process.

After establishing a low impedance coating and a tissue-friendly insertion system, the developed intracortical implants were validated under acute *in vivo* experiments. The flexible arrays with a shank length of 2 mm and a cross-section of 250 μm² could be successfully implanted into the barrel cortex without inserting the bulky PEG coating into the tissue. Furthermore, recordings of spontaneous and whisker-evoked activity showed that the compliant devices, comprising recording sites with a GSA of 113 μm², were able to simultaneously record SUAs, MUAs, and LFPs. In addition, the performance was comparable to commercially available state-of-the-art Si probes. However, more quality units (SNR>4) were detected using the compliant intracortical implants with a maximum SNR of 7 indicating a better biointegration within acute experiments.

From the technology perspective, a variety of modifications can be considered to further advance the compliant neural devices. For example, three-dimensional (3D), high-density arrays need to be developed to cope with the densely packed neurons within the nervous system and to reach the 3D space of the tissue. With the aim to increase electrode density but keep the small cross-section, the double-metal-layer process based on photolithography has been proposed within this work (see Section 4.5). Further optimization towards high-resolution patterning can be achieved via e-beam lithography [48]. To produce 3D probes, stacking [36] and folding [252] of two-dimensional (2D) planar probes can be considered. Additionally, the thermoforming properties of PaC [28] provides the possibility to create 3D structures from flat PaC films as shown by thermally bending the shanks of the C-MEA-32 probes (see Figure 8.1). In contrast to 2D shanks, inserting 3D compliant implants becomes even more challenging. This demands for a further optimization of the insertion systems to successfully introduce such probes into target brain regions. Considering the temporary PEG coating proposed within this work, inserting 2D probes one after the other might be another solution to reach the 3D tissue.
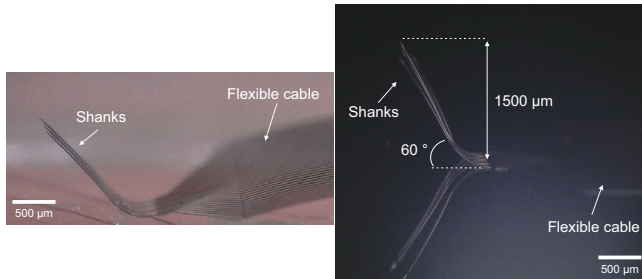

Figure 8.1.: Thermoforming of PaC based neural probes. The C-MEA-32 probes (see Section 4.5) were aligned between a Teflon mold and the shanks were thermally bent at 200 °C and 48 h under vacuum and nitrogen purging to prevent oxidative degradation.

Based on the promising outcomes of the acute experiments, the next step is the chronic implantation of the developed neural probes to validate long-term stability. For such future experiments, the C-MEA-32 probes were designed (see Section 4.5) as the monolithically integrated flexible cable enables a free-floating probe fixation. The designed headmount is appropriate for rats however, for mice experiments, the PCBs should be reduced in size. Additionally, a shuttle system is needed to support the flexible cable and the PCB during the insertion [22, 44].

Within previous works, implantation up to two years showed an increased neuronal density and decreased microglial migration around compliant probes in contrast to stiff devices [15, 21]. Additionally, stable single-cell recordings using polymer based Michigan arrays have been demonstrated for several months [44, 49, 50]. However, long-term recordings exceeding one year still need to be pursued. The chronic stability of implantable devices depends on several factors, for example the insertion conditions. Properties like probe substrate material, its surface characteristics, probe dimensions, insertion speed, tethering scheme, and tissue properties influence the force experienced by the implant and the tissue dimpling during implantation [4, 16]. Besides optimizing the devices' mechanical characteristics, it has been shown that bioactive coatings or topographical cues play a role in probe acceptance during the indwelling period by preventing inflammatory cell attachment and facilitating neuronal adhesion [4, 253]. Additional abiotic factors like delamination of passivation layers, corrosion of electrode coatings, and interconnection failure can impede the long-term device performance [16]. In summary, the interplay between device and tissue properties, and the implantation conditions contribute to the FBR and the long-term acceptance of intracortical implants. Therefore, further work is needed to fully unravel the complex interactions between the neural interface and the nervous system and to design chronically stable implants meeting the specifications for seamless biointegration.

A. Appendix

A.1. Fabrication protocol of PaC based single-metal-layer devices

1. Cleaning of 4 inch silicon wafers:

   a) Acetone bath for 10 min using ultrasonication

   b) Isopropyl alcohol bath for 10 min using ultrasonication

   c) Rinsing with deionized (DI) water

   d) Spin drying

2. ParyleneC deposition as substrate layer
   (PDS2010 Labcoater from Specialty Coating Systems, Inc., USA):

   a) Dimer: 8.5 g (5 μm)

   b) Furnace Temperature: 690 °C

   c) Chamber Gauge Temperature: 135 °C

   d) Vaporizer Temperature: 160 °C

   e) Vacuum Pressures: SP=25, PLA1=20

3. Patterning metal interconnections and electrode sites:

   a) Dehydration at 150 °C for 5 min

   b) Plasma treatment: O_2, 50 W, 80 sccm, 2 min, with installed Faraday cage (TePl GigaBatch 360M, Germany)

   c) Spin-coating of LOR3b (MicroChemicals, Germany): 500 rpm, ramp rate 200 rpm/s, 5 s and 2000 rpm, ramp rate 500 rpm/s, 30 s

   d) Soft baking at 150 °C for 5 min

   e) Spin-coating of AZ nLOF2020 (MicroChemicals, Germany): 500 rpm, ramp rate 200 rpm/s, 5 s and 3000 rpm, ramp rate 500 rpm/s, 30 s

   f) Soft baking at 110 °C for 1 min

g) UV exposure: $40\,\mathrm{mJ/cm^2}$ (hard contact)

h) Post-exposure bake at $110\,°C$ for $1\,\mathrm{min}$

i) Development in AZ MIF 326 (MicroChemicals, Germany) for 33-35 s

4. Metal evaporation:

a) Plasma treatment: O_2, 50 W, 80 sccm, 2 min, with installed Faraday cage (TePI GigaBatch 360M, Germany)

b) Electron beam evaporation (Pfeiffer PLS 570, Pfeiffer Vacuum, Asslar, Germany)

   i. Ar pre-sputtering: 150 V, 5 A

   ii. 10 nm Titanium ($0.1\,\mathrm{\mu m/min}$)

   iii. 100 nm Platinum ($0.5\,\mathrm{\mu m/min}$)

   iv. 10 nm Titanium ($0.1\,\mathrm{\mu m/min}$)

c) Lift-off in acetone for 2-3 h

d) Dipping in AZ MIF 326 for 2-5 min to remove LOR3b and rinsing with DI water

5. ParyleneC deposition as passivation layer:

a) Adhesion promoter: cover chamber walls with 1 ml gamma-Methacryloxypropyl-trimethoxysilane (A-174 Silane, Specialty Coating Systems, Inc., USA) using a cotton stick

b) Dimer: 8.5 g ($5\,\mathrm{\mu m}$)

c) Furnace Temperature: $690\,°C$

d) Chamber Gauge Temperature: $135\,°C$

e) Vaporizer Temperature: $160\,°C$

f) Vacuum Pressures: SP=25, PLA1=20

6. Patterning probe shape and electrode sites:

a) Plasma treatment: O_2, 50 W, 80 sccm, 2 min, with installed Faraday cage

b) Spin-coating of AZ 10XT (MicroChemicals, Germany): 1. layer, 2400 rpm, ramp rate 500 rpm/s, 60 s

c) Soft baking at $110\,°C$ for $1\,\mathrm{min}\,20\,\mathrm{s}$

d) Spin-coating of AZ 10XT (MicroChemicals, Germany): 2. layer, 2100 rpm, ramp rate 500 rpm/s, 60 s (Thickness: 20 μm)

e) Soft baking at 110 °C for 2 min 40 s

f) UV exposure: 2100 mJ/cm^2 (soft contact)

g) Development in AZ 400K (MicroChemicals, Germany) (dilution 1:4 in DI water) for 5-7 min

h) ParyleneC dry etch: CF$_4$:O$_2$, 4:36 sccm, 0.007 mbar, RF 50 W, ICP 500 W, 10 °C, 0.65-0.70 μm/min (Oxford Plasma Technology RIE reactor, United Kingdom)

i) Titanium dry etch: Ar:O$_2$, 20:20 sccm, 0.035 mbar, RF 50 W, 10 °C, 0.006 μm/min

j) Stripping of resist in AZ 100 Remover (MicroChemicals, Germany) using a two tank system for 5-10min and rinsing with isopropyl alcohol.

A.2. Fabrication protocol of PaC based double-metal-layer devices

1. See steps 1-2 in A.1

2. Patterning metal interconnections:

   a) Dehydration at 150 °C for 5 min

   b) Plasma treatment: O$_2$, 50 W, 80 sccm, 2 min, with installed Faraday cage (TePI GigaBatch 360M, Germany)

   c) Spin-coating of AZ nLOF2020 (MicroChemicals, Germany): 500 rpm, ramp rate 200 rpm/s, 5 s and 3000 rpm, ramp rate 500 rpm/s, 30 s

   d) Soft baking at 110 °C for 1 min

   e) UV exposure: 17 mJ/cm^2 (hard contact)

   f) Post-exposure bake at 110 °C for 1 min

   g) Development in AZ MIF 326 (MicroChemicals, Germany) for 33-35 s

3. Metal evaporation: see step 4 in A.1

4. ParyleneC deposition as interlayer
   (PDS2010 Labcoater from Specialty Coating Systems, Inc., USA):

a) Adhesion promoter: cover chamber walls with 1 ml gamma-Methacryloxypropyl-trimethoxysilane (A-174 Silane, Specialty Coating Systems, Inc., USA) using a cotton stick

b) Dimer: 0.8 g (0.5 µm)

c) Furnace Temperature: 690 °C

d) Chamber Gauge Temperature: 135 °C

e) Vaporizer Temperature: 160 °C

f) Vacuum Pressures: SP=25, PLA1=20

5. Patterning vias:

a) Plasma treatment: O_2, 50 W, 80 sccm, 2 min, with installed Faraday cage

b) Spin-coating of AZ 10XT (MicroChemicals, Germany): 5000 rpm, ramp rate 500 rpm/s, 60 s

c) Soft baking at 110 °C for 3 min

d) UV exposure: 900 mJ/cm^2 (soft contact)

e) Development in AZ 400K (MicroChemicals, Germany) (dilution 1:4 in DI water) for 3-4 min

f) ParyleneC dry etch: CF_4:O_2, 4:36 sccm, 0.007 mbar, RF 50 W, ICP 500 W, 10 °C, 0.65-0.70 µm/min
(Oxford Plasma Technology RIE reactor, United Kingdom)

g) Titanium dry etch: Ar:O_2, 20:20 sccm, 0.035 mbar, RF 50 W, 10 °C, 0.006 µm/min

h) Stripping of resist in AZ 100 Remover (MicroChemicals, Germany) using a two bath system for 5-10min and rinsing with isopropyl alcohol.

6. Patterning electrode sites and contact pads:

a) Dehydration at 150 °C for 5 min

b) Plasma treatment: O_2, 50 W, 80 sccm, 2 min, with installed Faraday cage (TePI GigaBatch 360M, Germany)

c) Spin-coating of LOR3b (MicroChemicals, Germany): 500 rpm, ramp rate 200 rpm/s, 5 s and 2000 rpm, ramp rate 500 rpm/s, 30 s

d) Soft baking at 150 °C for 5 min

    e) Spin-coating of AZ nLOF2020 (MicroChemicals, Germany): 500 rpm, ramp rate 200 rpm/s, 5 s and 2000 rpm, ramp rate 500 rpm/s, 30 s

    f) Soft baking at 110°C for 1 min

    g) UV exposure: 40 mJcm^2 (hard contact)

    h) Post-exposure bake at 110 °C for 1 min

    i) Development in AZ MIF 326 (MicroChemicals, Germany) for 33-35 s

7. Metal evaporation:

    a) Plasma treatment: O_2, 50 W, 80 sccm, 2 min, with installed Faraday cage (TePl GigaBatch 360M, Germany)

    b) Electron beam evaporation (Pfeiffer PLS 570, Pfeiffer Vacuum, Asslar, Germany)

        i. Ar pre-sputtering: 150 V, 5 A
          10 nm Titanium (0.1 µm/min)
          500 nm Gold (0.5 µm/min)
          10 nm Titanium (0.1 µm/min)
          or

       ii. Ar pre-sputtering: 150 V, 5 A
          10 nm Titanium (0.1 µm/min)
          100 nm Platinum (0.5 µm/min)
          10 nm Titanium (0.1 µm/min)
          450-500 nm IrOx

      iii. IrOx Sputtering (Nordiko 2550, UK):
          Ar pre-sputtering: 500 W, 1 min
          450-500 nm IrOx, 10 sccm O_2, 200 W
          The sputtered IrOx films were provided from the cleanroom facility at the Institut für Werkstoffe der Elektrotechnik (IWE-1), RWTH Aachen University (Germany).

    c) Lift-off in acetone for 2-3 h

    d) Dipping in AZ MIF 326 for 2-5 min to remove LOR3b and rinsing with DI water

8. ParyleneC deposition as passivation layer: see step 5 in A.1

9. Patterning probe shape and electrode sites: see step 6 in A.1

A.3. Soldering flexible probes to PCBs

1. Principe: manual flip-chip bonding

2. Place printed circuit board (PCB) on hotplate at 180 °C

3. Disperse soldering paste NC-31 (AMTECH, USA) based on 42Sn/58Bi alloy on PCB's contact pads

4. After solvent evaporation, remove excess alloy leaving alloy balls on top of the contact pads

5. With a help of a microscope, align bond pads of released transparent probes on to PCB's contact pads

6. Perform the last step at the edge of the hotplate to avoid a direct contact of the flexible probes with the hotplate

7. Remove board with probe from hotplate and let cool down

8. Seal probes soldered to PCB with epoxy EPO-TEK 302 (Epoxy Technology, USA) by mixing part A and B in a ratio of 2:1, applying the mixture around probe edges and curing at 110 °C for 30 min

A.4. PDMS based electrode array fabrication

In efforts to produce ultra-soft neural probes, PDMS was considered with a Young's modulus one-tenth lower than PaC. In the following sections, the microfabrication is described and the finale implants are presented.

A.4.1. Microfabrication

1. Cleaning of 4 inch silicon wafers:

   a) Acetone bath for 10 min using ultrasonication

   b) Isopropyl alcohol bath for 10 min using ultrasonication

   c) Rinsing with DI water

   d) Spin drying

2. Deposition of sacrificial layer:

   a) Electron beam evaporation (Pfeiffer PLS 570, Pfeiffer Vacuum, Asslar, Germany)

   b) Ar pre-sputtering: 150 V, 5 A

   c) 100 nm Al (0.5 µm/min)

3. Preparation of PDMS mixture:

   a) Use Sylgard 184 (Dow Corning, USA), a 2-component PDMS kit

   b) Thoroughly mixing base and curing agent at a ratio 10:1 and degas at -20 °C for a couple of days to remove gas bubbles

4. PDMS as substrate layer:

   a) Warming up of PDMS mixture at RT for 15-20 min

   b) Dehydration at 150 °C for 5 min

   c) Spin-coating: 500 rpm, ramp rate 200 rpm/s, 2 s and 5000 rpm, ramp rate 200 rpm/s, 180 s

   d) Curing at 110°C for 10 min

5. Metal evaporation:

   a) Electron beam evaporation (Pfeiffer PLS 570, Pfeiffer Vacuum, Asslar, Germany)

      i. 5 nm Cr (0.1 µm/min)

      ii. 50 nm Au (0.3 µm/min)

6. Chemical wet etching:

   a) Etch mask:

      i. Dehydration at 150 °C for 5 min

      ii. Plasma treatment: O_2, 50 W, 80 sccm, 2 min, with installed Faraday cage (TePl GigaBatch 360M, Germany)

      iii. Spin-coating of AZ 5214E (MicroChemicals, Germany): 500 rpm, ramp rate 200 rpm/s, 5 s and 3000 rpm, ramp rate 500 rpm/s, 60 s

      iv. Soft baking at 110 °C for 1 min

      v. UV exposure: 50 mJ/cm^2 (hard contact)

      vi. Post-exposure bake at 110 °C for 1 min

      vii. Development in AZ MIF 326 (MicroChemicals, Germany) for 60-80 s

   a) Au etching in TechniEtch ACl2 (MicroChemicals, Germany) (dilution 1:3 in DI water) for 100 s

b) Stripping of resist in acetone for 10-15 min and rinsing with isopropyl alcohol

c) Cr etching in TechniEtch Cr01 (MicroChemicals, Germany) (dilution 1:3 in DI water) for 18 s

7. PDMS as passivation layer:

   a) Warming up of PDMS mixture at RT for 15-20 min

   b) Dehydration at 150 °C for 5 min

   c) Spin-coating: 500 rpm, ramp rate 200 rpm/s, 2 s and 5000 rpm, ramp rate 200 rpm/s, 180 s

   d) Curing at 110°C for 10 min

8. Patterning probe shape and electrode sites:

   a) ParyleneC deposition as promotion layer
      (PDS2010 Labcoater from Specialty Coating Systems, Inc., USA):

      i. Dimer: 6.5 g (4 µm)

      ii. Furnace Temperature: 690 °C

      iii. Chamber Gauge Temperature: 135 °C

      iv. Vaporizer Temperature: 160 °C

      v. Vacuum Pressures: SP=25, PLA1=20

   b) Dry etching:

      i. Plasma treatment: O_2, 50 W, 80 sccm, 2 min, with installed Faraday cage

      ii. Spin-coating of AZ 10XT (MicroChemicals, Germany): 1. layer, 2400 rpm, ramp rate 500 rpm/s, 60 s

      iii. Soft baking at 110 °C for 1 min 20 s

      iv. Spin-coating of AZ 10XT (MicroChemicals, Germany): 2. layer, 2100 rpm, ramp rate 500 rpm/s, 60 s (Thickness: 20 µm)

      v. Soft baking at 110 °C for 2 min 40 s

      vi. UV exposure: 2100 mJ/cm^2 (soft contact)

      vii. Development in AZ 400K (MicroChemicals, Germany) (dilution 1:4 in DI water) for 5-7 min

viii. ParyleneC dry etch: CF_4:O_2, 4:36 sccm, 0.007 mbar, RF 50 W, ICP 500 W, 10 °C, 0.65-0.70 µm/min (Oxford Plasma Technology RIE reactor, United Kingdom)

ix. PDMS dry etch: CF_4:O_2, 45:3 sccm, 0.007 mbar, RF 100 W, ICP 500 W, 10 °C, 0.5 µm/min

x. Stripping of resist in AZ 100 Remover (MicroChemicals, Germany) using a two tank system for 5-10min and rinsing with isopropyl alcohol.

xi. ParyleneC dry etch (if needed, to remove PaC on top of PDMS probes): CF_4:O_2, 4:36 sccm, 0.007 mbar, RF 50 W, ICP 500 W, 10 °C, 0.65-0.70 µm/min

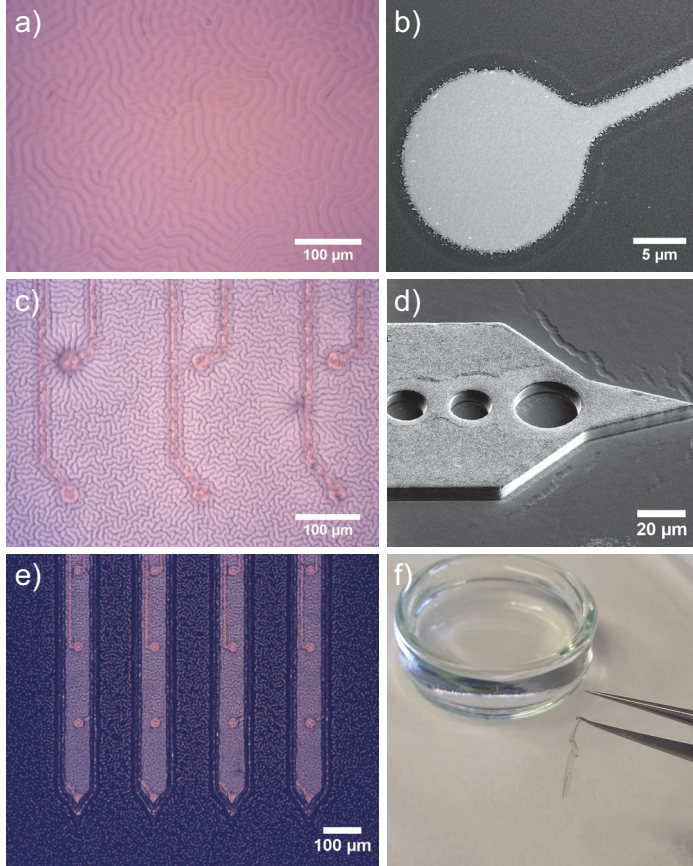## A.4.2. Ultra-flexible intracortical probes

Figure A.1.: Presentation of the PDMS based flexible intracortical implants: The morphology of Au on PDMS depends on parameters such as deposition temperature, metal film thickness and surface properties of PDMS [125]. Within this work, the e-beam evaporation resulted in a buckled morphology of Au and the underlying PDMS (a). Due to the high CTE (see Table 4.1), microfabrication of photoresists on native PDMS is challenging. Therefore, chemical wet etching was employed to pattern the metal films. SEM picture of a structured Au film on top of PDMS (b). Furthermore, PaC was used as promotion layer between PDMS and the resist etch mask used for RIE. The combination of the porous nature of PDMS and the CVD of PaC results in the permeating of PaC into the PDMS bulk [254, 255]. Therefore, after the CVD, the buckled morphology was more pronounced (c). RIE was used to pattern PDMS resulting in vertical sidewalls (d). The finale probes before (e) and after (f) release. The dark background originates from the Al sacrificial layer, which enabled a dry release of the PDMS probes (e). During RIE, the buckled morphology within the PDMS layers was transferred to the underlying Al. Intrinsic stress within the ultra-soft PDMS films caused a curling of the probes after releasing them from the carrier wafer (f).

A.5. Fabrication of PEDOT:PSS coated probes

1. ParyleneC deposition as sacrificial layer:

   a) Spin-coating of Micro90 (2 % (v/v) in ultrapure water) (International products cooperation, USA): 1000 rpm, ramp rate 200 rpm/s, 20 s

   b) Drying at RT for 5 min

   c) Dimer: 6.5 g (4 μm)

   d) Furnace Temperature: 690 °C

   e) Chamber Gauge Temperature: 135 °C

   f) Vaporizer Temperature: 160 °C

   g) Vacuum Pressures: SP=25, PLA1=20

2. Patterning electrode openings:

   a) Plasma treatment: O_2, 50 W, 80 sccm, 2 min, with installed Faraday cage (TePI GigaBatch 360M, Germany)

   b) Spin-coating of AZ 10XT (MicroChemicals, Germany): 1000 rpm, ramp rate 500 rpm/s, 60 s (Thickness: 13 μm)

   c) Soft baking at 110 °C for 3 min

   d) UV exposure: 900 mJcm^2 (soft contact)

   e) Development in AZ 400K (MicroChemicals, Germany) (dilution 1:4 in DI water) for 3-4 smin

   f) ParyleneC etch: CF_4:O_2, 4:36 sccm, 0.007 mbar, RF 50 W, ICP 500 W, 10 °C, 0.65-0.70 μm/min

   g) Titanium dry etch: Ar_4:O_2, 20:20 sccm, 0.035 mbar, RF 50 W, 10 °C, 0.006 μm/min

   h) Stripping of resist in AZ 100 Remover (MicroChemicals, Germany) using a two bath system for 5-10min and rinsing with isopropyl alcohol.

3. PEDOT:PSS solution:

   a) Filter Clevios PH-1000 (Heraeus Holding GmbH, Germany) using a syringe filter with a pore size of $0.8\,\mu m$

   b) Add 5 % (v/v) EG (Sigma-Aldrich, Germany), 1 % (v/v) GOPS (Sigma-Aldrich, Germany) and 0.1 % (v/v) DBSA (Sigma-Aldrich, Germany)

   c) Allow to stand overnight before usage

4. PEDOT:PSS coating:

   a) Plasma treatment: O_2, 50 W, 80 sccm, 2 min, with installed Faraday cage (TePI GigaBatch 360M, Germany)

   b) Spin-coating of PEDOT:PSS: 3000 rpm, ramp rate 500 rpm/s, 30 s

   c) Wait 15s between applying the solution and spin-coating for an even distribution

   d) Soft baking at 110 °C for 1 min

   e) Spin-coating of PEDOT:PSS: 500 rpm, ramp rate 200 rpm/s, 30 s

   f) Wait 15s between applying the solution and spin-coating for an even distribution

   g) Soft baking at 110 °C for 1 min

   h) Repeat last two steps until desired thickness is reached.

   i) Peeling off sacrificial layer with a few drops of DI water and a tweezer

   j) Hard baking in oven at 140 °C for 1 h

   k) Soaking in water for at least 2-3 h or overnight

   l) Dry releasing probes with tweezer

A.6. Introducing iridium oxide as adhesion layer

1. Same process to A.1

2. Perform following steps after step 4 in A.1

3. Patterning metal coating:

   a) Dehydration at 150 °C for 5 min

   b) Plasma treatment: O_2, 50 W, 80 sccm, 2 min, with installed Faraday cage (TePI GigaBatch 360M, Germany)

   c) Spin-coating of LOR3b (MicroChemicals, Germany): 500 rpm, ramp rate 200 rpm/s, 5 s and 2000 rpm, ramp rate 500 rpm/s, 30 s

   d) Soft baking at 150 °C for 5 min

   e) Spin-coating of AZ nLOF2020 (MicroChemicals, Germany): 500 rpm, ramp rate 200 rpm/s, 5 s and 2000 rpm, ramp rate 500 rpm/s, 30 s

   f) Soft baking at 110°C for 1 min

g) UV exposure: $40\,\mathrm{mJ/cm^2}$ (hard contact)

h) Post-exposure bake at $110\,\mathrm{°C}$ for $1\,\mathrm{min}$

i) Development in AZ MIF 326 (MicroChemicals, Germany) for 33-35 s

4. Metal evaporation:

   a) *The sputtered IrOx films were provided from the cleanroom facility at IWE-1, RWTH Aachen University.*

   b) Sputtering (Nordiko 2550, UK):

      i. Ar pre-sputtering: $500\,\mathrm{W}$, $1\,\mathrm{min}$

      ii. 450-500 nm IrOx, $10\,\mathrm{sccm}$ O_2, $200\,\mathrm{W}$

   c) Lift-off in acetone for 2-3 h

   d) Dipping in AZ MIF 326 for 2-5 min to remove LOR3b and rinsing with water

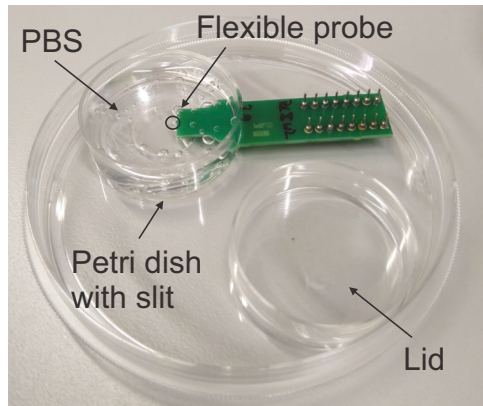## A.7. Sample holder for accelerated ageing test

Figure A.2.: Storage container used for accelerated ageing test of flexible neural probes with PEDOT:PSS as electrode coating.

A.8. PEDOT:PSS as electrode coating material
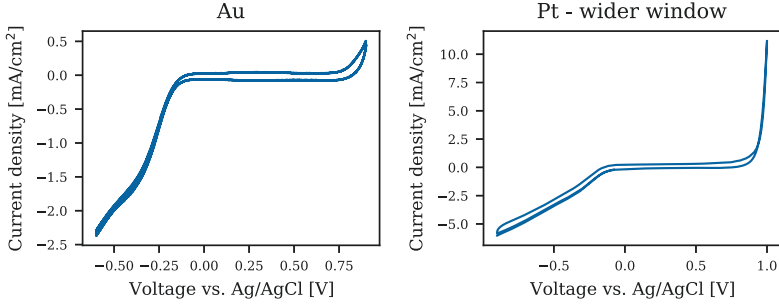
A.8.1. Platinum microelectrodes

Figure A.3.: Current over voltage curve for a Au (left) and Pt (right) microelectrode with a GSA of $113\,\mu m^2$ obtained at scan rate of $0.1\,V/s$.

A.8.2. Electrochemical deposited PEDOT:PSS

Deposition time [s]	Deposition charge [mC/cm^2]
7	53.468±4.714
10	88.556±4.284
15	142.335±15.707
20	218.096±20.640

Table A.1.: Deposition times and corresponding charges used for the electrochemical deposition of PEDOT:PSS (mean±std, n=12).

A.8.2.1. Growth mechanisms of electrochemical deposited PEDOT:PSS

The nucleation process of EDOT starts with the induction period, where the current drops to a minimum indicating the beginning of the polymerization (see Figure A.4). This step is mainly dominated by diffusion-limited oxidation of the monomers followed by coupling of radical cations until the oligomers reach a certain chain length and precipitate onto the WE. Afterwards, the propagation of polymer chains and growth of globules on the WE predominate the nucleation process resulting in an increase of the current with time ($t \sim I^{0.5}$) (see Figure A.4). For prolonged depositions times, the current rises until reaching a plateau [256,257]. The time scale of the induction phase gets shorter for increasing deposition potentials [258] and therefore, this initial phase was not detectable for all polymerization performed within this work. However, in Figure A.4, one example is shown where the current minimum is clearly visible.
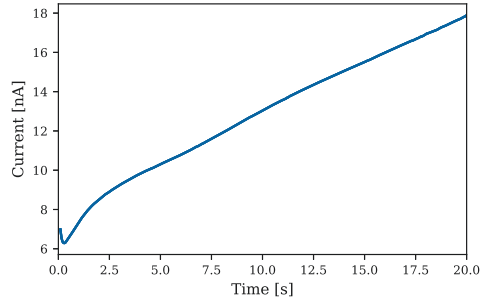
Figure A.4.: Exemplary chronoamperogram for electrochemical deposition of PEDOT:PSS at $1\,\mathrm{V}$ from $0.1\,\%$ (w/v) $0.01\,\mathrm{M}$ EDOT and $0.7\,\%$ (w/v) NaPSS. The current response depicts two characteristics transients. In the first few seconds, the current reaches a minimum indicating the start of the polymerization. Afterwards, the current increases with time following a parabolic rate law.
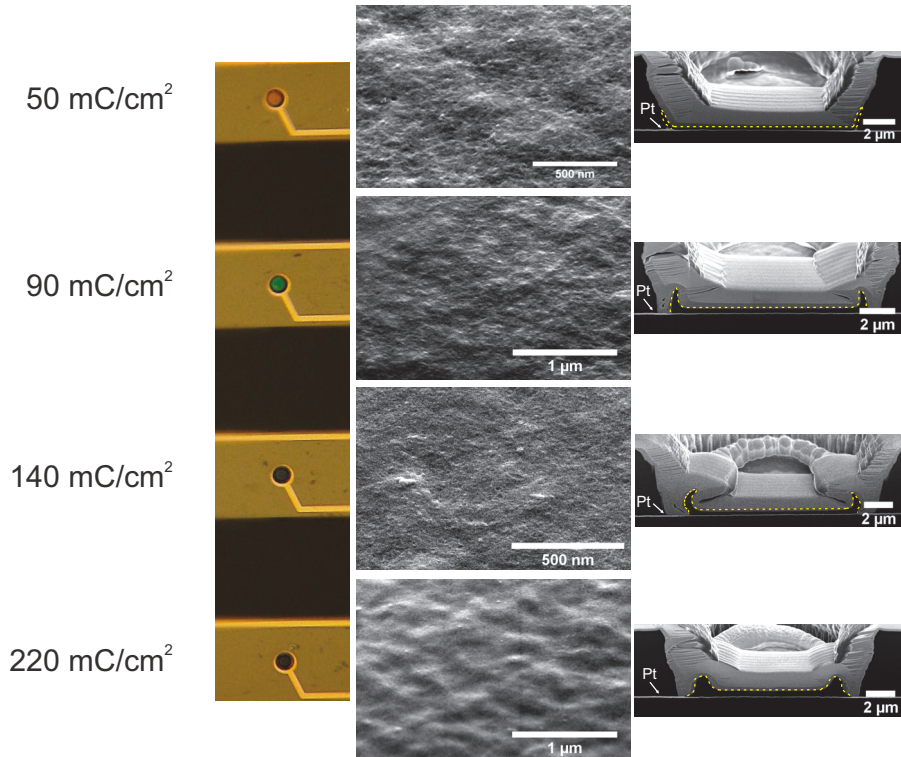

Figure A.5.: Optical images, SEM pictures and FIB sections of electrochemically deposited PEDOT:PSS for different deposition charges obtained under potentiostatic mode.
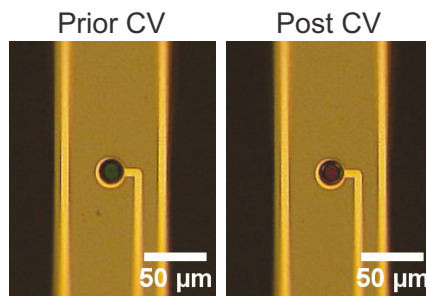
Figure A.6.: Electrochemically deposited PEDOT:PSS coating before and after CV cycling. In response to the potential cycling, the thin polymer layer at the electrode edge went off.
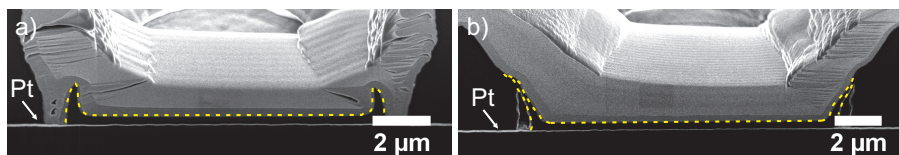

Figure A.7.: Electrochemical deposition of PEDOT:PSS without (a) and with (b) pre-treating the Pt microelectrodes utilizing an Ar etch (0.4 mbar, 100 W, 3 min). The deposition time of 15s resulted in charges of $140\,\text{mC/cm}^2$ (a) and $570\,\text{mC/cm}^2$ (b).
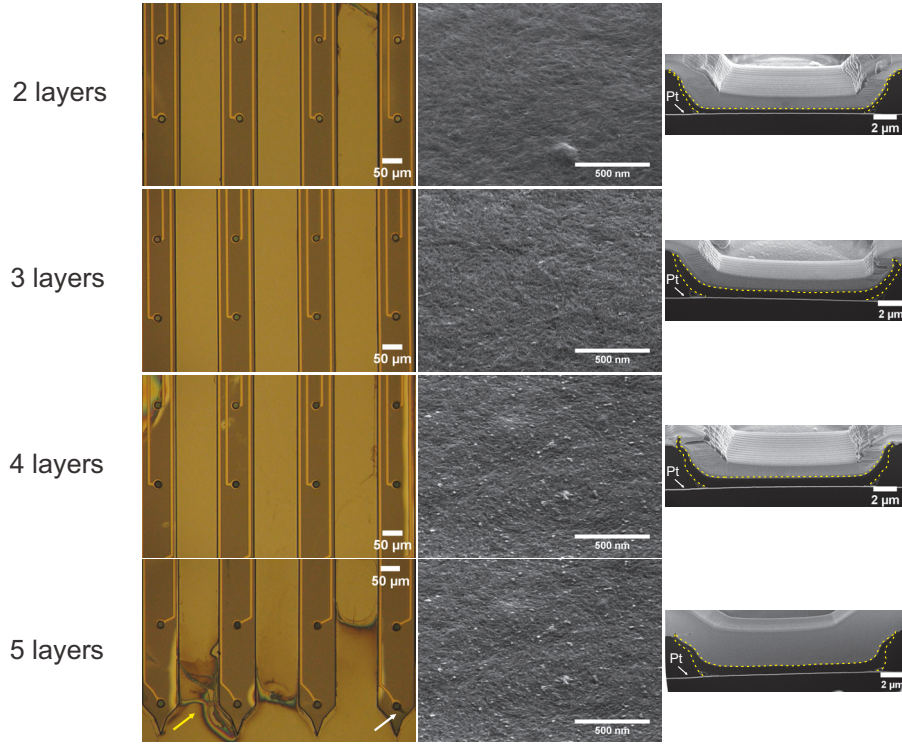
A.8.3. Spin-coated PEDOT:PSS

Figure A.8.: Optical images, SEM pictures and FIB sections of spin-coated PEDOT:PSS upon stacking of several layers. After dry releasing the PaC sacrificial layer, bluish residues were seen occasionally, especially around the shank tips (white arrows) and residues of the release soap solution were observed on top of the wafer around the probes (yellow arrow).
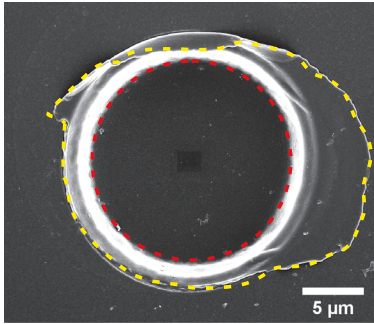
Figure A.9.: SEM image of the residues from the sacrificial layer around the electrode opening (dashed yellow line), which increased the ESA in contrast to the GSA (dashed red line).

A.8.4. Overview of electrochemical parameters

Electrode coating	Substrate	Area [μm^2]	Impedance (at 1 kHz) [$M\Omega \cdot \mu m^2$]	CSC [mC/cm^2]
	Pt [This work]	**113**	**744**	**1.14**
	Pt [259]	400	456	4.42 (cathodal)
	Pt [260]	491	491	
	Pt [172]	7854	400	1.4 (cathodal)
ECD [This work]	**Pt**	**113**	**4-6**	**10-50**
ECD [172]	Pt	7854	22	88.4 (cathodal)
ECD [143]	Au	1250	≈12.5	≈11
SC [This work]	**Pt**	**113**	**2-4**	**25-45**
SC [160]	Au	400	9.2	
SC [173]	Au	100	≈16	

Table A.2.: Overview of electrochemical parameters. Similar properties in regard to area of microelectrode, deposition/coating method, material of underlying conductive film and PEDOT:PSS formulation have been considered to find comparable works. ECD=Electrochemical deposition, SC=spin-coating.
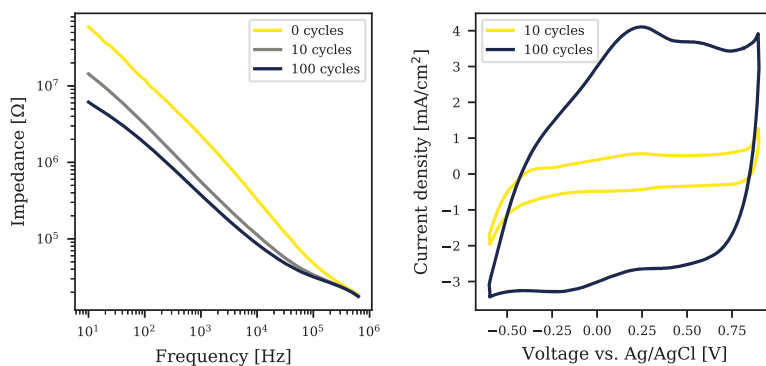
A.8.5. IrOx as adhesion promoter

Figure A.10.: Representative bode plots (left) and current over voltage curves (right) of SIROF. As a result to potential cycling defined as activation, the CSC increased and the impedance decreased.
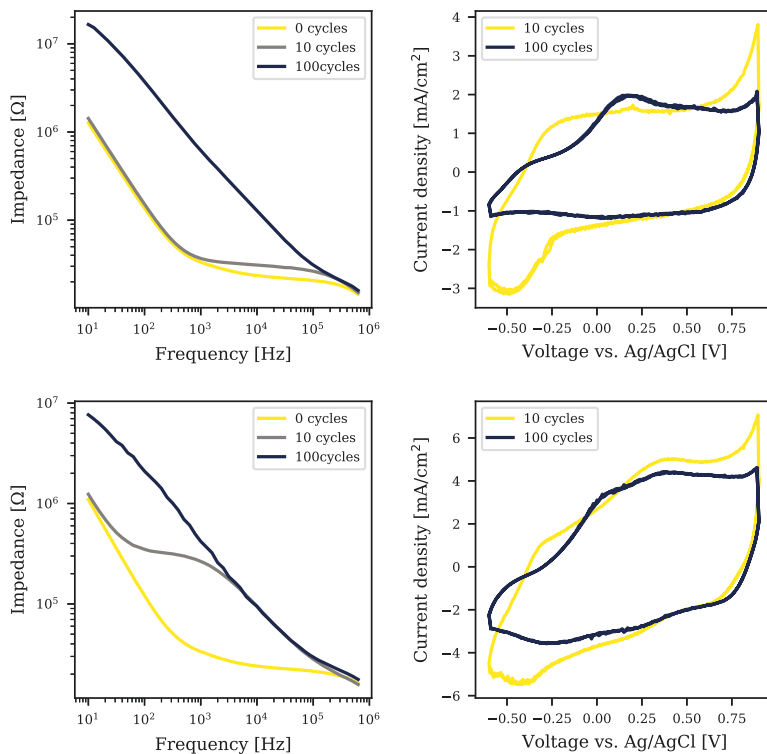
Figure A.11.: Representative bode plots (left) and current over voltage curves (right) of electrochemically deposited PEDOT:PSS on top of SIROF. A comparison is shown between native (top) and activated (bottom) IrOx.

A.9. PEG based insertion aid - Manual coating process

1. PDMS slap preparation:

   a) Use Sylgard 184 (Dow Corning, USA), a 2-component PDMS kit

   b) Thoroughly mix base and curing agent at a ratio 10:1 and degas at -20 °C for a couple of days to remove gas bubbles

   c) Dehydration of Si wafer at 150 °C for 5 min

   d) If necessary, Micro90 can be used as anti-adhesion layer to facilitate PDMS slap release:

      i. Spin-coating of Micro90 (2 % (v/v) in ultrapure water) (International products cooperation, USA): 1000 rpm, ramp rate 200 rpm/s, 20 s

      ii. Drying at RT for 5 min

   e) Spin-coating of PDMS mixture: 500 rpm, ramp rate 200 rpm/s, 60 s (120 µm)

   f) Soft baking at 110 °C for 10 min on hotplate

2. Cut PDMS base sheet ($\approx$4x4 mm^2), release with tweezer and place sheet on top of glass slide without trapping air bubbles

3. Carefully align probe soldered to PCB on top of PDMS base sheet

4. Straight alignment of shanks crucial (If not given, try to adjust with a tweezer without damaging the shanks.)

5. Fix PCB with tape on to glass slide

6. Cut PDMS mold by outlining the cavity: $\approx$4x4 mm^2 sheet with $\approx$0.8x0.8 mm^2 recess (Cavity determines width of PEG coating.)

7. Align PDMS mold on top of shank by covering first 200 µm from shank tip

8. Heat up probe and PDMS mold by placing entire assembly on the glass slide on a hotplate at 80 °C

9. Take a small granulate piece of PEG 35,000 g/mol (Sigma-Aldrich, Germany) with the aid of a tweezer and place on top of PDMS mold using a microscope

10. Wait until PEG melts and carefully distribute molten PEG over all four shanks

11. Repeat last two steps until cavity is completely filled with PEG

12. If necessary, cut PDMS cover sheet ($\approx$4x4 mm^2) and place on top of cavity to remove excess PEG

13. Let entire assembly cool down at RT for 5 min until PEG solidifies

14. Remove PDMS cover sheet and mold

15. Carefully release probe from PDMS base sheet by lifting the PCB
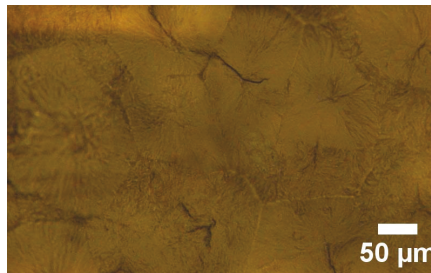
A.10. Crystallization of PEG

Figure A.12.: Solidification of PEG 35,000 g/mol by growing spherulites.

A.11. Agarose gel

A.11.1. Preparation of agarose gels

1. Weight 0.06 g agarose powder (A9539-256, Sigma Aldrich, Germany)

2. Add 10 ml PBS (137 mM NaCl, 2.7 mM KCl, 10 mM Na_2HPO_4 and 2 mM KH_2PO_4 prepared in ultrapure water and with a pH of 7.4 (Recipe from [72]))

3. Let sit for 1-2 min

4. Microwave on medium for 30 s

5. Swirl solution

6. Microwave on medium for 10 s

7. Swirl solution

8. Check for crystals and repeat last two steps until solution is homogenous

9. Avoid overboiling of solution

10. Prepare teflon mold by placing the pillow (1x1x0.5 cm^3) into cube (1x1x1 cm^3)

11. Pure solution into container

12. Allow to cool for $\approx$10 min and polymerize

13. Keep gels hydrated by covering with a few drops of PBS

14. For insertion tests, remove gel (1x1x0.5 cm^3) from mold (flip teflon mold and push pillow downwards) to have a free-standing phantom, which enables the imaging of the penetration
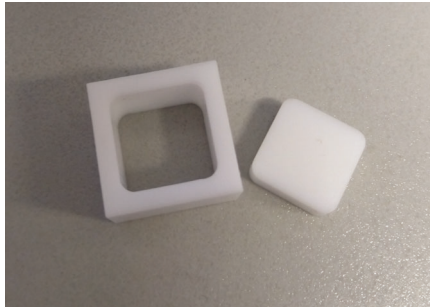
15. Use gels within 3 h

Figure A.13.: Telfon mold used to produce 0.6 % Agarose gel.

A.11.2. Mechanical characterization of agarose gels

Four 0.6 % agarose gels (see Section A.11.1) prepared at two different days were used to determine the Young's modulus. The measurements were performed at the Institute of Biological Information Processing 2 (IBI-2) of the Research Center Jülich. An AFM, Nanowizard (Bruker, Germany) in combination with an inverse light microscope (Axiovert 200, Zeiss, Germany) was used for the nanoindentation experiments. For the measurements, the agarose gels were covered with 0.1 M PBS. The identation was carried out at a velocity of 1-10 µm/s in spectroscopy mode. Several points for each gel were measured and each point was measured repeatedly. Silicon or silicon nitride cantilevers were used for the experiments with nominal spring constants of k = 0.06 N/m (NP, Veeco, Germany) and k = 0.04 N/m (Arrow TL, Nanoandmore, Germany), respectively. The tips of the cantilevers had a conical shape with an opening angle of 35°. For tipless cantilevers, polystyrol or glass beads (r=0.5 and 7.5 µm respective to the used cantilevers, Polyscience, Germany) were glued at the end. The actual spring constant was determined using thermal fluctuations in air [261] and the sensitivity was validated in PBS on glass. The data was analysed using the JPKSPM data processing Software

Nanowizard (Bruker, former JPK, Germany) and Origin 9G (Origin Lab). The force indentation depth curves were fitted to the extended Hertz model to obtain the Young's modulus assuming a Poisson ratio of 0.5 [262–265]. For determining the elastic modulus, the trace curves and the velocities 1-2 µm were considered.

A.12. PEG based insertion aid: Wafer-scale approach - PDMS mold

1. Use Sylgard 184 (Dow Corning, USA), a 2-component PDMS kit

2. Thoroughly mixing base and curing agent at a ratio 10:1 and degas at -20 °C for a couple of days to remove gas bubbles

3. Dehydration of Si wafer with flexible probes at 150 °C for 5 min

4. Sacrificial posts:

    a) Spin-coating of AZ 125nXT-10A (MicroChemicals, Germany): 300 rpm, ramp rate 100 rpm/s, 5 s; 900 rpm (145 µm) or 1000 rpm (95 µm), ramp rate 500 rpm/s, 1.2 s; 620 rpm, ramp rate 200 rpm/s, 12 s

    b) Perform edge bead removal

    c) Resting wafer for 15 min

    d) Soft-baking using a temperature ramp: from 20-135 °C in 30 °C/min, hold at 135 °C for 25 min, from 135-20 °C in 30 °C/min

    e) UV exposure: 2400-2500 mJ/cm² (soft contact)

    f) Development in AZ MIF 326 (MicroChemicals, Germany) for 5 min

    g) Removing residues from wafer edge using cotton stick and acetone

5. PDMS deposition:

    a) Release layer: Spin-coating of Micro 90 (2 % (v/v) in ultrapure water): 1000 rpm, ramp rate 200 rpm/s, 20 s and Drying at RT for 5 min

    b) Spin-coating of PDMS mixture: 1000 rpm (75 µm) or 500 rpm (120 µm), ramp rate 200 rpm/s, 60 s

    c) Resting wafer for 30 min

    d) Soft baking at 110 °C for 10 min on hotplate

6. Dry etching and lift-off:

a) CF_4:O_2, 45:3 sccm, 0.007 mbar, RF 100 W, ICP 500 W, 10 °C, 30 min with 0.5 µm/min (Oxford Plasma Technology RIE reactor, United Kingdom)

b) Stripping of sacrificial posts resist in acetone for 10 min using ultrasonication and rinsing with isopropyl alcohol

A.13. Type of intracortical implants

	A-MEA-16	Retinal probe	ATLAS probe
Insulation material	PaC	Si	Si
Number of shanks	4	4	1
Shank thickness [µm]	10	10-20	50
Shank width [µm]	100	100	75
Shank length [mm]	2	1	6
Inter-shank distance [µm]	100	150	
Electrodes per shank [µm]	4	3	16
Electrode pitch [µm]	200	20	100
Electrode area [µm^2]	113	800-1600	491
Electrode coating	PEDOT:PSS	IrOx	IrOx
Electrode impedance [MΩ·µm^2]	3.06±0.15	2.06±0.44	112.93±4.91
Tip angle [°]	30-40	50-60	

Table A.3.: The critical dimensions and properties of the neural probes used within this work are provided. The ATLAS probe E16+R-100-S1-L6 NT was used. The impedances at 1 Hz are given and were averaged for one single probe. Microelectrodes with an impedance above 10 MΩ·µm^2 at 1 kHz were excluded as outliers.

References

[1] F. A. Azevedo, L. R. Carvalho, L. T. Grinberg, J. M. Farfel, R. E. Ferretti, R. E. Leite, W. J. Filho, R. Lent, and S. Herculano-Houzel, "Equal numbers of neuronal and nonneuronal cells make the human brain an isometrically scaled-up primate brain," *Journal of Comparative Neurology*, vol. 513, no. 5, pp. 532–541, 2009.

[2] Collaborators GBD 2016 Neurology, "Global, regional, and national burden of neurological disorders, 1990–2016: a systematic analysis for the Global Burden of Disease Study 2016," *The Lancet Neurology*, vol. 18, no. 5, pp. 459–480, 2019.

[3] G. E. Loeb, "Neural Prosthetics: A Review of Empirical vs. Systems Engineering Strategies," *Applied Bionics and Biomechanics*, 2018.

[4] M. Jorfi, J. L. Skousen, C. Weder, and J. R. Capadona, "Progress towards biocompatible intracortical microelectrodes for neural interfacing applications," *Journal of Neural Engineering*, vol. 12, no. 1, pp. 1304–1314, 2015.

[5] K. M. Szostak, L. Grand, and T. G. Constandinou, "Neural interfaces for intracortical recording: Requirements, fabrication methods, and characteristics," *Frontiers in Neuroscience*, vol. 11, 2017.

[6] A. Weltman, J. Yoo, and E. Meng, "Flexible, penetrating brain probes enabled by advances in polymer microfabrication," *Micromachines*, vol. 7, no. 10, 2016.

[7] A. Lecomte, E. Descamps, and C. Bergaud, "A review on mechanical considerations for chronically-implanted neural probes," *Journal of Neural Engineering*, vol. 15, no. 3, 2018.

[8] Z. Aqrawe, J. Montgomery, J. Travas-Sejdic, and D. Svirskis, "Conducting polymers for neuronal microelectrode array recording and stimulation," *Sensors and Actuators B: Chemical*, vol. 257, pp. 753–765, 2018.

[9] F. Blair Simmons, J. M. Epley, R. C. Lummis, N. Guttman, L. S. Frishkopf, L. D. Harmon, and E. Zwicker, "Auditory nerve: Electrical stimulation in man," *Science*, vol. 148, no. 3666, pp. 104–106, 1965.

References

[10] K. Stingl, K. U. Bartz-Schmidt, D. Besch, A. Braun, A. Bruckmann, F. Gekeler, U. Greppmaier, S. Hipp, G. Hortdorfer, C. Kernstock, A. Koitschev, A. Kusnyerik, H. Sachs, A. Schatz, K. T. Stingl, T. Peters, B. Wilhelm, and E. Zrenner, "Artificial vision with wirelessly powered subretinal electronic implant alpha-IMS," *Proceedings of the Royal Society B: Biological Sciences*, vol. 280, no. 1757, pp. 1–8, 2013.

[11] E. Bloch and L. da Cruz, "The Argus II Retinal Prosthesis System," *IntechOpen*, 2019.

[12] J. K. Krauss, N. Lipsman, T. Aziz, A. Boutet, P. Brown, J. W. Chang, B. Davidson, W. M. Grill, M. I. Hariz, A. Horn, M. Schulder, A. Mammis, P. A. Tass, J. Volkmann, and A. M. Lozano, "Technology of deep brain stimulation: current status and future directions," *Nature Reviews Neurology*, vol. 17, 2020.

[13] D. F. Williams, "On the mechanisms of biocompatibility," *Biomaterials*, vol. 29, no. 20, pp. 2941–2953, 2008.

[14] R. Biran, D. C. Martin, and P. A. Tresco, "Neuronal cell loss accompanies the brain tissue response to chronically implanted silicon microelectrode arrays," *Experimental Neurology*, vol. 195, no. 1, pp. 115–126, 2005.

[15] J. K. Nguyen, D. J. Park, J. L. Skousen, A. E. Hess-Dunning, D. J. Tyler, S. J. Rowan, C. Weder, and J. R. Capadona, "Mechanically-compliant intracortical implants reduce the neuroinflammatory response," *Journal of Neural Engineering*, vol. 11, no. 5, 2014.

[16] D. Prodanov and J. Delbeke, "Mechanical and biological interactions of implants with the brain and their impact on implant design," *Frontiers in Neuroscience*, vol. 10, 2016.

[17] A. Prasad, Q. S. Xue, R. Dieme, V. Sankar, R. C. Mayrand, T. Nishida, W. J. Streit, and J. C. Sanchez, "Abiotic-biotic characterization of Pt/Ir microelectrode arrays in chronic implants," *Frontiers in Neuroengineering*, vol. 7, pp. 1–15, 2014.

[18] P. Takmakov, K. Ruda, K. Scott Phillips, I. S. Isayeva, V. Krauthamer, and C. G. Welle, "Rapid evaluation of the durability of cortical neural implants using accelerated aging with reactive oxygen species," *Journal of Neural Engineering*, vol. 12, 2015.

[19] J. C. Barrese, N. Rao, K. Paroo, C. Triebwasser, C. Vargas-Irwin, L. Franquemont, and J. P. Donoghue, "Failure mode analysis of silicon-based intracortical microelectrode arrays in non-human primates," *Journal of Neural Engineering*, vol. 10, no. 6, 2013.

[20] V. Lindroos, S. Franssila, M. Tilli, M. Paulasto-Krockel, A. Lehto, T. Motooka, and V.-M. Airaksinen, "Silicon as MEMS material," in *Handbook of Silicon Based MEMS Materials and Technologies: Second Edition*, Elsevier, 2009.

[21] H. S. Sohal, G. J. Clowry, A. Jackson, A. O'Neill, and S. N. Baker, "Mechanical flexibility reduces the foreign body response to long-term implanted microelectrodes in rabbit cortex," *PLoS ONE*, vol. 11, no. 10, pp. 1–15, 2016.

[22] S. Felix, K. Shah, D. George, V. Tolosa, A. Tooker, H. Sheth, T. Delima, and S. Pannu, "Removable silicon insertion stiffeners for neural probes using polyethylene glycol as a biodissolvable adhesive," *Proceedings of the Annual International Conference of the IEEE Engineering in Medicine and Biology Society, EMBS*, pp. 871–874, 2012.

[23] A. Lecomte, V. Castagnola, E. Descamps, L. Dahan, M. C. Blatché, T. M. Dinis, E. Leclerc, C. Egles, and C. Bergaud, "Silk and PEG as means to stiffen a parylene probe for insertion in the brain: Toward a double time-scale tool for local drug delivery," *Journal of Micromechanics and Microengineering*, 2015.

[24] N. Obidin, F. Tasnim, and C. Dagdeviren, "The Future of Neuroimplantable Devices: A Materials Science and Regulatory Perspective," *Advanced Materials*, vol. 32, no. 15, 2019.

[25] R. Biran, D. C. Martin, and P. A. Tresco, "The brain tissue response to implanted silicon microelectrode arrays is increased when the device is tethered to the skull," *Journal of Biomedical Materials Research*, vol. 82A, no. 1, pp. 169–178, 2007.

[26] A. Sridharan, S. D. Rajan, and J. Muthuswamy, "Long-term changes in the material properties of brain tissue at the implant-tissue interface," *Journal of Neural Engineering*, vol. 10, no. 6, 2013.

[27] A. Lecomte, A. Degache, E. Descamps, L. Dahan, and C. Bergaud, "In vitro and in vivo biostability assessment of chronically-implanted Parylene C neural sensors," *Sensors and Actuators, B: Chemical*, vol. 251, pp. 1001–1008, 2017.

[28] J. T. Kuo, B. J. Kim, S. a. Hara, C. D. Lee, C. a. Gutierrez, T. Q. Hoang, and E. Meng, "Novel flexible Parylene neural probe with 3D sheath structure for enhancing tissue integration," *Lab Chip*, vol. 13, no. 4, pp. 554–561, 2013.

[29] J. M. H. Morales and C. Clément, "Technical Challenges of Active Implantable Medical Devices for Neurotechnology," *IEEE CPMT Symposium Japan (ICSJ)*, pp. 77–80, 2018.

[30] F. Kohler, C. A. Gkogkidis, C. Bentler, X. Wang, M. Gierthmuehlen, J. Fischer, C. Stolle, L. M. Reindl, J. Rickert, T. Stieglitz, T. Ball, and

References

M. Schuettler, "Closed-loop interaction with the cerebral cortex: a review of wireless implant technology," *Brain-Computer Interfaces*, vol. 4, no. 3, pp. 146–154, 2017.

[31] M. E. J. Obien, K. Deligkaris, T. Bullmann, D. J. Bakkum, and U. Frey, "Revealing neuronal function through microelectrode array recordings," *Frontiers in Neuroscience*, vol. 8, 2015.

[32] J. J. Jun, N. A. Steinmetz, J. H. Siegle, D. J. Denman, M. Bauza, B. Barbarits, A. K. Lee, C. A. Anastassiou, A. Andrei, Ç. Aydin, M. Barbic, T. J. Blanche, V. Bonin, J. Couto, B. Dutta, S. L. Gratiy, D. A. Gutnisky, M. Häusser, B. Karsh, P. Ledochowitsch, C. M. Lopez, C. Mitelut, S. Musa, M. Okun, M. Pachitariu, J. Putzeys, P. D. Rich, C. Rossant, W. L. Sun, K. Svoboda, M. Carandini, K. D. Harris, C. Koch, J. O'Keefe, and T. D. Harris, "Fully integrated silicon probes for high-density recording of neural activity," *Nature*, vol. 551, no. 7679, pp. 232–236, 2017.

[33] M. A. Nicolelis, D. Dimitrov, J. M. Carmena, R. Crist, G. Lehew, J. D. Kralik, and S. P. Wise, "Chronic, multisite, multielectrode recordings in macaque monkeys," *Proceedings of the National Academy of Sciences of the United States of America*, vol. 100, no. 19, pp. 11041–11046, 2003.

[34] J. Krüger, F. Caruana, R. D. Volta, and G. Rizzolatti, "Seven years of recording from monkey cortex with a chronically implanted multiple microelectrode," *Frontiers in Neuroengineering*, vol. 3, no. MAY, pp. 1–9, 2010.

[35] M. Y. Cheng, M. Je, K. L. Tan, E. L. Tan, R. Lim, L. Yao, P. Li, W. T. Park, E. J. R. Phua, C. L. Gan, and A. Yu, "A low-profile three-dimensional neural probe array using a silicon lead transfer structure," *Journal of Micromechanics and Microengineering*, vol. 23, no. 9, 2013.

[36] J. John, Y. Li, J. Zhang, J. A. Loeb, and Y. Xu, "Microfabrication of 3D neural probes with combined electrical and chemical interfaces," *Journal of Micromechanics and Microengineering*, vol. 21, no. 10, 2011.

[37] D. R. Kipke, R. J. Vetter, J. C. Williams, and J. F. Hetke, "Silicon-substrate intracortical microelectrode arrays for long-term recording of neuronal spike activity in cerebral cortex," *IEEE Transactions on Neural Systems and Rehabilitation Engineering*, vol. 11, no. 2, pp. 151–155, 2003.

[38] R. J. Vetter, J. C. Williams, J. F. Hetke, E. A. Nunamaker, and D. R. Kipke, "Chronic neural recording using silicon-substrate microelectrode arrays implanted in cerebral cortex," *IEEE Transactions on Biomedical Engineering*, vol. 51, no. 6, pp. 896–904, 2004.

References

[39] S. Suner, M. R. Fellows, C. Vargas-Irwin, G. K. Nakata, and J. P. Donoghue, "Reliability of signals from a chronically implanted, silicon-based electrode array in non-human primate primary motor cortex," *IEEE Transactions on Neural Systems and Rehabilitation Engineering*, vol. 13, no. 4, pp. 524–541, 2005.

[40] J. D. Simeral, S. P. Kim, M. J. Black, J. P. Donoghue, and L. R. Hochberg, "Neural control of cursor trajectory and click by a human with tetraplegia 1000 days after implant of an intracortical microelectrode array," *Journal of Neural Engineering*, vol. 8, no. 2, 2011.

[41] S. P. Lacour, G. Courtine, and J. Guck, "Materials and technologies for soft implantable neuroprostheses," *Nature Reviews Materials*, vol. 1, no. 10, 2016.

[42] J. Subbaroyan, D. C. Martin, and D. R. Kipke, "A finite-element model of the mechanical effects of implantable microelectrodes in the cerebral cortex," *Journal of Neural Engineering*, vol. 2, no. 4, pp. 103–113, 2005.

[43] F. Deku, C. L. Frewin, A. Stiller, Y. Cohen, S. Aqeel, A. Joshi-Imre, B. Black, T. J. Gardner, J. J. Pancrazio, and S. F. Cogan, "Amorphous silicon carbide platform for next generation penetrating neural interface designs," *Micromachines*, vol. 9, no. 10, 2018.

[44] B. J. Kim, J. T. Kuo, S. A. Hara, C. D. Lee, L. Yu, C. A. Gutierrez, T. Q. Hoang, V. Pikov, and E. Meng, "3D Parylene sheath neural probe for chronic recordings," *Journal of Neural Engineering*, vol. 10, 2013.

[45] H. Xu, A. W. Hirschberg, K. Scholten, T. W. Berger, D. Song, and E. Meng, "Acute in vivo testing of a conformal polymer microelectrode array for multi-region hippocampal recordings," *Journal of Neural Engineering*, vol. 15, no. 1, 2018.

[46] Z. Xiang, S.-C. C. Yen, N. Xue, T. Sun, W. M. Tsang, S. Zhang, L.-D. D. Liao, N. V. Thakor, and C. Lee, "Ultra-thin flexible polyimide neural probe embedded in a dissolvable maltose-coated microneedle," *Journal of Micromechanics and Microengineering*, vol. 24, no. 6, 2014.

[47] R. J. Van Daal, J. J. Sun, F. Ceyssens, F. Michon, M. Kraft, R. Puers, and F. Kloosterman, "System for recording from multiple flexible polyimide neural probes in freely behaving animals," *Journal of Neural Engineering*, vol. 17, no. 1, 2020.

[48] X. Wei, L. Luan, Z. Zhao, X. Li, H. Zhu, O. Potnis, and C. Xie, "Nanofabricated Ultraflexible Electrode Arrays for High-Density Intracortical Recording," *Advanced Science*, vol. 5, no. 6, pp. 1–9, 2018.

[49] L. Luan, X. Wei, Z. Zhao, J. J. Siegel, O. Potnis, C. a. Tuppen, S. Lin, S. Kazmi, R. a. Fowler, S. Holloway, A. K. Dunn, R. a. Chitwood, and

C. Xie, "Ultraflexible nanoelectronic probes form reliable, glial scar–free neural integration," *Science Advances*, vol. 3, no. 2, pp. 1–10, 2017.

[50] J. E. Chung, H. R. Joo, J. L. Fan, D. F. Liu, A. H. Barnett, S. Chen, C. Geaghan-Breiner, M. P. Karlsson, M. Karlsson, K. Y. Lee, H. Liang, J. F. Magland, J. A. Pebbles, A. C. Tooker, L. F. Greengard, V. M. Tolosa, and L. M. Frank, "High-Density, Long-Lasting, and Multi-region Electrophysiological Recordings Using Polymer Electrode Arrays," *Neuron*, vol. 101, no. 1, pp. 21–31, 2019.

[51] N. Campbell and J. Reece, *Biology*. Benjamin-Cummings Pub Co, 2002.

[52] W. H. Goldmann, "Mechanical aspects of cell shape regulation and signaling," *Cell Biology International*, vol. 26, no. 4, pp. 313–317, 2002.

[53] D. J. Aidley, "The Physiology of Excitable Cells. Cambridge University," *Press*, 1998.

[54] S. I. Amari, "Neural mechanisms of information processing in the brain," *Systems and Computers in Japan*, vol. 18, no. 7, pp. 31–45, 1987.

[55] E. R. Kandel and J. H. Schwartz, *Principles of neural science*. McGraw-Hill New York, 2000.

[56] A. L. Hodgkin and A. F. Huxley, "A quantitaive description of membrane current and its application to conduction and excitation in nerve," *Journal of Physiology*, vol. 117, pp. 500–544, 1952.

[57] J. P. Donoghue, "Bridging the Brain to the World: A Perspective on Neural Interface Systems," *Neuron*, vol. 60, no. 3, pp. 511–521, 2008.

[58] G. Buzsáki, C. A. Anastassiou, and C. Koch, "The origin of extracellular fields and currents-EEG, ECoG, LFP and spikes," *Nature Reviews Neuroscience*, vol. 13, no. 6, pp. 407–420, 2012.

[59] J. M. Carmena, M. A. Lebedev, C. S. Henriquez, and M. A. Nicolelis, "Stable ensemble performance with single-neuron variability during reaching movements in primates," *Journal of Neuroscience*, vol. 25, no. 46, pp. 10712–10716, 2005.

[60] L. R. Hochberg, M. D. Serruya, G. M. Friehs, J. A. Mukand, M. Saleh, A. H. Caplan, A. Branner, D. Chen, R. D. Penn, and J. P. Donoghue, "Neuronal ensemble control of prosthetic devices by a human with tetraplegia," *Nature*, vol. 442, no. 7099, pp. 164–171, 2006.

[61] A. Belitski, A. Gretton, C. Magri, Y. Murayama, M. A. Montemurro, N. K. Logothetis, and S. Panzeri, "Low-frequency local field potentials and spikes in primary visual cortex convey independent visual information," *Journal of Neuroscience*, vol. 28, no. 22, pp. 5696–5709, 2008.

[62] G. Hong and C. M. Lieber, "Novel electrode technologies for neural recordings," *Nature Reviews Neuroscience*, vol. 20, no. 6, pp. 330–345, 2019.

[63] C. A. Thomas, P. A. Springer, G. E. Loeb, Y. Berwald-Netter, and L. M. Okun, "A miniature microelectrode array to monitor the bioelectric activity of cultured cells," *Experimental Cell Research*, vol. 74, no. 1, pp. 61–66, 1972.

[64] G. W. Gross, "Simultaneous Single Unit Recording in vitro with a Photoetched Laser Deinsulated Gold Multimicroelectrode Surface," *IEEE Transactions on Biomedical Engineering*, vol. BME-26, no. 5, pp. 273–279, 1979.

[65] J. Pine, "Recording action potentials from cultured neurons with extracellular microcircuit electrodes," *Journal of Neuroscience Methods*, vol. 2, pp. 19–31, feb 1980.

[66] J. P. Seymour, F. Wu, K. D. Wise, and E. Yoon, "State-of-the-art MEMS and microsystem tools for brain research," *Microsystems and Nanoengineering*, vol. 3, no. March 2016, pp. 1–16, 2017.

[67] A. J. Bard and L. R. Faulkner, *Electrochemical Methods, Fundamentals and Applications*. John Wiley & Sons, Inc., 2nd ed., 2001.

[68] R. Weis and P. Fromherz, "Frequency dependent signal transfer in neuron transistors," *Physical Review E - Statistical Physics, Plasmas, Fluids, and Related Interdisciplinary Topics*, vol. 55, no. 1, pp. 877–889, 1997.

[69] P. Massobrio, G. Massobrio, and S. Martinoia, "Interfacing cultured neurons to microtransducers arrays: A review of the neuro-electronic junction models," *Frontiers in Neuroscience*, vol. 10, pp. 1–13, jun 2016.

[70] J. Randles, "Kinetics of rapid electrode reactions," *Discuss. Faraday Soc.*, pp. 11–19, 1947.

[71] W. Franks, I. Schenker, P. Schmutz, and A. Hierlemann, "Impedance characterization and modeling of electrodes for biomedical applications," *IEEE Transactions on Biomedical Engineering*, vol. 52, no. 7, pp. 1295–1302, 2005.

[72] J. Sambrook and D. W. Russell, *Molecular Cloning: A Laboratory Manual, Volume 3*. Cold Spring Habor Laboratory Press, 2001.

[73] F. Scholz, *Electroanalytical Methods*. Springer-Verlag Berlin Heidelberg, 2nd ed., 2010.

[74] J. S. Brusius, *3-Dimensionale Penetrierende Multi-elektrodenarrays zur Stimulation und Ableitung in der Retina*. PhD thesis, 2015.

References

[75] V. Maybeck, J. Schnitker, W. Li, M. O. Heuschkel, and A. Offenhäusser, "An Evaluation of Extracellular MEA vs. Optogenetic Stimulation of Cortical Neurons," *Biomedical Physics & Engineering Express*, vol. 2, no. 5, 2016.

[76] G. van Rossum, "Python Library Reference (CWI Report CS-R9524)," 1995.

[77] D. N. Hill, S. B. Mehta, and D. Kleinfeld, "Quality metrics to accompany spike sorting of extracellular signals," *Journal of Neuroscience*, vol. 31, no. 24, pp. 8699–8705, 2011.

[78] J. J. DiCarlo, J. W. Lane, S. S. Hsiao, and K. O. Johnson, "Marking microelectrode penetrations with fluorescent dyes," *Journal of Neuroscience Methods*, vol. 64, no. 1, pp. 75–81, 1996.

[79] P. J. Rousche, D. S. Pellinen, D. P. Pivin, J. C. Williams, R. J. Vetter, and D. R. Kipke, "Flexible polyimide-based intracortical electrode arrays with bioactive capability," *IEEE Transactions on Biomedical Engineering*, vol. 48, no. 3, pp. 361–370, 2001.

[80] A. M. Stiller, B. J. Black, C. Kung, A. Ashok, S. F. Cogan, V. D. Varner, and J. J. Pancrazio, "A meta-analysis of intracortical device stiffness and its correlation with histological outcomes," *Micromachines*, vol. 9, no. 9, 2018.

[81] Nusil Silicone Technology, "MED-1000 Silicone adhesive - Technical Data Sheet," 2018.

[82] Z. Wang, A. A. Volinsky, and N. D. Gallant, "Crosslinking effect on polydimethylsiloxane elastic modulus measured by custom-built compression instrument," *Journal of Applied Polymer Science*, vol. 131, no. 22, pp. 1–4, 2014.

[83] M. J. Madou, *Fundamentals of Microfabrication: The Science of Miniaturization.* CRC Press, 2002.

[84] T. H. Thomas and T. C. Kendrick, "Thermal analysis of polydimethylsiloxanes. I. Thermal degradation in controlled atmospheres," *Journal of Polymer Science Part A-2: Polymer Physics*, vol. 7, no. 3, pp. 537–549, 1969.

[85] J. Ortigoza-Diaz, K. Scholten, C. Larson, A. Cobo, T. Hudson, J. Yoo, A. Baldwin, A. W. Hirschberg, and E. Meng, "Techniques and considerations in the microfabrication of parylene C microelectromechanical systems," *Micromachines*, vol. 9, no. 9, 2018.

[86] R. a. Nawrocki, H. Jin, S. Lee, T. Yokota, M. Sekino, and T. Someya, "Self-Adhesive and Ultra-Conformable, Sub-300 nm Dry Thin-Film Electrodes for Surface Monitoring of Biopotentials," *Advanced Functional Materials*, vol. 28, no. 36, pp. 1–11, 2018.

[87] C. Hassler, T. Boretius, and T. Stieglitz, "Polymers for neural implants," *Journal of Polymer Science, Part B: Polymer Physics*, vol. 49, no. 1, pp. 18–33, 2011.

[88] Specialty Coating Systems, "SCS Parylene Properties - Technical Data Sheet," 2018.

[89] The Dow Chemical Company, "SYLGARD™ 184 Silicone Elastomer - Technical Data Sheet," 2017.

[90] V. Castagnola, E. Descamps, A. Lecestre, L. Dahan, J. Remaud, L. G. Nowak, and C. Bergaud, "Parylene-based flexible neural probes with PEDOT coated surface for brain stimulation and recording," *Biosensors and Bioelectronics*, vol. 67, pp. 450–457, 2015.

[91] J. M. Kim, D. R. Oh, J. Sanchez, S. H. Kim, and J. M. Seo, "Fabrication of polydimethylsiloxane (PDMS) - Based multielectrode array for neural interface," *Proceedings of the Annual International Conference of the IEEE Engineering in Medicine and Biology Society, EMBS*, pp. 1716–1719, 2013.

[92] Z. Xiang, H. Wang, S. Zhang, S. C. Yen, M. Je, W. M. Tsang, Y. P. Xu, N. V. Thakor, D. L. Kwong, and C. Lee, "Development of flexible neural probes using SU-8/parylene," *8th Annual IEEE International Conference on Nano/Micro Engineered and Molecular Systems*, vol. 1, pp. 1076–1079, 2013.

[93] S. E. Lee, S. B. Jun, H. J. Lee, J. Kim, S. W. Lee, C. Im, H. C. Shin, J. W. Chang, and S. J. Kim, "A flexible depth probe using liquid crystal polymer," *IEEE Transactions on Biomedical Engineering*, vol. 59, no. 7, pp. 2085–2094, 2012.

[94] K. Lee, S. Massia, and J. He, "Biocompatible benzocyclobutene-based intracortical neural implant with surface modification," *Journal of Micromechanics and Microengineering*, vol. 15, no. 11, pp. 2149–2155, 2005.

[95] J. Charmet, J. Bitterli, O. Sereda, M. Liley, P. Renaud, and H. Keppner, "Optimizing parylene C adhesion for MEMS processes: Potassium hydroxide wet etching," *Journal of Microelectromechanical Systems*, vol. 22, no. 4, pp. 855–864, 2013.

[96] C. Hassler, R. P. Von Metzen, P. Ruther, and T. Stieglitz, "Characterization of parylene C as an encapsulation material for implanted neural prostheses," *Journal of Biomedical Materials Research - Part B Applied Biomaterials*, vol. 93, no. 1, pp. 266–274, 2010.

[97] Specialty Coating Systems, "SCS A-174 - Material Safety data sheet," 2013.

[98] A. J. Blake, T. M. Pearce, N. S. Rao, S. M. Johnson, and J. C. Williams, "Multilayer PDMS microfluidic chamber for controlling brain slice

microenvironment," *Lab on a Chip*, vol. 7, no. 7, pp. 842–849, 2007.

[99] Y. Hwang, O. H. Paydar, and R. N. Candler, "3D printed molds for non-planar PDMS microfluidic channels," *Sensors and Actuators A: Physical*, vol. 226, pp. 137–142, 2015.

[100] J. H. Lin, Y. Wang, X. M. Wu, T. L. Ren, and L. T. Liu, "Implantable subdural electrode arrays for neural recordings based on MEMS technologies," *Proceedings of the 2nd International Conference on Biomedical Engineering and Informatics*, 2009.

[101] M. Ochoa, P. Wei, A. J. Wolley, K. J. Otto, and B. Ziaie, "A Hybrid PDMS-Parylene Subdural Multi-Electrode Array," *Biomedical Microdevices*, vol. 15, no. 3, pp. 437–443, 2013.

[102] I. D. Johnston, D. K. McCluskey, C. K. Tan, and M. C. Tracey, "Mechanical characterization of bulk Sylgard 184 for microfluidics and microengineering," *Journal of Micromechanics and Microengineering*, vol. 24, no. 3, 2014.

[103] J. N. Patel, B. Kaminska, B. L. Gray, and B. D. Gates, "A sacrificial SU-8 mask for direct metallization on PDMS," *Journal of Micromechanics and Microengineering*, vol. 19, no. 11, 2009.

[104] L. Guo, W. K. Meacham, S. Hochman, and S. P. DeWeerth, "A PDMS-Based Conical-Well Microelectrode Array for Surface Stimulation and Recording of Neural Tissues," *IEEE transactions on bio-medical engineering*, vol. 57, no. 10, pp. 2485–2494, 2010.

[105] B. K. Sarkar, *Strength of materials.* Tata McGraw-Hill, 2003.

[106] W. Jensen, K. Yoshida, and U. G. Hofmann, "In-vivo implant mechanics of flexible, silicon-based ACREO microelectrode arrays in rat cerebral cortex," *IEEE Transactions on Biomedical Engineering*, vol. 53, no. 5, pp. 934–940, 2006.

[107] A. M. Obaid, Y.-W. Wu, M.-E. Hanna, W. D. Nix, J. B. Ding, and N. a. Melosh, "Ultra-sensitive measurement of brain penetration with microscale probes for brain machine interface considerations," *bioRxiv*, 2018.

[108] A. H. Dunning and D. J. Tyler, "A Mechanically-Adaptive Polymer Nanocomposite-Based Intracortical Probe and Package for Chronic Neural Recording," *Micromachines*, vol. 9, no. 583, pp. 1–16, 2018.

[109] J. Agorelius, F. Tsanakalis, A. Friberg, P. T. Thorbergsson, L. M. E. Pettersson, and J. Schouenborg, "An array of highly flexible electrodes with a tailored configuration locked by gelatin during implantation-initial evaluation in cortex cerebri of awake rats," *Frontiers in Neuroscience*, vol. 9, pp. 1–12, 2015.

[110] J. W. Judy, "Microelectromechanical systems (MEMS): Fabrication, design and applications," *Smart Materials and Structures*, vol. 10, no. 6, pp. 1115–1134, 2001.

[111] A. Folch, *Introduction to BioMEMS*. CRC Press, Taylor & Francis Group, 2013.

[112] R. Luttge, *Microfabrication for Industrial Applications - Chapter 2 : Basic Technologies for Microsystems*. William Andrew, 2011.

[113] E. Liston, L. Martinu, and M. Wertheimer, "Plasma surface modification of polymers for improved adhesion: a critical review," *Journal of Adhesion Science and Technology*, vol. 7, no. 10, pp. 1091–1127, 1993.

[114] M. Nordström, A. Johansson, E. S. Noguerón, B. Clausen, M. Calleja, and A. Boisen, "Investigation of the bond strength between the photo-sensitive polymer SU-8 and gold," *Microelectronic Engineering*, vol. 78-79, no. 1-4, pp. 152–157, 2005.

[115] S. Franssila and L. Sainiemi, "Reactive Ion Etching (RIE)," in *Encyclopedia of Microfluidics and Nanofluidics* (D. Li, ed.), pp. 1790–1790, Boston, MA: Springer US, 2008.

[116] T. Adrega and S. P. Lacour, "Stretchable gold conductors embedded in PDMS and patterned by photolithography: Fabrication and electromechanical characterization," *Journal of Micromechanics and Microengineering*, vol. 20, 2010.

[117] M. A. Lieberman and A. J. Lichtenberg, *Principles of Plasma Discharges and Materials Processing*. A John Wiley & Sons, INC Publication, 2nd ed., 2005.

[118] E. Meng, P. Y. Li, and Y. C. Tai, "Plasma removal of Parylene C," *Journal of Micromechanics and Microengineering*, vol. 18, no. 4, 2008.

[119] A. Lecomte, A. Lecestre, D. Bourrier, M. C. Blatché, L. Jalabert, E. Descamps, and C. Bergaud, "Deep plasma etching of Parylene C patterns for biomedical applications," *Microelectronic Engineering*, vol. 177, pp. 70–73, 2017.

[120] J.-M. Kim and J. M. Seo, "Fabrication of Polydimethylsiloxane (PDMS) -Based Flexible Electrode Array for Improving Tissue Contact," *IFMBE Proceedings*, vol. 45, pp. 363–366, 2015.

[121] W. Chen, R. H. W. Lam, and J. Fu, "Photolithographic surface micromachining of polydimethylsiloxane (PDMS)," *Lab on a Chip*, vol. 12, no. 2, pp. 391–395, 2012.

[122] T. Trantidou, T. Prodromakis, and C. Toumazou, "Oxygen plasma induced hydrophilicity of Parylene-C thin films," *Applied Surface Science*, vol. 261,

pp. 43–51, 2012.

[123] J. Ortigoza-Diaz, K. Scholten, and E. Meng, "Characterization and Modification of Adhesion in Dry and Wet Environments in Thin-Film Parylene Systems," *Journal of Microelectromechanical Systems*, vol. 27, no. 5, pp. 874–885, 2018.

[124] X. Wang, A. W. Hirschberg, H. Xu, Z. Slingsby-Smith, A. Lecomte, K. Scholten, D. Song, and E. Meng, "A Parylene Neural Probe Array for Multi-Region Deep Brain Recordings," *Journal of Microelectromechanical Systems*, vol. 29, no. 4, pp. 499–513, 2020.

[125] O. Graudejus, P. Görrn, and S. Wagner, "Controlling the morphology of gold films on poly(dimethylsiloxane)," *ACS Applied Materials and Interfaces*, vol. 2, no. 7, pp. 1927–1933, 2010.

[126] D. Zeniieh, A. Bajwa, F. Olcaytug, and G. Urban, "Parylene-C Thin Film for Biocompatible Encapsulations With Very Strong Adhesion and Superior Barrier Properties," *21st International Symposium on Plasma Chemistry*, pp. 1–4, 2013.

[127] G. Buzsáki, A. Berényi, E. Stark, K. D. Wise, E. Yoon, D. Khodagholy, and D. R. Kipke, "Tools for Probing Local Circuits: High-Density Silicon Probes Combined with Optogenetics," *Neuron*, vol. 86, no. 1, pp. 92–105, 2015.

[128] A. Schuz and G. Palm, "Density of Neurons and Synapses," *Journal of Comparative Neurology*, vol. 455, pp. 442–455, 1989.

[129] K. J. Seo, P. Artoni, Y. Qiang, Y. Zhong, X. Han, Z. Shi, W. Yao, M. Fagiolini, and H. Fang, "Transparent, Flexible, Penetrating Microelectrode Arrays with Capabilities of Single-Unit Electrophysiology," *Advanced Biosystems*, 2019.

[130] J. Pas, A. L. Rutz, P. P. Quilichini, A. Slézia, A. Ghestem, A. Kaszas, M. J. Donahue, V. F. Curto, R. P. O'Connor, C. Bernard, A. Williamson, and G. G. Malliaras, "A bilayered PVA/PLGA-bioresorbable shuttle to improve the implantation of flexible neural probes," *Journal of Neural Engineering*, vol. 15, no. 6, 2018.

[131] S. A. Hara, B. J. Kim, J. T. Kuo, C. D. Lee, E. Meng, and V. Pikov, "Long-term stability of intracortical recordings using perforated and arrayed Parylene sheath electrodes," *Journal of Neural Engineering*, vol. 13, no. 6, pp. 1–17, 2016.

[132] A. Maccione, M. Gandolfo, M. Tedesco, T. Nieus, K. Imfeld, S. Martinoia, and L. Berdondini, "Experimental investigation on spontaneously active hippocampal cultures recorded by means of high-density MEAs: Analysis of the spatial resolution effects," *Frontiers in Neuroengineering*, vol. 3, 2010.

[133] N. A. Steinmetz, C. Koch, K. D. Harris, and M. Carandini, "Challenges and opportunities for large-scale electrophysiology with Neuropixels probes," *Current Opinion in Neurobiology*, vol. 50, pp. 92–100, 2018.

[134] K. A. Ludwig, N. B. Langhals, M. D. Joseph, S. M. Richardson-Burns, J. L. Hendricks, and D. R. Kipke, "Poly(3,4-ethylenedioxythiophene) (PEDOT) polymer coatings facilitate smaller neural recording electrodes," *Journal of Neural Engineering*, vol. 8, no. 1, 2011.

[135] E. Slavcheva, R. Vitushinsky, W. Mokwa, and U. Schnakenberg, "Sputtered Iridium Oxide Films as Charge Injection Material for Functional Electrostimulation," *Journal of The Electrochemical Society*, vol. 151, no. 7, pp. 226–237, 2004.

[136] W. Hasenkamp, S. Musa, A. Alexandru, W. Eberle, and C. Bartic, "Electrodeposition and characterization of iridium oxide as electrode material for neural recording and stimulation," *IFMBE Proceedings*, vol. 25, no. 9, pp. 472–475, 2009.

[137] Q. Zeng, K. Xia, B. Sun, Y. Yin, T. Wu, and M. S. Humayun, "Electrodeposited Iridium Oxide on Platinum Nanocones for Improving Neural Stimulation Microelectrodes," *Electrochimica Acta*, vol. 237, pp. 152–159, 2017.

[138] E. W. Keefer, B. R. Botterman, M. I. Romero, A. F. Rossi, and G. W. Gross, "Carbon nanotube coating improves neuronal recordings," *Nature Nanotechnology*, vol. 3, no. 7, pp. 434–439, 2008.

[139] N. Burblies, J. Schulze, H. C. Schwarz, K. Kranz, D. Motz, C. Vogt, T. Lenarz, A. Warnecke, and P. Behrens, "Coatings of different carbon nanotubes on platinum electrodes for neuronal devices: Preparation, cytocompatibility and interaction with spiral ganglion cells," *PLoS ONE*, vol. 11, no. 7, pp. 1–22, 2016.

[140] H. Yamato, M. Ohwa, and W. Wernet, "Stability of polypyrrole and poly(3,4-ethylenedioxythiophene) for biosensor application," *Journal of Electroanalytical Chemistry*, vol. 397, no. 1-2, pp. 163–170, 1995.

[141] S. Baek, R. A. Green, and L. A. Poole-Warren, "The biological and electrical trade-offs related to the thickness of conducting polymers for neural applications," *Acta Biomaterialia*, vol. 10, pp. 3048–3058, 2014.

[142] A. S. Pranti, A. Schander, A. Bödecker, and W. Lang, "Highly Stable PEDOT:PSS Coating on Gold Microelectrodes with Improved Charge Injection Capacity for Chronic Neural Stimulation," *Proceedings*, vol. 1, no. 492, 2017.

References

[143] X. Cui and D. C. Martin, "Electrochemical deposition-and characterization of poly(3,4-ethylenedioxythiophene) on neural microelectrode arrays," *Sensors and Actuators B: Chemical*, vol. 89, pp. 92–102, 2003.

[144] P. M. George, A. W. Lyckman, D. A. Lavan, A. Hegde, Y. Leung, R. Avasare, C. Testa, P. M. Alexander, R. Langer, and M. Sur, "Fabrication and biocompatibility of polypyrrole implants suitable for neural prosthetics," *Biomaterials*, vol. 26, no. 17, pp. 3511–3519, 2005.

[145] A. J. Heeger, A. G. MacDiarmid, and H. Shirakawa, "Advanced Information - The Nobel Prize in Chemistry 2000," *Kungl. Vetenskapsakademien*, pp. 1–16, 1974.

[146] J. Rivnay, R. M. Owens, and G. G. Malliaras, "The rise of organic bioelectronics," *Chemistry of Materials*, vol. 26, no. 1, pp. 679–685, 2014.

[147] D. C. Martin and G. G. Malliaras, "Interfacing Electronic and Ionic Charge Transport in Bioelectronics," *ChemElectroChem*, vol. 3, no. 5, pp. 686–688, 2016.

[148] C. M. Proctor, J. Rivnay, and G. G. Malliaras, "Understanding volumetric capacitance in conducting polymers," *Journal of Polymer Science, Part B: Polymer Physics*, vol. 54, no. 15, pp. 1433–1436, 2016.

[149] T. L. Rose and L. S. Robblee, "Electrical stimulation with Pt electrodes. VIII. Electrochemically safe charge injection limits with 0.2 ms pulses.," *IEEE Transactions on Biomedical Engineering*, vol. 37, no. 11, pp. 1118–1120, 1990.

[150] A. Norlin, J. Pan, and C. Leygraf, "Investigation of interfacial capacitance of Pt, Ti and TiN coated electrodes by electrochemical impedance spectroscopy," *Biomolecular Engineering*, vol. 19, no. 2-6, pp. 67–71, 2002.

[151] J. Yang and D. C. Martin, "Impedance spectroscopy and nanoindentation of conducting poly(3,4-ethylenedioxythiophene) coatings on microfabricated neural prosthetic devices," *Journal of Materials Research*, vol. 21, no. 5, pp. 1124–1132, 2006.

[152] S. Baek, R. A. Green, and L. A. Poole-Warren, "Effects of dopants on the biomechanical properties of conducting polymer films on platinum electrodes," *Journal of Biomedical Materials Research - Part A*, vol. 102, no. 8, pp. 2743–2754, 2014.

[153] J. M. Fonner, L. Forciniti, H. Nguyen, J. D. Byrne, Y. F. Kou, J. Syeda-Nawaz, and C. E. Schmidt, "Biocompatibility implications of polypyrrole synthesis techniques," *Biomedical Materials*, vol. 3, no. 3, 2008.

[154] J. Rivnay, S. Inal, B. A. Collins, M. Sessolo, E. Stavrinidou, X. Strakosas, C. Tassone, D. M. Delongchamp, and G. G. Malliaras, "Structural control

of mixed ionic and electronic transport in conducting polymers," *Nature Communications*, vol. 7, pp. 1–9, 2016.

[155] E. M. Thaning, M. L. Asplund, T. A. Nyberg, O. W. Inganäs, and H. Von Holst, "Stability of poly(3,4-ethylene dioxythiophene) materials intended for implants," *Journal of Biomedical Materials Research - Part B Applied Biomaterials*, vol. 93, no. 2, pp. 407–415, 2010.

[156] A. Elschner, S. Kirchmeyer, W. Lovenich, and U. Merker, *PEDOT - Principles and Applications of an Intrinsically Conductive Polymer*. CRC Press, 2010.

[157] M. Lefebvre, Z. Qi, D. Rana, and P. G. Pickup, "Chemical synthesis, characterization, and electrochemical studies of poly(3,4-ethylenedioxythiophene)/ Poly(styrene-4-sulfonate) composites," *Chemistry of Materials*, vol. 11, no. 2, pp. 262–268, 1999.

[158] B. Winther-Jensen and K. West, "Vapor-phase polymerization of 3,4-ethylenedioxythiophene: A route to highly conducting polymer surface layers," *Macromolecules*, vol. 37, no. 12, pp. 4538–4543, 2004.

[159] H. Shi, C. Liu, Q. Jiang, and J. Xu, "Effective Approaches to Improve the Electrical Conductivity of PEDOT:PSS: A Review," *Advanced Electronic Materials*, vol. 1, no. 4, pp. 1–16, 2015.

[160] M. Sessolo, D. Khodagholy, J. Rivnay, F. Maddalena, M. Gleyzes, E. Steidl, B. Buisson, and G. G. Malliaras, "Easy-to-fabricate conducting polymer microelectrode arrays," *Advanced Materials*, vol. 25, no. 15, pp. 2135–2139, 2013.

[161] Y. Liang, M. Ernst, F. Brings, D. Kireev, V. Maybeck, A. Offenhäusser, and D. Mayer, "High Performance Flexible Organic Electrochemical Transistors for Monitoring Cardiac Action Potential," *Advanced Healthcare Materials*, vol. 7, no. 19, pp. 1–9, 2018.

[162] A. Phongphut, C. Sriprachuabwong, A. Wisitsoraat, A. Tuantranont, S. Prichanont, and P. Sritongkham, "A disposable amperometric biosensor based on inkjet-printed Au/PEDOT-PSS nanocomposite for triglyceride determination," *Sensors and Actuators, B: Chemical*, vol. 178, pp. 501–507, 2013.

[163] A. Benoudjit, M. M. Bader, and W. W. A. Wan Salim, "Study of electropolymerized PEDOT:PSS transducers for application as electrochemical sensors in aqueous media," *Sensing and Bio-Sensing Research*, vol. 17, no. August 2017, pp. 18–24, 2018.

[164] U. Lang, E. Muller, N. Naujoks, and J. Dual, "Microscopical investigations of PEDOT:PSS thin films," *Advanced Functional Materials*, vol. 19, no. 8, pp. 1215–1220, 2009.

References

[165] E. Stavrinidou, P. Leleux, H. Rajaona, D. Khodagholy, J. Rivnay, M. Lindau, S. Sanaur, and G. G. Malliaras, "Direct measurement of ion mobility in a conducting polymer," *Advanced Materials*, vol. 25, no. 32, pp. 4488–4493, 2013.

[166] S. Zhang, P. Kumar, A. S. Nouas, L. Fontaine, H. Tang, and F. Cicoira, "Solvent-induced changes in PEDOT:PSS films for organic electrochemical transistors," *APL Materials*, vol. 3, no. 1, pp. 1–8, 2015.

[167] O. P. Dimitriev, D. a. Grinko, Y. V. Noskov, N. a. Ogurtsov, and a. a. Pud, "PEDOT:PSS films-Effect of organic solvent additives and annealing on the film conductivity," *Synthetic Metals*, vol. 159, no. 21-22, pp. 2237–2239, 2009.

[168] V. Castagnola, C. Bayon, E. Descamps, and C. Bergaud, "Morphology and conductivity of PEDOT layers produced by different electrochemical routes," *Synthetic Metals*, vol. 189, pp. 7–16, 2014.

[169] E. Tamburri, S. Orlanducci, F. Toschi, M. L. Terranova, and D. Passeri, "Growth mechanisms, morphology, and electroactivity of PEDOT layers produced by electrochemical routes in aqueous medium," *Synthetic Metals*, vol. 159, no. 5-6, pp. 406–414, 2009.

[170] S. Patra, K. Barai, and N. Munichandraiah, "Scanning electron microscopy studies of PEDOT prepared by various electrochemical routes," *Synthetic Metals*, vol. 158, no. 10, pp. 430–435, 2008.

[171] ASTM International, "F1980 – 07: Standard Guide for Accelerated Aging of Sterile Barrier Systems for Medical Devices," 2016.

[172] H. Zhou, "Poly(3,4-ethylenedioxythiophene)/multiwall carbon nanotube composite coatings for improving the stability of microelectrodes in neural prostheses applications," *Acta Biomaterialia*, vol. 9, pp. 6439–6449, 2013.

[173] D. A. Koutsouras, P. Gkoupidenis, C. Stolz, V. Subramanian, G. G. Malliaras, and D. C. Martin, "Impedance Spectroscopy of Spin-Cast and Electrochemically Deposited PEDOT:PSS Films on Microfabricated Electrodes with Various Areas," *ChemElectroChem*, vol. 4, pp. 2321–2327, sep 2017.

[174] K. W. Horch and G. S. Dhillon, *Neuroprosthetics: Theory and Practice.* World Scientific Publishing Co. Pte. Ltd., 2nd ed., 2004.

[175] S. F. Cogan, "Neural Stimulation and Recording Electrodes," *Annual Review of Biomedical Engineering*, vol. 10, no. 1, pp. 275–309, 2008.

[176] C. Boehler, F. Oberueber, T. Stieglitz, and M. Asplund, "Iridium Oxide (IrOx) serves as adhesion promoter for conducting polymers on neural microelectrodes," *7th Annual International IEEE EMBS Conference on*

Neural Engineering, pp. 410–413, 2015.

[177] D. Pletcher and S. Sotiropoulos, "A study of cathodic oxygen reduction at platinum using microelectrodes," *Journal of Electroanalytical Chemistry*, vol. 356, no. 1-2, pp. 109–119, 1993.

[178] E. M. Hudak, J. T. Mortimer, and H. B. Martin, "Platinum for neural stimulation: Voltammetry considerations," *Journal of Neural Engineering*, vol. 7, no. 2, 2010.

[179] S. F. Cogan, J. Ehrlich, T. D. Plante, M. D. Gingerich, and D. B. Shire, "Contribution of oxygen reduction to charge injection on platinum and sputtered iridium oxide neural stimulation electrodes," *IEEE Transactions on Biomedical Engineering*, vol. 57, no. 9, pp. 2313–2321, 2010.

[180] J. Heinze, "Ultramicroelectrodes in Electrochemistry," *Angewandte Chemie International Edition in English*, vol. 32, no. 9, pp. 1268–1288, 1993.

[181] C. Boehler and M. Asplund, "PEDOT as a high charge injection material for low-frequency stimulation," *Proceedings of the Annual International Conference of the IEEE Engineering in Medicine and Biology Society*, pp. 2202–2205, 2018.

[182] D. Wakizaka, T. Fushimi, H. Ohkita, and S. Ito, "Hole transport in conducting ultrathin films of PEDOT/PSS prepared by layer-by-layer deposition technique," *Polymer*, vol. 45, no. 25, pp. 8561–8565, 2004.

[183] G. Dijk, H. J. Ruigrok, and R. P. O. Connor, "Influence of PEDOT : PSS Coating Thickness on the Performance of Stimulation Electrodes," *Advanced Materials Interfaces*, vol. 2000675, pp. 1–9, 2020.

[184] International Organization for Standardization, "ISO 10993-13: Identification and quantification of degradation products from polymeric medical devices," 2010.

[185] R. Caldwell, M. G. Street, R. Sharma, P. Takmakov, B. Baker, and L. Rieth, "Characterization of Parylene-C degradation mechanisms: In vitro reactive accelerated aging model compared to multiyear in vivo implantation," *Biomaterials*, vol. 232, 2020.

[186] M. ElMahmoudy, S. Inal, A. Charrier, I. Uguz, G. G. Malliaras, and S. Sanaur, "Tailoring the Electrochemical and Mechanical Properties of PEDOT:PSS Films for Bioelectronics," *Macromolecular Materials and Engineering*, vol. 302, no. 5, pp. 1–8, 2017.

[187] L. V. Lingstedt, M. Ghittorelli, H. Lu, D. A. Koutsouras, T. Marszalek, F. Torricelli, N. I. Crăciun, P. Gkoupidenis, and P. W. Blom, "Effect of DMSO Solvent Treatments on the Performance of PEDOT:PSS Based Organic

Electrochemical Transistors," *Advanced Electronic Materials*, vol. 5, no. 3, pp. 1–8, 2019.

[188] G. Dijk, A. L. Rutz, and G. G. Malliaras, "Stability of PEDOT:PSS-Coated Gold Electrodes in Cell Culture Conditions," *Advanced Materials Technologies*, vol. 5, no. 3, 2020.

[189] C. Boehler, F. Oberueber, S. Schlabach, T. Stieglitz, and M. Asplund, "Long-Term Stable Adhesion for Conducting Polymers in Biomedical Applications: IrOx and Nanostructured Platinum Solve the Chronic Challenge," *ACS applied materials & interfaces*, vol. 9, no. 1, pp. 189–197, 2017.

[190] H. S. Mandal, G. L. Knaack, H. Charkhkar, D. G. McHail, J. S. Kastee, T. C. Dumas, N. Peixoto, J. F. Rubinson, and J. J. Pancrazio, "Improving the performance of poly(3,4-ethylenedioxythiophene) for brain-machine interface applications," *Acta Biomaterialia*, vol. 10, no. 6, pp. 2446–2454, 2014.

[191] X. Du and Z. Wang, "Effects of polymerization potential on the properties of electrosynthesized PEDOT films," *Electrochimica Acta*, vol. 48, no. 12, pp. 1713–1717, 2003.

[192] M. Ujvári, J. Gubicza, V. Kondratiev, K. J. Szekeres, and G. G. Láng, "Morphological changes in electrochemically deposited poly(3,4-ethylenedioxythiophene) films during overoxidation," *Journal of Solid State Electrochemistry*, vol. 19, no. 4, pp. 1247–1252, 2015.

[193] M. A. Kamensky, S. N. Eliseeva, G. Láng, M. Ujvári, and V. V. Kondratiev, "Electrochemical Properties of Overoxidized Poly-3,4-Ethylenedioxythiophene," *Russian Journal of Electrochemistry*, vol. 54, no. 11, pp. 893–901, 2018.

[194] X. Cui and D. Zhou, "Poly (3,4-Ethylenedioxythiophene) for Chronic Neural Stimulation," *IEEE Transactions on Neural Systems and Rehabilitation Engineering*, vol. 15, no. 4, pp. 502–508, 2007.

[195] R. A. Green, R. T. Hassarati, L. Bouchinet, C. S. Lee, G. L. Cheong, J. F. Yu, C. W. Dodds, G. J. Suaning, L. A. Poole-Warren, and N. H. Lovell, "Substrate dependent stability of conducting polymer coatings on medical electrodes," *Biomaterials*, vol. 33, no. 25, pp. 5875–5886, 2012.

[196] A. S. Pranti, A. Schander, A. Bödecker, and W. Lang, "PEDOT: PSS coating on gold microelectrodes with excellent stability and high charge injection capacity for chronic neural interfaces," *Sensors and Actuators, B: Chemical*, vol. 275, no. March, pp. 382–393, 2018.

[197] S. F. Cogan, T. D. Plante, and J. Ehrlich, "Sputtered indium oxide films (SIROFs) for low-impedance neural stimulation and recording electrodes," *Annual International Conference of the IEEE Engineering in Medicine and Biology - Proceedings*, pp. 4153–4156, 2004.

[198] B. Wessling, A. Besmehn, W. Mokwa, and U. Schnakenberg, "Reactively Sputtered Iridium Oxide: Influence of Plasma Excitation and Substrate Temperature on Morphology, Composition, and Electrochemical Characteristics," *Journal of The Electrochemical Society*, vol. 154, no. 5, pp. 83–89, 2007.

[199] X. Y. Kang, J. Q. Liu, H. C. Tian, B. Yang, Y. Nuli, and C. S. Yang, "Fabrication and electrochemical comparison of SIROF-AIROF-EIROF microelectrodes for neural interfaces," *36th Annual International Conference of the IEEE Engineering in Medicine and Biology Society*, vol. 1, pp. 478–481, 2014.

[200] S. F. Cogan, J. Ehrlich, T. D. Plante, A. Smirnov, D. B. Shire, M. Gingerich, and J. F. Rizzo, "Sputtered iridium oxide films for neural stimulation electrodes," *Journal of Biomedical Materials Research - Part B Applied Biomaterials*, vol. 89, no. 2, pp. 353–361, 2009.

[201] J. Moral-Vico, S. Sánchez-Redondo, M. P. Lichtenstein, C. Suñol, and N. Casañ-Pastor, "Nanocomposites of iridium oxide and conducting polymers as electroactive phases in biological media," *Acta Biomaterialia*, vol. 10, no. 5, pp. 2177–2186, 2014.

[202] T. D. Kozai and D. R. Kipke, "Insertion shuttle with carboxyl terminated self-assembled monolayer coatings for implanting flexible polymer neural probes in the brain," *Journal of Neuroscience Methods*, 2009.

[203] A. Richter, Y. Xie, A. Schumacher, S. Löffler, R. D. Kirch, J. Al-Hasani, D. H. Rapoport, C. Kruse, A. Moser, V. Tronnier, S. Danner, and U. G. Hofmann, "A simple implantation method for flexible, multisite microelectrodes into rat brains," *Frontiers in Neuroengineering*, vol. 6, pp. 1–6, 2013.

[204] J. P. Harris, J. R. Capadona, R. H. Miller, B. C. Healy, K. Shanmuganathan, S. J. Rowan, C. Weder, and D. J. Tyler, "Mechanically adaptive intracortical implants improve the proximity of neuronal cell bodies," *Journal of Neural Engineering*, vol. 8, 2011.

[205] A. E. Hess, J. R. Capadona, K. Shanmuganathan, L. Hsu, S. J. Rowan, C. Weder, D. J. Tyler, and C. A. Zorman, "Development of a stimuli-responsive polymer nanocomposite toward biologically optimized, MEMS-based neural probes," *Journal of Micromechanics and Microengineering*, 2011.

[206] K. A. Potter, M. Jorfi, K. T. Householder, E. J. Foster, C. Weder, and J. R. Capadona, "Curcumin-releasing mechanically adaptive intracortical implants improve the proximal neuronal density and blood-brain barrier stability," *Acta Biomaterialia*, vol. 10, no. 5, pp. 2209–2222, 2014.

References

[207] A. Lecomte, V. Castagnola, E. Descamps, L. Dahan, M. C. Blatché, T. M. Dinis, E. Leclerc, C. Egles, and C. Bergaud, "Silk and PEG as means to stiffen a parylene probe for insertion in the brain: Toward a double time-scale tool for local drug delivery," *Journal of Micromechanics and Microengineering*, vol. 25, no. 12, 2015.

[208] D. Kil, M. Bovet Carmona, F. Ceyssens, M. Deprez, L. Brancato, B. Nuttin, D. Balschun, and R. Puers, "Dextran as a Resorbable Coating Material for Flexible Neural Probes," *Micromachines*, vol. 10, no. 1, p. 61, 2019.

[209] W. Jensen, U. G. Hofmann, and K. Yoshida, "Assessment of subdural insertion force of single-tine microelectrodes in rat cerebral cortex," in *Proceedings of the 25th Annual International Conference of the IEEE Engineering in Medicine and Biology Society*, 2003.

[210] N. H. Hosseini, R. Hoffmann, S. Kisban, T. Stieglitz, O. Paul, and P. Ruther, "Comparative study on the insertion behavior of cerebral microprobes," in *Annual International Conference of the IEEE Engineering in Medicine and Biology - Proceedings*, pp. 4711–4714, 2007.

[211] A. A. Sharp, A. M. Ortega, D. Restrepo, D. Curran-Everett, and K. Gall, "In Vivo Penetration Mechanics and Mechanical Properties of Mouse Brain Tiusse at Micrometer Scale," *IEEE Transactions on Biomedical Engineering*, vol. 56, no. 1, pp. 45–53, 2009.

[212] C.-H. Chen, S.-C. Chuang, H.-C. Su, W.-L. Hsu, T.-R. Yew, Y.-C. Chang, S.-R. Yeh, and D.-J. Yao, "A three-dimensional flexible microprobe array for neural recording assembled through electrostatic actuation.," *Lab on a Chip*, vol. 11, no. 9, pp. 1647–1655, 2011.

[213] S. Ramcharitar and P. W. Serruys, "Biodegradable stents," *Minerva Cardioangiologica*, vol. 56, no. 2, pp. 205–213, 2008.

[214] B. D. Ulery, L. S. Nair, and C. T. Laurencin, "Biomedical Applications of Biodegradable Polymers," *Journal of Polymer Science, Part B: Polymer Physics*, vol. 49, no. 12, pp. 832–864, 2011.

[215] F. Barz, P. Ruther, S. Takeuchi, and O. Paul, "Flexible silicon-polymer neural probe rigidified by dissolvable insertion vehicle for high-resolution neural recording with improved duration," in *Proceedings of the IEEE International Conference on Micro Electro Mechanical Systems*, pp. 636–639, 2015.

[216] I. Kaetsu, M. Yoshida, and A. Yamada, "Controlled slow release of chemotherapeutic drugs for cancer from matrices prepared by radiation polymerization at low temperatures," *Journal of Biomedical Materials Research*, vol. 14, no. 3, pp. 185–197, 1980.

[217] S. Parveen and S. K. Sahoo, "Long circulating chitosan/PEG blended PLGA nanoparticle for tumor drug delivery," *European Journal of Pharmacology*, vol. 670, no. 2-3, pp. 372–383, 2011.

[218] M. E. Mingot-Castellano, D. Diaz-Canales, F. Fernandez-Fuertes, M. Perera-Alvarez, I. Caparros-Miranda, R. Jimenez-Barcenas, A. Palomo-Bravo, A. I. Heiniger Mazo, and G. ACC, "Thrombopoietin Analogs In ITP Patients Daily Practice: Treatment Profile, Efficacy and Safety," *Blood*, vol. 122, no. 21, pp. 4749–4749, 2013.

[219] J. Manson, D. Kumar, B. J. Meenan, and D. Dixon, "Polyethylene glycol functionalized gold nanoparticles: The influence of capping density on stability in various media," *Gold Bulletin*, vol. 44, no. 2, pp. 99–105, 2011.

[220] Sigma Aldrich, "Polyethylene Glycol (PEG) - Selection Guide."

[221] O. I. Corrigan, C. A. Murphy, and R. P. Timoney, "Dissolution properties of polyethylene glycols and polyethylene glycol-drug systems," *International Journal of Pharmaceutics*, vol. 4, no. 1, pp. 67–74, 1979.

[222] O. Biondi, "Low molecular weight polyethylene glycol induces chromosome aberrations in Chinese hamster cells cultured in vitro," *Mutagenesis*, vol. 17, no. 3, pp. 261–264, 2002.

[223] S. Takeuchi, D. Ziegler, Y. Yoshida, K. Mabuchi, and T. Suzuki, "Parylene flexible neural probes integrated with microfluidic channels," *Lab on a Chip*, vol. 5, no. 5, pp. 519–523, 2005.

[224] M. Jorfi, J. L. Skousen, C. Weder, and J. R. Capadona, "Progress towards biocompatible intracortical microelectrodes for neural interfacing applications," *Journal of Neural Engineering*, vol. 12, no. 1, 2015.

[225] A. Sridharan, J. K. Nguyen, J. R. Capadona, and J. Muthuswamy, "Compliant intracortical implants reduce strains and strain rates in brain tissue in vivo," *Journal of Neural Engineering*, vol. 12, no. 3, p. 36002, 2015.

[226] S. R. Oh, "Thick single-layer positive photoresist mold and poly(dimethylsiloxane) (PDMS) dry etching for the fabrication of a glass–PDMS–glass microfluidic device," *Journal of Micromechanics and Microengineering*, vol. 18, no. 11, pp. 1–13, 2008.

[227] C. Chen, R. Plass, E. Ng, S. Lee, S. Meyer, G. Pawlowski, and R. Beica, "Development of thick negative photoresists for electroplating applications," *Advances in Resist Materials and Processing Technology XXV*, vol. 6923, 2008.

[228] M. Staab, F. Greiner, M. Schlosser, and H. F. Schlaak, "Applications of Novel High-Aspect-Ratio Ultrathick UV Photoresist for Microelectroplating,"

References

Journal of Microelectromechanical Systems, vol. 20, no. 4, pp. 794–796, 2011.

[229] D. Szmigiel, K. Domański, P. Prokaryn, and P. Grabiec, "Deep etching of biocompatible silicone rubber," *Microelectronic Engineering*, vol. 83, pp. 1178–1181, 2006.

[230] J.-K. Chen, F.-H. Ko, K.-F. Hsieh, C.-T. Chou, and F.-C. Chang, "Effect of fluoroalkyl substituents on the reactions of alkylchlorosilanes with mold surfaces for nanoimprint lithography," *Journal of Vacuum Science & Technology, B: Microelectronics and Nanometer Structures*, vol. 22, no. 6, p. 3233, 2004.

[231] S. A. Hara, B. J. Kim, J. T. Kuo, and E. Meng, "An Electrochemical Investigation of the Impact of Microfabrication Techniques on Polymer-Based Microelectrode Neural Interfaces," *Journal of Microelectromechanical Systems*, vol. 24, no. 4, pp. 801–809, 2015.

[232] A. Maccione, M. Garofalo, T. Nieus, M. Tedesco, L. Berdondini, and S. Martinoia, "Multiscale functional connectivity estimation on low-density neuronal cultures recorded by high-density CMOS Micro Electrode Arrays," *Journal of Neuroscience Methods*, vol. 207, no. 2, pp. 161–171, 2012.

[233] A. Agmon and B. W. Connors, "Thalamocortical responses of mouse somatosensory (barrel) cortex in vitro," *Neuroscience*, vol. 41, no. 2-3, pp. 365–379, 1991.

[234] J. N. MacLean, V. Fenstermaker, B. O. Watson, and R. Yuste, "A visual thalamocortical slice," *Nature Methods*, vol. 3, no. 2, pp. 129–134, 2006.

[235] U. Egert, D. Heck, and A. Aertsen, "Two-dimensional monitoring of spiking networks in acute brain slices," *Experimental Brain Research*, vol. 142, no. 2, pp. 268–274, 2002.

[236] T. A. Simeone, K. A. Simeone, K. K. Samson, D. Y. Kim, and J. M. Rho, "Loss of the Kv1.1 potassium channel promotes pathologic sharp waves and high frequency oscillations in in vitro hippocampal slices," *Neurobiology of Disease*, vol. 54, pp. 68–81, 2013.

[237] M. T. Schurr, A., Teyler, T. J., and Tseng, *Brain Slices: Fundamentals, Applications and Implications*. Kager, 1987.

[238] C. Yamamoto and H. McIlwain, "Electrical Activities in Thin Sections From the Mammalian Brain Maintained in Chemically-Defined Media in Vitro," *Journal of Neurochemistry*, vol. 13, no. 12, pp. 1333–1343, 1966.

[239] International Organization for Standardization, "ISO 10993-1: Biological evaluation of medical devices - Part 1: Evaluation and testing within a risk management process," 2020.

[240] D. B. Salkoff, E. Zagha, Ö. Yüzgeç, and D. A. McCormick, "Synaptic mechanisms of tight spike synchrony at gamma frequency in cerebral cortex," *Journal of Neuroscience*, vol. 35, no. 28, pp. 10236–10251, 2015.

[241] F. Grenier, I. Timofeev, and M. Steriade, "Neocortical very fast oscillations (ripples, 80-200 Hz) during seizures: Intracellular correlates," *Journal of Neurophysiology*, vol. 89, no. 2, pp. 841–852, 2003.

[242] J. M. Ibarz, G. Foffani, E. Cid, M. Inostroza, and L. M. De La Prida, "Emergent dynamics of fast ripples in the epileptic hippocampus," *Journal of Neuroscience*, vol. 30, no. 48, pp. 16249–16261, 2010.

[243] F. Grenier, I. Timofeev, and M. Steriade, "Focal synchronization of ripples (80-200 Hz) in neocortex and their neuronal correlates," *Journal of Neurophysiology*, vol. 86, no. 4, pp. 1884–1898, 2001.

[244] N. Maier, V. Nimmrich, and A. Draguhn, "Cellular and network mechanisms underlying spontaneous sharp wave-ripple complexes in mouse hippocampal slices," *Journal of Physiology*, vol. 550, no. 3, pp. 873–887, 2003.

[245] K. J. Suter, B. N. Smith, and F. E. Dudek, "Electrophysiological Recording from Brain Slices," *Methods*, vol. 18, no. 2, pp. 86–90, 1999.

[246] M. T. Schurr, A., Teyler, T. J., and Tseng, *Brain Slices: Fundamentals, Applications and Implications.* Kager, 1987.

[247] K. Rambani, J. Vukasinovic, A. Glezer, and S. M. Potter, "Culturing thick brain slices: An interstitial 3D microperfusion system for enhanced viability," *Journal of Neuroscience Methods*, vol. 180, no. 2, pp. 243–254, 2009.

[248] H. C. Lee, F. Ejserholm, J. Gaire, S. Currlin, J. Schouenborg, L. Wallman, M. Bengtsson, K. Park, and K. J. Otto, "Histological evaluation of flexible neural implants; Flexibility limit for reducing the tissue response?," *Journal of Neural Engineering*, vol. 14, 2017.

[249] Z. Fekete, A. Németh, G. Márton, I. Ulbert, and A. Pongrácz, "Experimental study on the mechanical interaction between silicon neural microprobes and rat dura mater during insertion," *Journal of Materials Science: Materials in Medicine*, vol. 26, no. 2, pp. 1–9, 2015.

[250] G. Buzsáki, "Theta oscillations in the hippocampus," *Neuron*, vol. 33, no. 3, pp. 325–340, 2002.

[251] F. Pothof, L. Bonini, M. Lanzilotto, A. Livi, L. Fogassi, G. A. Orban, O. Paul, and P. Ruther, "Chronic neural probe for simultaneous recording of single-unit, multi-unit, and local field potential activity from multiple brain sites," *Journal of Neural Engineering*, 2016.

References

[252] D. A. Soscia, D. Lam, A. C. Tooker, H. a. Enright, M. Triplett, P. Karande, S. K. G. Peters, A. P. Sales, E. K. Wheeler, and N. O. Fischer, "A flexible 3-dimensional microelectrode array for in vitro brain models," *Lab on a Chip*, 2020.

[253] A. F. Renz, A. M. Reichmuth, F. Stauffer, G. Thompson-Steckel, and J. Vörös, "A guide towards long-term functional electrodes interfacing neuronal tissue," *Journal of Neural Engineering*, vol. 15, no. 6, p. 061001, 2018.

[254] S. Sawano, K. Naka, A. Werber, H. Zappe, and S. Konishi, "Sealing method of PDMS as elastic material for MEMS," in *Proceedings of the IEEE International Conference on Micro Electro Mechanical Systems*, pp. 419–422, IEEE, 2008.

[255] Y. Chen, W. Pei, R. Tang, S. Chen, and H. Chen, "Conformal coating of parylene for surface anti-adhesion in polydimethylsiloxane (PDMS) double casting technique," *Sensors and Actuators, A: Physical*, vol. 189, pp. 143–150, 2013.

[256] H. Randriamahazaka, V. Noe, and C. Chevrot, "Nucleation and growth of poly(3,4-ethylenedioxythiophene) in acetonitrile on platinum under potentiostatic conditions," *Journal of Electroanalytical Chemistry*, vol. 472, pp. 103–111, 1999.

[257] F. Li and W. J. Albery, "A novel mechanism of electrochemical deposition of conducting polymers: two-dimensional layer-by-layer nucleation and growth observed for poly(thiophene-3-acetid acid)," *Electrochimica Acta*, vol. 37, no. 3, pp. 393–401, 1992.

[258] L. Pigani, A. Heras, Á. Colina, R. Seeber, and J. López-Palacios, "Electropolymerisation of 3,4-ethylenedioxythiophene in aqueous solutions," *Electrochemistry Communications*, vol. 6, no. 11, pp. 1192–1198, 2004.

[259] B. Fan, A. V. Rodriguez, D. L. Vercosa, C. Kemere, and J. T. Robinson, "Sputtered porous Pt for wafer-scale manufacture of low-impedance flexible microelectrodes," *bioRxiv*, 2020.

[260] A. Mercanzini, K. Cheung, D. L. Buhl, M. Boers, A. Maillard, P. Colin, J. C. Bensadoun, A. Bertsch, and P. Renaud, "Demonstration of cortical recording using novel flexible polymer neural probes," *Sensors and Actuators, A: Physical*, vol. 143, no. 1, pp. 90–96, 2008.

[261] J. L. Hutter and J. Bechhoefer, "Calibration of atomic-force microscope tips," *Review of Scientific Instruments*, vol. 64, no. 7, pp. 1868–1873, 1993.

[262] H. Hertz, "Über die Berührung fester elastischer Körper," *Journal für die reine und angewandte Mathematik*, vol. 92, pp. 156–171, 1881.

[263] I. N. Sneddon, "The relation between load and penetration in the axisymmetric boussinesq problem for a punch of arbitrary profile," *International Journal of Engineering Science*, vol. 3, no. 1, pp. 47–57, 1965.

[264] M. Radmacher and M. Fritz, "Imaging Soft Samples," vol. 69, no. July, pp. 264–270, 1995.

[265] A. L. Weisenhorn, M. Khorsandi, S. Kasas, V. Gotzos, and H. J. Butt, "Deformation and height anomaly of soft surfaces studied with an AFM," *Nanotechnology*, vol. 4, no. 2, pp. 106–113, 1993.

Acknowledgements

I would like to thank all my family, friends, and colleagues, who supported me and my work during my PhD. Without your help and support, this work would not have been possible.

Prof. Dr. Andreas Offenhäusser, vielen Dank für die Betreuung in den letzten drei Jahren und außerdem für das Vertrauen und die Möglichkeit, an diesem interessanten Thema und in dem multidisziplinären Institut IBI-3 zu arbeiten.

Prof. Dr. Sven Ingebrandt, danke für das Wecken meines Interesses für MEMS Technologien bereits während meines Bachelorstudiums und für die Einwilligung meine Promotion als Zweitprüfer zu unterstützen.

Danke an alle Biologen, die es ermöglicht haben, meine entwickelten Implantate innerhalb von Tierversuchen zu testen: Kerstin Doerenkamp, Renata Medinaceli Quintela, Dr. Simon Musall, Dr. Markus Rothermel und Prof. Dr. Björn Kampa. Furthermore, thank you, Dr. Vanessa Maybeck and Bettina Breuer, for helping me establishing slice recordings, which gave me the possibility to validate the neural probes within the institute.

Viviana Rincón Montes, thank you for the collaborative work in probe fabrication and in conference contributions. Special thanks for all the scientific discussions we had.

Marko Banzet, Michael Prömpers und alle technischen Angestellten der HNF, danke für die angenehme Atmosphäre, die das Arbeiten im Reinraum mit viel Spaß verband. Außerdem vielen Dank für eure Unterstützung und Geduld vor allem bei ausgefallenen Ideen, wie z.B. Proben aus PDMS herzustellen.

Elke Brauweiler-Reuters, vielen Dank für deine Hilfe mit all den SEM Bilder und FIB Schnitten. Besonderen Dank dafür, dass du auch bei kurzfristigen Anfragen immer versucht hast, einen Weg zu finden, die Proben rechtzeitig zu charakterisieren.

Acknowledgements

Own Publications

Journal articles

K. Srikantharajah, R. Medinaceli Quintela, B. M. Kampa, S. Musall, M. Rothermel, and
A. Offenhäusser, **Minimally-invasive insertion strategy and in vivo evaluation
of multi-shank flexible intracortical probes**, *Scientific Reports*, vol. 11, 2021. doi:
10.1038/s41598-021-97940-x

D. Kireev, V. Rincón Montes, J. Stevanovic, K. Srikantharajah, and A. Offenhäusser, **N3-MEA
probes: Scooping neuronal networks**, *Frontiers in Neuroscience*, vol. 13, 2019. doi:
10.3389/fnins.2019.00320.

D. Kireev, P. Shokoohimehr, M. Ernst, V. Rincón Montes, K. Srikantharajah, V. Maybeck,
B. Wolfrum, and A. Offenhäusser, **Fabrication of ultrathin and flexible graphene-
based devices for in vivo neuroprosthetics**, *MRS Advances*, vol. 3, no. 29, 2018. doi:
10.1557/adv.2018.94

Conference posters

K. Srikantharajah, V. Rincón Montes, D. T. Vu, B. Lenyk, D. Kireev, and A. Offenhäusser.
Progress towards compliant penetrating implants for *in vivo* applications, 6th
International Winterschool on Bioelectronics (BioEl 2019), Kirchberg in Tyrol, Austria.

V. Rincón Montes, K. Srikantharajah, D. Kireev, J. Lange, and A. Offenhäusser (2019). **From
stiff to compliant retinal and cortical multisite penetrating implants**, MEA
Meeting 2018, Reutlingen, Germany. doi: 10.3389/conf.fncel.2018.38.00072.

K. Srikantharajah, V. Rincón Montes, D. Kireev, J. Lange, M. Ernst, and A. Offenhäusser.
**Development of highly flexible and penetrating microelectrode arrays for corti-
cal and retinal applications**, Neuroelectronic Interfaces - Gordon Research Conference
2018, Galveston, Texas, USA.

Other talks

Talk - K. Srikantharajah, **Mounting headstages for brain recordings on small animals.**,
Int. Workshop Neuroelectronics, Hirschegg, Austria, 2019

Talk - K. Srikantharajah, **Insertion Systems - How to implant flexible neuronal probes?**,
Int. Workshop Bioelectronics - New Challenges, Hirschegg, Austria, 2018.

Band / Volume 59
Defect engineering in oxide thin films
F. V. E. Hensling (2019), 10, 164 pp
ISBN: 978-3-95806-424-9

Band / Volume 60
Chemical control of the electrical surface properties of *n*-doped transition metal oxides
M. Andrä (2019), X, 150, XXXVIII pp
ISBN: 978-3-95806-448-5

Band / Volume 61
Digital Signal Processing and Mixed Signal Control of Receiver Circuitry for Large-Scale Particle Detectors
P. Muralidharan (2020), xv, 109 pp
ISBN: 978-3-95806-489-8

Band / Volume 62
Development of Electromagnetic Induction Measurement and Inversion Methods for Soil Electrical Conductivity Investigations
X. Tan (2020), ix, 124 pp
ISBN: 978-3-95806-490-4

Band / Volume 63
Novel System Approach for a mm-range Precision Indoor Positioning System
R. Xiong (2020), xi, 144 pp
ISBN: 978-3-95806-517-8

Band / Volume 64
Quantitative investigation of group III-nitride interfaces by a combination of scanning tunneling microscopy and off-axis electron holography
Y. Wang (2021), 102 pp
ISBN: 978-3-95806-534-5

Band / Volume 65
Scalable Control Electronics for a Spin Based Quantum Computer
L. Geck (2021), xiv, 114, xv-xxxiii
ISBN: 978-3-95806-540-6

Band / Volume 66
DNA-capped silver nanoparticles for stochastic nanoparticle impact electrochemistry
L. Nörbel (2021), VI, 142 pp
ISBN: 978-3-95806-541-3

Schriften des Forschungszentrums Jülich
Reihe Information

Weitere *Schriften des Verlags im Forschungszentrum Jülich* unter
http://wwwzb1.fz-juelich.de/verlagextern1/index.asp

JÜLICH
Forschungszentrum